ABSTRACT

Title of Document: SCAFFOLD DESIGN PARAMETERS TO STIMULATE THE OSTEOGENIC SIGNAL EXPRESSION FOR BONE TISSUE ENGINEERING APPLICATIONS

Kyobum Kim, Doctor of Philosophy, 2010

Directed By: Associate Professor John P. Fisher, Fischell Department of Bioengineering

The fundamental components of bone tissue engineering are (a) progenitor cells which subsequently express tissue matrix, (b) scaffolds which can act as temporary frameworks to support bone growth, and (c) growth factors to induce osteoblast regeneration. A variety of growth factors are involved during the differentiation cascade and these chemical and biological signals dynamically interact with cell populations to facilitate the differentiation. Therefore, enhanced expression of endogenous growth factor genes might facilitate abundant existence of growth factors in the surrounding microenvironment, stimulate the osteogenic differentiation of progenitor cell population, and finally induce bone regeneration. This work is focused on the augmentation of osteogenic signal expressions to stimulate the downstream differentiation of transplanted bone marrow stromal cells (BMSCs) population through the optimization of a variety of properties of three dimensional (3D) biodegradable poly(propylene fumarate) (PPF) scaffold. Changes in the

microenvironment of cell population would affect the responses of localized cell population and the manipulated scaffold properties might be associated with induction of endogenous osteogenic signal expressions.

First, the effect of cell-to-cell paracrine signaling distance, which can by modulated by initial cell seeding density, on the osteogenic signal expressions and osteoblastic differentiation of BMSCs on 2D PPF disks was investigated. Next, in order to investigate the improvement of the 3D macroporous PPF scaffold by the incorporation with nanoparticle filler materials, PPF/hydroxyapatite (HA) nanocomposite scaffolds were fabricated. The effect of HA content and initial cell seeding density on the osteogenic signal expression in 3D porous system was then determined. Finally, the incorporation of diethyl dumarate (DEF) with PPF was tested based on the photocrosslinking characteristics of PPF/DEF composite material with increased mechanical properties. The effect of two scaffold design parameters including the stiffness by modulating the DEF content as well as the pore size of porous scaffold on the signal expression and downstream osteoblastic differentiation was investigated. In addition, the feasibility of PPPF/DEF materials for stereolithographical fabrication was also tested in this work.

Controlling these construction parameters to optimize engineered bone substitutes could affect various cellular functions of attachment, proliferation, signal expression, and differentiation. This research provided the insight of stimulation of the expression of target endogenous genes to induce the osteogenic differentiation and bone regeneration as well as the fabrication of improved bone substitute implant materials which is clinically applicable.

SCAFFOLD DESIGN PARAMETERS TO STIMULATE THE OSTEOGENIC SIGNAL EXPRESSION FOR BONE TISSUE ENGINEERING APPLICATIONS

By

Kyobum Kim

Dissertation submitted to the Faculty of the Graduate School of the
University of Maryland, College Park, in partial fulfillment
of the requirements for the degree of
Doctor of Philosophy
2010

Advisory Committee:
Associate Professor John P. Fisher, Chair
Professor William E. Bentley
Professor Sheryl Ehrman
Associate Professor Srinivasa R. Raghavan
Assistant Professor Ganesh Sriram

Dedication

This work is dedicated to my love, Hyeyeon, and my precious kids, Iris and Sebastian.

Acknowledgements

I would like to thank my advisor Dr. John Fisher, whose encouragement, guidance and great support enabled me to develop an understanding of this study. It is a pleasure to show my gratitude to him for his effort to introduce me to the world of science, engineering, and research.

Table of Contents

List of Tables

List of Figures

Chapter 1: Introduction

A variety of growth factors, cytokines, and hormones are involved during the differentiation cascade and these chemical and biological signals dynamically interact with cell populations to facilitate the differentiation. Therefore, enhanced expression of endogenous growth factor genes might facilitate abundant existence of growth factors in the surrounding microenvironment, stimulate the osteogenic differentiation of progenitor cell population, and finally induce bone regeneration. This work is focused on the augmentation of expression of these osteogenic signals in order to stimulate the downstream differentiation by optimizing the properties of 3D poly(propylene fumarate) (PPF) scaffold and the microenvironment of cell population. It has been demonstrated that scaffold construction parameters including cell-to-cell paracrine signaling distance, the types and amounts of nano-sized mineral filler material for the fabrication of nanocomposite scaffolds, and physical scaffold construction factors such as porosity, pore size, scaffold interconnectivity, and mechanical strength (stiffness), influence the osteogenic growth factor gene expression. By using a biodegradable PPF polymer, cell/scaffold parameters were investigated for the optimal stimulation of desired signal expression and the induction of osteogenic differentiation of a recruited cell population for bone tissue regeneration. Controlling these construction parameters to optimize engineered bone substitutes could affect various cellular functions of attachment, proliferation, signal expression, and differentiation. Stereolithographical fabrication of controlled geometry of 3D macroporous scaffolds has also been investigated for the

development of patient specific implants. This research provided the insight of stimulation of the expression of target endogenous genes to induce the osteogenic differentiation and bone regeneration as well as the fabrication of improved bone substitute implants which is clinically applicable.

Chapter 2: Stereolithographic Bone Scaffold Design Parameters – Osteogenic Signal Expression and Differentiation

2.1. Introduction

Tissue engineering strategies involving cell/scaffold constructs represent a promising alternative for the treatment of bone injuries. However, the nature and extent of the interactions between cells and the scaffolds are not yet fully understood. Recent research in bone tissue engineering has utilized mesenchymal stem cells (MSCs) for the preparation of cell/scaffold complexes. (Please see Table 1 for a list of abbreviations.) Due to the capability of MSCs to differentiate into multiple tissues, it is of importance to optimize a variety of parameters including chemical, biological, and mechanical cues to induce the osteogenic differentiation of a scaffold-localized cell population. Progenitor MSCs either transplanted to scaffolds before implantation or recruited from surrounding host tissues, may differentiate into osteogenic lineages through a series of steps including proliferation, matrix formation, and mineralization [1]. During these stages, a variety of growth factors, cytokines, and hormones are involved and these chemical/biological signals dynamically interact with cell populations to facilitate differentiation cascades. Bone morphogenetic protein-2 (BMP-2),[2-5] fibroblast growth factor,[6, 7] transforming growth factor,[8, 9] vascular endothelial growth factor,[10-12] and platelet-derived growth factor[7, 13] are the major osteogenic growth factors while alkaline phosphatase (ALP) and

As published in **K. Kim,** A. Yeatte, D. Dean, and J.P. Fisher, "Stereolithographic Bone Scaffold Design Parameters: Osteogenic Signal Expression and Differentiation", Tissue Engineering Part B (In Press). .

osteocalcin (OC) are osteogenic differentiation marker proteins. In addition, osteopontin (OP), osteonectin, and bone sialoprotein (BSP) are the important protein components of bone extracellular matrix [14, 15]. Therefore, secreted growth factors from cells may be closely related to the regulation of osteogenic differentiation of a scaffold-localized cell population prior to implantation as well as a recruited cell population from the surrounding host tissues. Enhanced expression of endogenous growth factor genes might facilitate abundant existence of growth factors in the surrounding microenvironment, stimulate the osteogenic differentiation of progenitor cell population, and finally induce bone regeneration. In addition to the upregulation of osteogenic signal expression but also the control of dynamic signaling pathways such as Smad, mitogen activated protein kinase (MAPK) [5, 16], Wnt [17], and the involvement of runt-related transcription factor-2 (Runx2) [18, 19] and receptor activator of nuclear factor κB ligand (RANK-L) [20] might facilitate a tissue engineered cell/scaffold construct in bringing about bone tissue regeneration.

The association of many cell/scaffold construction parameters influences osteogenic signal expression. Among those parameters, physical construction factors, specifically scaffold design parameters including porosity, pore size, scaffold interconnectivity, and mechanical strength (stiffness) have been shown to influence the osteogenic signal expression and subsequent differentiation of cells seeded on scaffolds both *in vitro* and *in vivo* [21-24]. Furthermore, it has also been demonstrated that these properties might impact the architecture and the amount of *in vivo* bone formation [25-28]. Therefore, the demonstrated importance of these scaffold parameters dictates that an optimal bone tissue engineering scaffold must be

achieved for the stimulation of desired signal expression and the induction of osteogenic differentiation of the recruited cell population. Along with the combination of other chemical and biological factors such as the administration of growth factor proteins, the repeated construction of precisely controlled architectures with the optimal design parameters is necessary to achieve an optimal bone tissue engineering scaffold. Stereolithography (SLA) represents a promising advanced scaffold manufacturing technique to achieve this goal [29-31]. SLA is the rapid prototyping technique which uses photopolymerization to create 3D scaffolds layer by layer to a design specification that is input via computer [32-34]. This method will enable scaffolds to be reproduced with controlled porosity, pore size, interconnectivity and mechanical properties all of which greatly influence osteogenic signaling and differentiation. Therefore, this review will (1) discuss the influence of scaffold construct parameters on *in vitro* osteogenic signaling and *in vivo* bone formation and (2) evaluate SLA as a manufacturing technology to fabricate scaffolds to meet the requirements set forth in the literature.

2.2. Structural Parameters to Control Cell Signaling

2.2.1. Effect of porosity and pore size on cell signaling

The ability of a scaffold to enhance osteogenic signal expression and support new bone formation is largely dependent on the pore size and porosity of the scaffold (See Table 2). Porosity refers to the overall percentage of void space within a solid, while pore size reflects the diameter of individual voids in the scaffold [35]. The importance of scaffold porosity and pore size can be attributed to the native structure

of bone which itself is a porous tissue. Cortical bone is largely a dense structure, but within it exists pores that give an overall porosity of 10% [36]. Conversely, trabecular

3DP	three dimensional printing
ALP	alkaline phosphatase
BMP	bone morphogenic protein
BMSC	bone marrow stromal cell
BSP	bone sialoprotein
CAD	computer aided design
CARP	computer aided rapid prototyping
DEF	diethyl fumarate
DHT	dehydrothermal
ECM	extracellular matrix
ERK	extracellular signal-regulated kinase
FAK	focal adhesion kinase
FAME	fumaric acid monoethyl ester
GAG	glycosaminoglycan
HA	hydroxyapatite
MAPK	mitogen activated protein kinase
MSC	mesenchymal stem cell
NVP	N-Vinyl-2-pyrrolodone
OC	osteocalcin
OCM	olygocarbonate dimethacrylate
OP	osteopontin
PBT	poly(butylene terephthalate)
PCL	polycaprolactone
PDLLA	poly(D,L-lactide)
PDMS	Polydimethylsiloxane
PEG	poly(ethylene glycol)
PEG-DA	poly(ethylene glycol)-diacrylate
PEG-DMA	poly(ethylene glycol)-dimethacrylate
PEO	poly(ethylene oxide)
PLG	poly(L-lactic-co-glycolide)
PLGA	poly(lactic-co-glycolic acid)
PLA	poly(L-lactide)
PLLA	poly(L-lactic acid)
PMMA	Poly(methyl methacrylate
PPF	poly(propylene fumarate)
RANK-L	receptor activator of nuclear factor κB ligand
RhoA	Ras homolog gene family, member A
RGD	arginine-glycine-aspartic acid
ROCK	Rho-associated, coiled-coil containing protein kinase 1
Runx2	runt-related transcription factor-2
SEM	scanning electron microscope
SFF	solid freeform fabrication
SLA	stereolithography
TCP	tricalcium phosphate

Table 1: Abbreviations

bone is a highly porous structure with typical porosity values between 50 and 90% [36]. Porous regions of cortical bone allow for vascularization and cellular infiltration of the structure. Porosity and pore size have significant ramifications on the ability of tissue engineering scaffolds to support bone regeneration for several reasons. First, porosity and pore size have been shown to affect cell attachment efficiency which consequently impacts the cell seeding density, cell distribution and cell migration [37]. These factors have been shown to affect osteogenic differentiation through changes in signaling distances [38]. Moreover, pore size and porosity have a significant effect on the mechanical strength of a scaffold. Sufficient scaffold strength to provide mechanical support to a defect is often required of a hard tissue engineering scaffold such as bone, especially when the bone is load bearing [39]. Furthermore, porosity and pore size affect the ability of the scaffold to promote *in vivo* osteoconduction and vascularization. Integration of native tissue into a scaffold is fostered through growth into interconnected pores, thus both optimal and minimal pore sizes have been established to support tissue ingrowth [35, 40]. Finally, pore size and porosity affect *in vivo* and *in vitro* cell signaling which in turn affects osteoblastic differentiation of MSCs and the production of extracellular matrix (ECM) proteins [35, 41-45].

Not only must the optimal bone tissue engineering scaffold support the growth and osteogenesis of a seeded cell population, it must also support osteoconduction and vascularization from the surrounding tissue [46, 47]. Both osteoconduction and vascularization are influenced by scaffold pore size, porosity and interconnectivity of pores. In scaffolds with similar porosities (~50 %), it has been established that pore

sizes of at least 40 μm are required for minimal bone in growth while pore sizes of 100-350 μm are considered optimal [47, 48]. In a study analyzing the effect of pore size and porosity on bone healing in a critical size rat cranial defect, it was shown that smaller pore sizes (100 μm) induce greater amounts of bone healing than larger pore sizes (500 μm) [49]. This study also found a link to porosity, scaffold swelling, and degradation. It may be desirable to have the scaffold size and shape change over time as the scaffold material is resorbed, and to have the regenerated bone tissue remodel. In these remodeling cases, the material type and degradation rate should be factored into determining optimal pore volume, pore geometry, inter-pore wall thickness and porosity. Scaffolds with the larger pore sizes were found to have limited bone growth after about 4 weeks [49, 50]. Thus it was hypothesized that the smaller pore sizes may enhance continuous host tissue ingrowth. It was also concluded that pore size influences the location of tissue ingrowth, indicating that porosity and pore size should be tailored to different bone types and injury sites, a difficult task with traditional scaffold manufacturing methods.

In another study, femoral bone scaffolds with pore sizes of 565 μm exhibited higher amounts of bone formation than scaffolds with pore sizes of 300 μm. Within these pore size groups, porosity was also varied from 40% to 50%, but no significant change in bone growth was observed indicating that porosity may have less of an effect on bone growth than pore size [26]. Despite numerous studies on the topic, there is still disagreement over the significance of pore size on *in vivo* bone formation. In polycaprolactone (PCL) scaffolds made with pore sizes of 350, 550, and 800 μm, limited differences were observed in the amount of bone growth after 8

weeks [50]. After 4 weeks, the largest pore size group did exhibit greater bone growth, which could indicate that pore size does influence the amount of bone ingrowth, but after 8 weeks that influence could no longer be discernable. It might be possible that more dramatic responses to pore size are only seen at lower pore sizes. For example, it was found that pore sizes of 300 μm induced significantly increased amounts of bone growth after 4 weeks using PCL scaffolds in a rabbit cranial defect than 100, 200, or 400 μm pore sizes [27]. The discrepancy between these studies could indicate that pore size is not the only variable influencing bone growth. The material type and pore shape as well as the implant size and surrounding tissue vascularization could also influence the effects of pore size on bone ingrowth.

Despite these discrepancies, the influence of pore size and porosity on *in vivo* bone growth has been noted. Pore size has been observed to not only influences the osteoconduction of a scaffold, but also the vascularization, which is crucial to successful bone formation. In a study utilizing calcium phosphate ceramics, pore sizes of 140 - 280 μm exhibited faster vessel formation than those of 40 - 140 μm. Also larger pore sizes had significantly higher capillary density than small pore sizes. The volume of new bone correlated with these results as the largest pore size group (210-280 μm) had the most new bone growth [40]. Rapid vascularization is important for bone tissue growth in an implanted scaffold as cells on the interior portions of the scaffolds will not survive without a blood and nutrient supply. Oxygen and nutrient transfer distances are limited to approximately 200 μm making vascularization a concern even in smaller scaffolds [51]. The degree of vascularization in a bone tissue engineering scaffold also influences the mechanism

by which bone formation occurs [40, 52]. Hydroxyapatite (HA) scaffolds with pore sizes of 90-120 μm were shown to support bone formation by a process of endochondral ossification where MSCs proliferate on the scaffold and begin to form cartilage tissue [53]. The cartilage then begins to become vascularized and is resorbed by phagocytotic cells. MSCs migrate to the site, differentiate into osteoblasts and begin to form bone. This process can lead to the highly organized bone structures observed in long bones [36]. Scaffolds with pore sizes of 350 μm were observed to form bone through intramembranous ossification where MSCs initially migrate in with vascularization and form new bone directly without any cartilage formation [53]. This type of bone formation is typical in the cranium and other flat bones. Pore size can influence the method of bone formation as it affects the degree of vascularization, which in turn affects the oxygen present in the tissue and ultimately whether chondrogenesis or osteogenesis occurs. Therefore, the effect of pore size on the mechanism that results in bone formation underscores the importance of precise control over the pore size and porosity of the scaffold and pore architecture may need to be tailored to specific bones for effective tissue engineering.

In addition to *in vivo* bone growth, it has also been shown that *in vitro* cell growth and differentiation on scaffolds are greatly affected by pore size and porosity. While *in vivo* porosity and pore size mainly influence bone growth by influencing the native tissue that invades the scaffold, *in vitro* studies have emphasized the influence of pore size and porosity on the migration, proliferation, differentiation and signaling of cells within a scaffold [35]. For instance, Mygind *et al* have shown the effect of pore size on the expression of a series of osteogenic signals [23]. Human MSCs

cultured on coralline HA scaffolds exhibited lower proliferation rate and higher degree of differentiation as shown by increased ALP, OC, and BMP-2 mRNA expression on scaffolds with a smaller pore size (200 μm) as opposed to a larger pore size (500 μm). The enhancement of osteogenic differentiation and a lower proliferation rate may both be explained by the difference in surface area and transport efficiency resulting from the change in pore size. It might be suggested that a scaffold geometry with smaller pore size resulted in increasing tortuosity, thereby decreasing transport efficiency of soluble factors in the aqueous surrounding environments, and limiting the cell infiltration. Subsequently, decreased proliferation might be observed because of changes in signaling distances through varying the pore geometry that induces a higher level of differentiation. Another study has also shown that pore size and porosity influence expression levels of osteogenic signals. In collagen-glycosaminoglycan (GAG) scaffolds greater expression of OC and type one collagen in MSCs after 21 days of culture was observed in scaffolds with pore sizes of 151 μm as compared to 96 μm [41]. Moreover, pore size has also been shown to influence the differentiation of human MSCs on β-tricalcium phosphate (ß-TCP) scaffolds with varying porosities (25 to 75%) and pore sizes (10 to 600 μm, respectively) [21]. In this research, no significant difference was observed in the *in vitro* osteogenic differentiation between the groups. However, when the samples were implanted into skin folds of mice, a significantly higher amount of osteoblastic differentiation was observed as shown by ALP production in scaffold constructs with 65 and 75% porosities with the highest amount observed in the 65% group. This study indicates that porosity may not be the sole influence of osteogenic

differentiation and that differences in signal expression might be observed relating from pore size *in vivo* even without bone ingrowth from surrounding tissues [21]. Using an hydrogel fabricated from PEG-DA and 5-ethyl-5-(hydroxymethyl)-β,β-dimethyl-1,3-dioxane-2-ethanol diacrylate, the effect of pore size and porosity on the BMP-2 signaling of human MSCs was investigated in scaffolds with pore sizes of 100 and 250 μm [45]. In this study, BMP-2 signaling was upregulated in the scaffolds with 250 μm pore size as compared to those with 100 μm pore size with the same porosity on day of 4, 8 and 12. This indicates pore size has an effect on BMP-2 signal expression. Furthermore, 50-70 fold increases in BMP-2 expression were observed in 3D porous gels as compared to 2D monolayer culture, highlighting the effect of 3D architecture on signal expression. It was hypothesized that this effect resulted from a concentration of signaling molecules within the hydrogel enhancing autocrine and paracrine cell signaling.

Scaffold porosity and pore size can influence *in vitro* growth and differentiation of a seeded MSC population, although these effects are often less pronounced ways than *in vivo* bone growth. While much research has been done in this area, further studies are necessary to determine the optimal pore size for *in vitro* bone growth and to fully elucidate the effect of pore size and porosity on cell signaling. For the future of bone tissue engineering highly controlled and characterized scaffolds must be created to not only further evaluate the influence of porosity and pore size, but also to create scaffolds with reliable geometries to ensure predictable clinical use.

Scaffold Materials	*Function and Biological Improvements*	*Reference*
Collagen-GAG	Pore size affects OC, OP, collagen I and BSP mRNA expression.	[41]
	Improved migration in pore sizes larger than 300 μm.	[54]
Calcium Phosphate	Higher pore sizes (280 μm) result in greater osseointegration. Pore size also affects blood vessel formation.	[40]
	Bone growth affected more by pore size than porosity. Larger pore size induces greater bone formation.	[26]
ß-TCP	ALP expression affected by size of pores and porosity of scaffolds. Higher mineralization with higher porosity.	[21]
PLGA	Pore size and porosity affects spatial distribution of new bone formation in cranial defect.	[49]
PCL	Pore sizes between 350-800 μm have limited role on bone regeneration after 8 weeks of implantation subcutaneously in mice.	[50]
	Pore size affects bone formation and type of tissue formed.	[27]
EH-PEG	Pore size affects BMP-2 expression.	[45]
HA	Higher ALP expression of human MSCs in smaller pore sizes (200μm). Higher proliferation in larger pore sizes (500 μm).	[23]

Table 2: The Effect of Porosity and Pore Size on Osteogenic Signal Expression and Differentiation

2.2.2. Scaffold interconnectivity

Another important characteristic of scaffold architecture is the degree of interconnectivity between the pores of a scaffold. Scaffolds that feature a highly interconnected architecture allow for enhanced communication between cells at different areas within a scaffold and promote tissue ingrowth (See Table 3). Scaffold

interconnectivity has been shown to have a limited direct effect on MSC signaling and differentiation, but a profound effect on the morphology of bone formed within a scaffold [55-57]. When human MSCs were seeded on silk constructs, no significant differences were observed in ALP expression and calcium deposition after 4 weeks of culture between scaffolds with different levels of interconnectivity [55]. Significant differences were observed however in the degree of cellular ingrowth into the scaffolds. It was observed that growth into scaffolds with low interconnectivity was confined to surface pores, while highly interconnected scaffolds featured homogenous mineralization and a network of bonelike tissue. In another study using poly(L-lactide-co-glycolide) (PLG), levels of vinculin, β-actin, OC, and OP of human MG63 cells were similar for scaffolds with varying interconnectivities [58]. Greater penetration depth was observed in scaffolds with larger pore sizes and higher interconnectivity although these differences diminished after 15 days. This study suggested that increasing pore size and interconnectivity yielded faster colonization of cells and that degree of interconnectivity should be tailored to bone cells as connective tissues may infiltrate more quickly into smaller connections, resulting in inhibition of bone tissue infiltration. Scaffold interconnectivity may also affect bone formation and osteogenic signal expression by affecting the degree of nutrient diffusion into a scaffold [59]. As previously described bone nutrient and oxygen transfer are a concern in any 3D construct.

Degree of interconnectivity is not the sole factor influencing bone ingrowth as the diameter of channels connecting pores has also been shown to influence cell penetration. In a study to investigate the effect of channel diameter on cell

penetration *in vitro* using HA scaffolds and human osteosarcoma cells, it was found that larger channel diameter resulted in both increasing cell coverage and deeper penetration into the center of the scaffold [56]. Furthermore, it was also found that there was a minimum level of channel diameter required for cell penetration (82 μm) [56]. Similarly, in another study human osteoblasts were shown to penetrate channels over 20 μm, but a pore size of 50 μm was required to support new bone formation through the channels [60]. This study indicated that the minimum channel size might vary with the dimension and material of a scaffold, as interconnectivity fosters not only cell infiltration but also vascularization and nutrient transfer, highlighting the need for controlled scaffold interconnectivity.

Scaffold degradation impacts ingrowth as well, therefore this factor needs to be considered in tandem with interconnectivity for optimal tissue formation. Due to the complexity of the network inside of a scaffold, pore interconnectivity can be difficult to assess, but the use of micro-CT to quantify pore interconnectivity allows for a more precise definition and better assessment of scaffold characteristics [61-63]. Precise scaffold interconnectivity is difficult to create using traditional scaffold fabrication techniques, thus advanced scaffold manufacturing may be necessary to achieve repeatable interconnectivity. Advanced manufacturing techniques include scaffolds made through the use of rapid prototyping, which is also known as solid freeform fabrication (SFF) and additive manufacturing. In one example of enhanced scaffold interconnectivity using SFF, poly(lactic-co-glycolic acid) (PLGA)- ß-TCP scaffolds were fabricated using the commercially available TheriForm^{TM} 3D printing process (3DP) [28]. In order to test the effect of interconnected continuous channels

on bone ingrowth, scaffolds were manufactured either with macroscopic channels or a microscopic porosity gradient. Using a rabbit cranial defect model, histomorphometric analysis after 8 weeks of implantation demonstrated that scaffolds with macroscopic channels had a higher new bone area than both the scaffolds

Scaffold Materials	*Function and Biological Improvements*	*Reference*
PLG	Faster colonization in scaffolds with large scaffold interconnectivity. No change observed in gene expression levels of vinculin, β-actin, OC or OP with changes in scaffold interconnectivities.	[58]
Silk Fibroin	Interconnectivity influences morphology of *in vitro* bone growth of hMSCs but not ALP protein expression.	[55]
HA	*In vitro* cell penetration enhanced by large interconnected channels, established minimum channel size of 80 μm for cell penetration.	[56]
	Enhancement of bone ingrowth observed in channels over 100 μm. Micro CT used to assess bone growth.	[61, 62]
	Scaffolds manufactured using solid freeform fabrication. Geometry of channels influence *in vivo* bone growth.	[24]
	Scaffolds formed from mold using SLA. Individual channels should be interconnected for increased bone growth.	[25]
HA/ß-TCP	Osteoblasts could penetrate channels as small as 20 μm but not form bone until channel diameter reached 50 um. Also observed changes with material type.	[60]
Titanium	Length and size of pore connection to surface of scaffold influenced amount of bone ingrowth.	[63]
PLGA/ß-TCP	Scaffolds manufactured using solid freeform fabrication. Macroscopic channels guide bone growth and dictate tissue type produced.	[28]

Table 3: The Effect of Interconnectivity on Osteogenic Signal Expression and Differentiation

without channels or the defect without any scaffold. These results indicated that *in vivo* bone formation was guided down the channels of the scaffold. Furthermore, the porosity gradient of the scaffold was shown to dictate the type of tissue that was produced, as only soft tissue was produced outside the radial channels of the scaffold. This suggests that the precise architecture of a scaffold can be used to guide tissue growth [28].

By manipulating the porosity and interconnectivity, the rate of bone tissue regeneration may be enhanced. Based on an *in vivo* study utilizing HA scaffolds fabricated by 3DP and rabbit cranial defects, it was suggested that the direction and the extent of void space in the scaffold might influence new bone formation [24]. Histological evaluation indicated that the channels direct the growth of new bone as radial channels penetrating from the sides of the scaffold were shown to successfully guide bone from the surrounding tissue and axial channels extending inward from the bottom of the scaffold directed the migrating cells into the center of the scaffold. This study provided even further evidence that *in vivo* bone growth could be influenced by the scaffold architecture and interconnectivity. Moreover, a similar result in regards to controlling *in vivo* bone growth through scaffold architecture and interconnectivity was observed in SLA-fabricated HA scaffolds [64]. To investigate *in vivo* performance of channel directions, scaffolds with orthogonal or radial channels were implanted into porcine mandibles. The scaffold architecture was shown to influence the amount of regenerated bone as the orthogonal scaffolds exhibited larger bone growth area than scaffolds with radially-oriented channels. The lack of interconnectivity between the individual channels might explain the reduced

bone growth in radially-channeled scaffolds. In addition, it appears that the architecture in the porous regime might influence bone geometry as bone formation was integrated throughout the orthogonal HA scaffolds while the bone in the radial scaffolds formed in an intact piece in the center of the scaffold [64]. These studies may validate the use of scaffold interconnectivity and architecture can be used to guide bone growth and enhance *in vivo* bone tissue regeneration. Additional work using scaffolds with highly characterized and controlled interconnectivity should be completed to further elucidate the connection between the two.

2.2.3. Mechanical stiffness and mechanosensing

Dynamic cell-ECM interaction may regulate initial cell attachment, proliferation, differentiation, and osteogenic and chondrogenic signal expressions. Among a variety of scaffold design parameters, including pore geometry and interconnectivity, substrate stiffness (rigidity) is another critical factor governing cellular behavior in terms of mechano-transduction and cell-matrix interaction. There have been many studies of the effect of substrate stiffness on the cellular behaviors in several tissue types including bone [65], the central nervous system [66], the cornea [67], and kidney epithelial cells [68]. Different tissues present characteristic elasticities, ranging from ~1 kPa in the brain to 100 kPa in collagenous bone. The specific type of cells in each tissue favored to differentiate into different lineages depending on the scaffold's mechanical stiffness [69]. Recent studies have revealed that the substrate stiffness is directly related to the specific differentiation cascades that an MSC population undergoes. Therefore, the mechanical properties of a

scaffold could be another critical parameter in designing the optimal 3D scaffold for bone tissue engineering (See Table 4).

It has been investigated that the responses of osteoblast cell populations could be affected by intrinsic ECM mechanical properties [22]. In this study, polyacrylamide hydrogels were functionalized with type I collagen and fabricated with various Young's moduli depending on the amount of crosslinker, N,N'-methylene-bis-acrylamide. The substrate stiffness ranged from 11.78 to 38.89 kPa by varying the amount of crosslinker from 0.1 to 0.3 %. When the collagen density was low, the proliferation of MC3T3-E1 cells was higher on a rigid polystyrene (PS) substrate than on the softest gel and the random motility speed of cell migration was also faster on PS than on a soft substrate. The result suggested that the modification of ECM mechanical properties might influence the contractility in the actin cytoskeleton, and immature focal contact and cytoskeleton development in the softest gel could verify this rationale. Moreover, both focal adhesion kinase (FAK) activity measured by detecting phosphorylated Y397-FAK and mineralization determined by qualitative Von Kossa staining demonstrated that signaling mechanisms of cell-ECM and osteogenic phenotypic differentiation were modulated by the ECM stiffness. A similar study has shown that cellular responses to scaffold mechanical properties may regulate the osteogenic differentiation by modulating the mitogen-activated protein (MAPK) and the extracellular signal regulated kinase (ERK) activity [16, 70]. The results demonstrated that osteogenic differentiation of MC3T3-E1 cells cultured on mechanically tunable poly(ethylene glycol) (PEG) hydrogels could be regulated by substrate rigidity. In particular, phosphorylation of p44/42 MAPK was enhanced as

the rigidity increased and this regulation of MAPK activity might be related with upregulation of ALP activity as well as the OC and BSP gene expression level [70]. In addition, it was also found that altered ECM mechanics activates the FAK activity through integrin-mediated signal transduction [16]. Enhanced FAK activity stimulates Ras homolog gene family, member A (RhoA)/ Rho-associated, coiled-coil containing protein kinase 1 (ROCK) activity, and this signal subsequently stimulates the ERK/MAPK kinase. Finally, Runx2 in a nucleus is activated and osteogenic gene expression including OC, BSP, and ALP may be upregulated. This sequential signal transduction triggered by matrix stiffness would ultimately lead to osteogenic differentiation of cells on the substrate material. Furthermore, stiffness dependent osteogenic signal expression was also observed in embryonic stem cells [71]. The expression levels of osteogenic marker genes including Runx2 and OP were dependent on the surface Young's modulus of collagen coated PDMS substrates. Upregulation of the primitive streak and mesoderm precursors including forkhead transcription factor (Foxa2), Brachyury, Mix 1 homebox-like 1 (Mixl1), cadherin-2 (Cdh2), and eomesodermin homolog (Eomes) was observed. In addition, mineralization assessed by alizarin red S was also positively correlated with the stiffness substrates from 0.041 to 2.7 MPa.

However, downstream differentiation of cells and changes in phenotype do not solely depend on mechanical cues that the cell receives from a scaffold, but also on a combination of factors of the cell's physical, chemical, and biological ECM properties. Rowlands *et al.* demonstrated that varying substrate stiffness could regulate the human MSC differentiation into either osteogenic or myogenic lineages

[72]. In this study, polyacrylamide gels coated with ECM proteins including collagen I, collagen IV, laminin, and fibronectin were investigated. Physiologically relevant stiffness (0.7 to 80 kPa) was obtained by crosslinker fraction and cultured MSCs exhibited different levels of Runx2 and myogenic differentiation1 (MyoD1) expressions, which represented osteogenic and myogenic transcription factors respectively. Specifically, the substrate model with an 80 kPa of modulus and a collagen type I coating showed the highest expression level of both transcription factors. This might suggest that mechano-transduction is related to both scaffold stiffness and adhesive ligand presentation on the ECM. This observation was also made in 2D gel systems as the osteoblastic function of cells was altered by changing type I collagen density [22] and other ECM protein coatings [73].

In addition to osteoblastic cells, smooth muscle cells have been observed to exhibit similar behavior on substrates with varying stiffness [74]. In this study, 3D crosslinked PEG-fibrinogen hydrogel encapsulating cells exhibited 4.48 to 5.41 kPa of compressive modulus. This range of stiffness in the 3D environment appeared to modulate cytoskeletal assembly. From this research, it may be suggested that small changes in the mechanical stiffness of scaffold materials may alter the biological functions and phenotype of transplanted cell populations. Another fundamental finding of this study was a synergetic effect between substrate stiffness and RhoA activation appears to be critical to the regulation of cytoskeletal contractility. As shown in another study, cell shape and morphology and the subsequent changes in contractility may regulate the downstream cell functions [75].

2.2.3.1. Crosslinking density

Mechanical properties of 3D polymeric scaffolds such as compressive modulus could be controlled by changing the crosslinking density during fabrication or by varying the ratio of composite filler materials. For instance, crosslinking density of polyester scaffolds fabricated with D,L-lactide, ε-caplolactone, and trimethylene carbonate could be controlled by varying the composition of copolymers and the type of initiator, and therefore the degradation ratio, as well as the compressive modulus, of scaffolds could be also varied [76]. Similar to the modulation of crosslinking density of 2D gel systems described previously, the amount (or the ratio) of crosslinker within polymeric matrices could be used to control the modulus of porous scaffolds. In addition, a study of poly(propylene fumarate) (PPF) photocrosslinking characteristics also demonstrated that mechanical properties could be controlled by fabrication parameters including the molecular weight of the PPF polymer, photoinitiator content, and the amount of the present diester precursor, diethyl fumarate (DEF) [77]. In this study, sol fraction, swelling degree, elastic modulus, and fracture strength were examined based on the factorial design of three fabrication factors. In particular, the results indicated that varying these factors could control crosslinking and compressive mechanical properties. Moreover, this study exhibited the feasibility of PPF/DEF mixture for the reduction of viscosity to use PPF as an SLA resin material and the suitability of this polymer network with compressive strength for trabecular bone replacement. Thus, controlling the crosslinking density of the polymer network could change the

mechanical stiffness of a scaffold, and this controllability could be utilized in SLA-rendering.

2.2.3.2. Filler incorporation:

Another method to control the stiffness of 3D scaffolds is incorporation of fillers into polymeric scaffold resins. For example, the gelatin scaffold incorporated with ß-TCP also exhibited varying compressive modulus from 0.27 (no ß-TCP incorporation) to 4.97 MPa (90 wt% of ß-TCP) depending on the amount of ß-TCP particles [78]. The highest ALP activity and OC content of rat MSCs were observed in 50 wt% of ß-TCP, and it could be concluded that the composition ratio of composites might change the compressive modulus of a 3D scaffold, and the expression of osteogenic marker proteins might be related to this ratio with the threshold up to 50 wt%. Similarly, when chitosan was incorporated in PLGA polymeric scaffolds, increasing the chitosan/PLGA ratio resulted in increasing adhesion efficiency of seeded rat bone marrow stromal cells (BMSCs) as well as increased calcium deposition, which indicated that the majority of cell population underwent osteogenic differentiation [79]. In addition to mineral particle incorporation, microfabricated SU-8 microrods (15 x 15 x 100 μm) in a 3D commercialized Matrigel might result in increasing stiffness of the 3D matrix and influence the fibroblast attachment pattern [80]. Given changes in morphology and cytoskeletal architecture, the mechano-transduction mechanism might be altered and the signal expression profiles of human MSCs cultured in this matrix system

exhibited upregulation of ACTR and PHACTR as well as downregulation of collagen I and BMP-6 expression [81].

However, incorporation of filler material into polymeric resin may alter not only the stiffness of composites but also the surface characteristics including topology, roughness, passive adsorption of soluble contents, and the overall scaffold's chemical composition [82, 83]. In addition to changing the mechanical stiffness by incorporating filler material into polymeric scaffolds, controlling of physico-chemical surface properties may facilitate the interaction of hosted cell population and a scaffold. Inorganic particle incorporation of ß-TCP or HA provides a biochemical environments that closely mimics native bone, and this might result in dynamic interaction of Ca^{2+} ions with the seeded cells [84] as well as *in vivo* tissue regeneration [8, 85].

2.2.3.3. Collagen

Since collagen is an important ECM protein found in the native bone, its structural properties have been researched in bone tissue engineering in order to lead to skeletal tissue regeneration strategies [86]. Therefore, the proper production and crosslinking of collagen in the ECM environment could lead to osteogenic differentiation of recruited cells [87]. The stiffness of the collagen matrix has also shown that it functionally stimulates implanted cell populations [88, 89]. The compressive modulus of collagen-GAG scaffolds could be controlled by varying the collagen amount as well as by altering the dehydrothermal (DHT) crosslinking process [89]. Specifically, the 1% collagen-GAG scaffolds that were treated with a

higher crosslinking temperature exhibited increased cell numbers and metabolic activity up to 7 days after culture. Another study using a dense collagen matrix showed upregulation of osteogenic signal expression in primary mouse calvarial osteoblasts [88]. Osteogenic differentiation of cells in the matrix were verified through the observation of increased expressions of ALP and BSP in the first 7 days of culture in osteogenic supplemented media which was compared to culture on a 2D plastic surface.

It might not be concluded that the stiffness or compressive modulus of scaffolds directly govern the specific signal expressions that would bring about bone tissue differentiation cascades. The complex signal transduction involved in osteogenesis is dynamically related to cell-cell and cell-ECM interaction as well as intracellular mechanisms. However, the combinational approaches of controllable mechanical strength and other stimulatory factors such as ECM protein incorporation and topological changes of the substrate surface may allow manipulation of the level of expressions of osteogenic signals and, eventually, differentiation. Given this concept, SLA can also be applied to create the tunable stiffness or other mechanical characteristics in 3D bone tissue engineering scaffolds.

Scaffold Materials	*Function and Biological Improvements*	*Reference*
Polyacrylamide gel	Tunable stiffness by varying the amount of crosslinker. Proliferation of MC3T3-E1 cells and random motility speed, FAK activity, and mineralization could be affected by substrate stiffness.	[22]
	Controlling the ECM stiffness and incorporation of ECM protein may regulate the human MSC differentiation into osteogenic and myogenic lineages.	[72]
PEG hydrogel	ECM rigidity may regulate ALP, OC, and BSP expression via MAPK activation. Sequential activation of FAK, RhoA/ROCK, ERK/MAPK by controlling ECM rigidity.	[16, 70]
2D Polystyrene	Stiffness dependent osteogenic signal expression and mineralization in embryonic stem cells.	[71]
PEG-fibrinogen hydrogel	Modulation of cytoskeletal assembly of smooth muscle cells by varying the stiffness. Synergetic effect of stiffness and RhoA activation on cytoskeletal contractility.	[74]
Polyester copolymer	Controllable crosslinking density by varying the composition of copolymer and the type of initiator.	[76]
Gelatin/ß-TCP	ß-TCP amount may affect compressive modulus, ALP activity and OC expression.	[78]
PLGA/chitosan	Cell adhesion and calcium deposition could be affected by PLGA/chitosan ratio.	[79]
Matrigel with microfabricated SU-8	mRNA expression of osteogenic signals of human MSC may be influenced by embedded SU-8.	[81]
Collagen-GAG	Tunable compressive modulus of scaffolds through DHT crosslinking process.	[89]
Denser collagen matrix	Denser collagen matrix exhibited increased expression of ALP and BSP.	[88]

Table 4: The Effect of Mechanical Stiffness on Osteogenic Signal Expression and Differentiation

2.3. Computer Aided Rapid Prototyping

Stem cell-based tissue engineering approaches may benefit from optimization of scaffold design parameters with the aid of chemical and biological stimuli in order for the stages of cell proliferation and osteogenic differentiation during *in vitro,* as well as *in vivo* osteogenesis. As discussed above, the architectural parameters, including porosity, pore size, interconnected channel geometry, chemical properties such as crosslinking density, and mechanical cues such as stiffness, are important factors for bone scaffold fabrication. These factors might stimulate cell responses including the signal expressions facilitating cell differentiation. Due to the variations observed when altering these factors, it is necessary to first define the optimal values of parameters to enhance cellular responses. Then, accurate fabrication and continuous production of the scaffolds with the optimal architectural, chemical, and mechanical parameters could justify extending the use of bone tissue engineering to clinical regenerative medicine with improved levels of bone regeneration at implanted sites. Therefore, computer aided rapid prototyping (CARP) is considered to meet these criteria with sufficient control in scaffold preparation to provide improved tissue regeneration, proper vascularization after implantation, and sufficient tissue integration with scaffold degradation. The CARP process produces scaffolds layer by layer through SFF with design parameters inputted from computer aided design (CAD) software. Precise control of these parameters is the most significant advantage of CARP, thus when designing a scaffold's inner architecture the ability of the design to influence the forming bone geometry should be considered in addition to its effects on osteogenesis [90].

Another advantage of CARP for the fabrication of scaffolds is its feasibility of patient- and defect-specific design of bone implants [91, 92]. SFF includes several types of commercially or readily available techniques that have been utilized to produce directly implantable tissue engineered (*i.e.,* resorptive) implants [29, 93]. 3D Printing (3DP^{TM}, Therics Inc., Princeton, NJ) injects a liquid binder, which may contain cells and/or growth factors, into a powder [94]. Fused deposition modeling (Stratasys Inc., Eden Prairie, MN) uses an inkjet to extrude material that is heated just above melting temperature [95]. 3D Plotting is another heat-based extrusion technique [96]. In selective laser sintering (3D Systems, Rock Hill, SC), a laser is used to sinter powder, layer by layer, into a plastic part [97]. Selective laser melting (MTT, Staffordshire, UK) uses a laser to sinter metal powders [98]. Solidscape (Merrimack, NH) devices print an implant shape in wax that can then be replaced with resorbable materials [99]. Soft lithography (Nanoterra, Cambridge, MA) [100] and electrospinning [101] are technologies that can produce very high resolution surface features, such as roughness on a scale relevant to cells.

2.4. Stereolithography

One of the most researched SFF methods is stereolithography (3D Systems, Rock Hill, SC), which utilizes a laser to crosslink photo-polymerizable polymers and fabricate 3D parts by vertical layering [102]. Figure 1 shows a schematic of SLA fabrication. The modeling of pore structure in porous tissue engineered scaffolds was highlighted in elsewhere [29]. Therefore, SLA is a useful strategy to fabricate precisely designed scaffolds with defect site-specific external shape based on a

patient's 3D CT scan, as well as parameters such as pore size, porosity, interconnectivity, and mechanical stiffness optimized to influence osteogenic signal expression and differentiation (See Table 5).

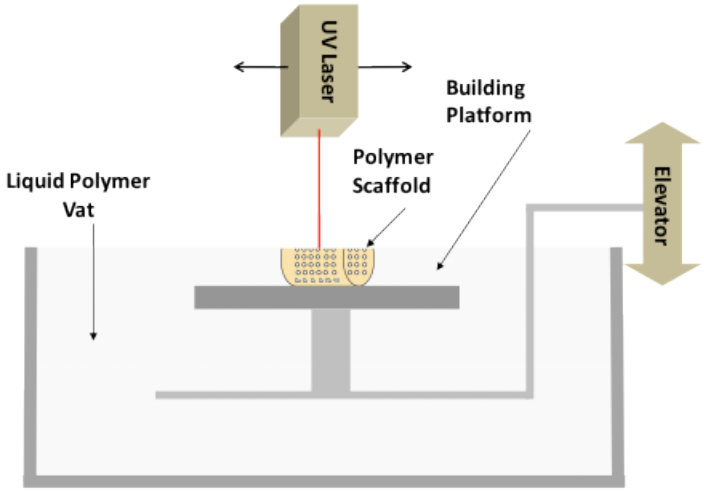

Figure 1: A schematic of the stereolithography process. A laser crosslinks the liquid polymer at the surface of the polymer vat to computer inputted pecifications by moving in the x and y directions. Following completion of a layer the elevator lowers the completed scaffold one layer in the z direction and the process repeats.

2.4.1. Poly(propylene fumarate)

PPF is one of the most studied biodegradable and photocrosslinkable polymers [38, 77]. With the aid of the photoinitiator, bis(2,4,6,-trimethylbenzoyl) phenylphosphine oxide, PPF chains can be crosslinked into networks. Due to the controllability of PPF photocrosslinking characteristics and mechanical properties as well as the suitable mechanical strength of UV crosslinked PPF networks [77], a mixture of PPF and DEF has been investigated for use as an SLA resin material. DEF is added as a solvent to reduce the viscosity, an important criterion for a device with moving part. This has allowed the control of pore size as well as channel and

wall thickness features in the hundred micron range [102-106]. By utilizing a commercially available laser curing device, an SLA 250/40 (3D systems), the first tissue engineering study to fabricate PPF scaffolds with controlled geometry designed using CAD software was published in 2003 [102]. An example of a CAD file prior to SLA scaffold fabrication is shown in Figure 2. Figure 3 shows scanning electron microscope (SEM) images of the morphology of controlled architecture 3D PPF/DEF scaffolds with continuous channels, which were fabricated by 3D systems Viper. In addition, it has been shown that a PPF/DEF mixture could be applicable to both SLA [104, 105] and other SFF methods such as 3D printing and injection molding [106]. Recent work has demonstrated the feasibility of surface modification of scaffolds by soaking them in a concentrated inorganic ion solution [103]. Moreover, controlling the degradability by varying the molecular weight of PPF during the synthesis could be a clinical advantage facilitating neobone development and complete resorption of implanted scaffolds [107]. Given this controllable degradability, PPF polymer with a low number average molecular weight (< 800 Da) has been researched [108].

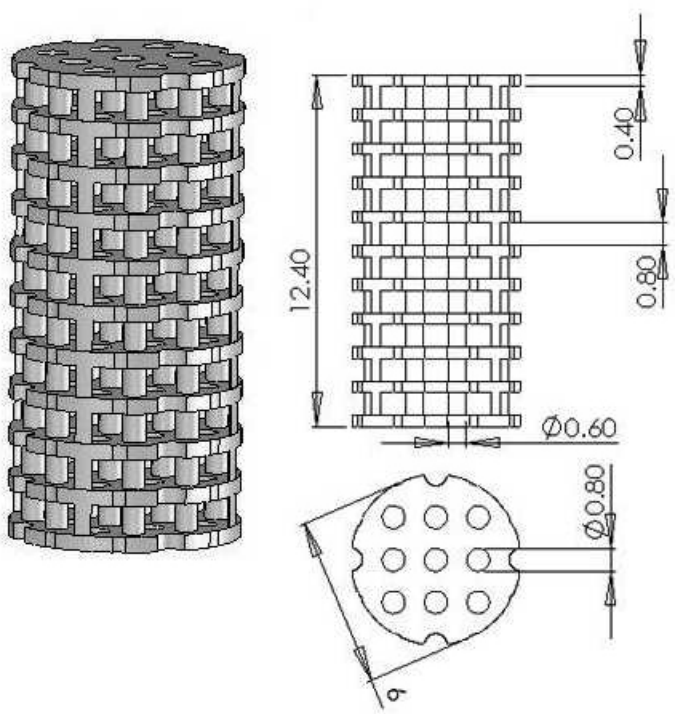

Figure 2: An example of a CAD file prior to the scaffold fabrication by SLA. Dimensions of total length, plate thickness, gap between plates, pole diameter,and pore diameter are in mm.

Top View

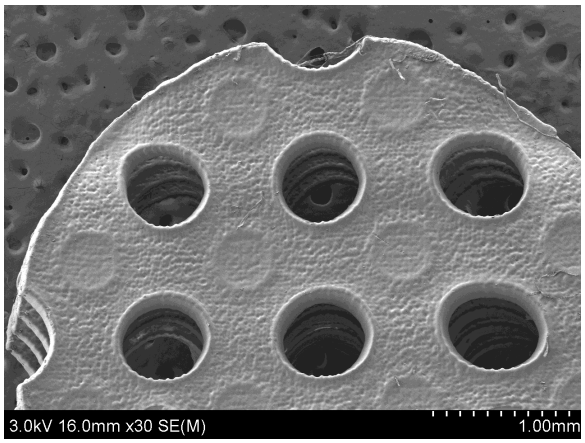

Side View

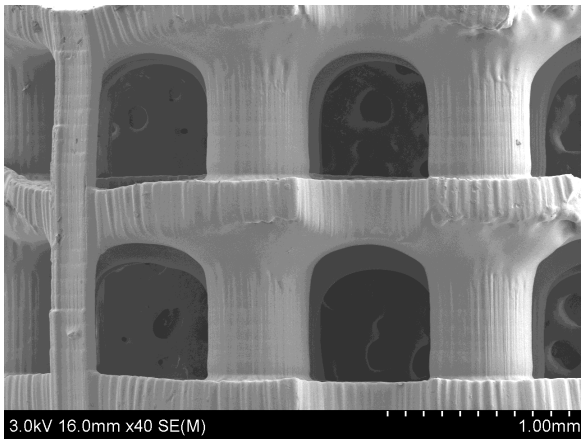

Orthogonal View

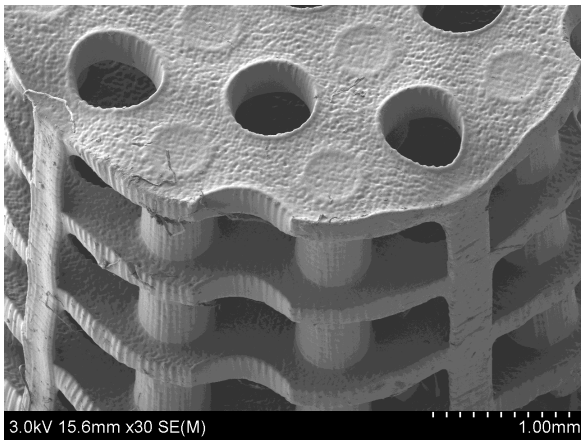

Figure 3: SEM images of SLA fabricated PPF/DEF scaffolds. Images show continuous channel geometry of scaffold architectures.

2.4.2. Other polymeric scaffolds fabricated by SLA

A series of recent studies investigated the fabrication of scaffolds with controlled geometry using several types of resin materials and *in vitro* cell attachment was assessed. Fumaric acid monoethyl ester (FAME) functionalized with poly(D,L-lactide) (PDLLA) oligomers has been used to create a gyroid architecture [109]. N-Vinyl-2-pyrrolodone (NVP) was used as the accelerator and Lucirin TPO-L was used as the photoinitiator. Initial *in vitro* data demonstrated that mouse preosteoblasts could adhere and spread on this scaffold. Another gyroid scaffold fabricated with PDLLA have also exhibited M3TC3 cell adhesion on day 1 [110]. SLA fabrication might also allow control of surface features of 3D porous scaffolds to provide a favorable environment for bone tissue formation [111]. Nano-fibrous poly(L-lactic acid) (PLLA) scaffolds have been developed with a micro pore structure in the struts that mimics the morphological function of type I collagen and significantly increased surface area compared to a solid-walled scaffold. These nanofibrous scaffolds with rectangular channels were created by using an SLA-fabricated negative mold and thermal phase separation of PLLA solution. Interestingly, mRNA expression levels of OC and BSP of MC3T3-E1 cells in fibrous scaffolds were higher than solid-walled scaffolds after 2 and 6 weeks of culture. Furthermore, one recent study has revealed that the critical importance of 3D porous scaffold structural cues to induce *in vivo* bone regeneration [112]. In addition to the importance of the design and fabrication of accurate morphology of implantable bone substitutes [113], it is also essential that the internal geometry closely mimic the native bone tissue in order to induce bone ingrowth. The inverse trabecular inner architecture of SLA-fabricated polybutylene

terephthalate (PBT) scaffolds designed from micro-CT scans of a native cadaveric canine femur exhibited up to 6 times higher bone growth into and adjacent to the scaffolds compared to simple porous scaffolds [112]. This study emphasized that macroscopic structural characteristic, specifically inner pore architecture, might facilitate accelerated bone regeneration, specifically inner pore architecture.

2.4.3. Photopolymerized hydrogels

In addition to controlled design of macroporous scaffolds, SLA can be applied to photopolymerized hydrogel systems. For example, 2D patterning on bilayer films has been achieved via soft-photolithography stamping and micro-patterning of interpenetrating polymeric network within 3D hydrogels of collagen and hyaluronic acid was also investigated. This technique may allow the zonal differential distribution of several scaffold properties within a bulk hydrogel, including crosslinking density, swelling degree, water content, and mechanical stiffness [114]. Cell encapsulation within a photopolymerized hydrogel has also been developed. 3D Poly(ethylene oxide) (PEO) hydrogel encapsulating Chinese hamster ovary cells were fabricated using a commercially available SLA process. This hydrogel system exhibited elastic mechanical property similar to soft tissues along with high viability of the encapsulated cells on day 2 [115]. PEG can be crosslinked into a hydrogel by the incorporation of acrylate or methacrylate as photoreactive and crosslinkable groups. Photoencapsulated MSCs in PEG-diacrylate (PEG-DA) hydrogel exhibited chondrogenic differentiation for 6 weeks [116], and encapsulation of human dermal fibroblasts in PEG-dimethacrylate (PEG-DMA) hydrogel could be also accomplished

with SLA [117]. Furthermore, this method can be applied to functionalization of the PEG hydrogel with arginine-glycine-aspartic acid (RGD) ligands for specific localization of cells [118]. These studies have shown the possibility of multi-material spatial control using SLA. Therefore, an SLA fabricated hydrogel containing an encapsulated cell population may be a promising technique for providing sufficient cell mass for large constructs. Moreover, Mapili *et al* have demonstrated spatiotemporal incorporation of a variety of materials within 3D PEG-DMA scaffolds fabricated by SLA [119]. Fluorescently-labeled polymer microparticles such as FITC or Cy5 labeled latex particles were spatially patterned in the scaffold layers. Fibronectin-derived peptides and heparin sulfate have also been successfully conjugated in the scaffold material. This result illustrated the capability of SLA for the accurate distribution of multiple factors such as growth factors within the scaffolds by point-by-point photopolymerization, resulting in a hybrid tissue structure.

2.4.4. Hydroxyapatite materials

HA is one of the most intensively researched bioceramics in bone tissue engineering due to its biocompatibility as well as physical and chemical similarity to the inorganic compound in the native bone tissue [120]. Although SLA has been traditionally applied to synthetic polymeric resins to create 3D complex architectures, recent studies have demonstrated the feasibility of controlled HA scaffold design. While the direct photopolymerization of polymeric resin results in simultaneous scaffold fabrication, controlled architecture of HA scaffolds are usually fabricated

from a negative mold prepared via SLA as well as the casting and subsequent curing of a suspension containing HA, dispersant, monomers, and initiators [121]. Goat BMSCs seeded onto the HA scaffold fabricated by this technique showed *in vitro* proliferation on the exterior surface of these scaffolds over 7 days and methylene blue/basic fuchsin-stained histology data indicated that the mineralized bone tissue was observed after 6 weeks of subcutaneous implantation in athymic nude mice.[99] Another *in vivo* study using designed HA scaffolds in a minipig model demonstrated that the overall shape of regenerated bone tissue may depend on the architecture of scaffold internal channel geometry [25].

Furthermore, HA could be used in composite fabrication with photocurable acrylate resins [122, 123]. In these studies, micron-sized HA particles were incorporated with olygocarbonate dimethacrylate (OCM) resin material, and simple stirring created homogenous mixture of HA particles and resin polymers, which blocked the inhibition of photocrosslinking by solid particles. Although increasing the amount of HA particles might limit the versatility of SLA fabrication due to increased viscosity, the result of 4 and 8 week *in vivo* studies on distal epiphysis implants in rat femora exhibited extensive periosteal and endosteal osteogenesis, as observed by SEM of sectioned tissue samples [123]. In addition, cell attachment measured by propidium iodide staining and proliferation assessed by DNA contents showed higher levels in composite scaffolds than in the control OCM scaffold [122]. Similarly, bioactive glass has also been used for the fabrication of CAD scaffolds with the aid of the combined methods of both SLA and gel-casting [124]. An SLA-produced epoxy resin negative mold with controlled architectures was used to cast

Scaffold Materials	*Function and Biological Improvements*	*Reference*
PPF	Controllable mechanical properties and crosslinking characteristics of PPF/DEF/photoinitiator mixture.	[77]
	Initial trial of PPF resin by using a commercialized SLA machine (3D systems).	[102]
	Surface modification after scaffold fabrication.	[103]
	Fabrication of controlled architecture with 250 ~ 260 μm pore size and 132 ~ 143 μm line width.	[104]
	Utilization of PPF with low number average molecular weight (less than 800 Da).	[103, 107]
PDLLA/NVP	FAME functionalized PDLLA/NVP could be used with SLA resin material and aid of accelerator / photoinitiator to form 240 ~ 350 μm pore sizes in gyroid structures.	[109]
PDLLA	Formed scaffold with 73 vol % porosity and 170 ~ 240 μm pore size in gyroid structures.	[110]
PLLA	Used a negative mold fabricated by SLA. Upregulation of OC and BSP mRNA expression in nanofibrous scaffold with microporous surface features.	[111]
PBT	The inverse trabecular inner structure from a native canine bone tissue was fabricated by SLA. Intensive bone growth *in vivo* compared to random porous design of scaffolds	[112]
Collagen/hyaluronic acid hydrogel	Zonal micropatterning in a bulk hydrogel with 500 μm thickness.	[114]
PEO gel	Cell encapsulation in a PEO gel using SLA. Encapsulated CHO cells were viable on day 2	[115]
PEG-DA	Chondrogenic differentiation of MSCs encapsulated in PEG-DMA gel.	[116]
PEG-DMA	Viable human fibroblast encapsulated in PEG-DMA gel.	[117]
	Spatial control of multiple materials including RGD ligands and fluorescently labeled microparticles by SLA.	[118, 119]
HA	Using a negative epoxy mold fabricated by SLA.	[121]
	In vitro proliferation of BMSCs and mineralized bone tissue formation were observed.	[99]
	Composite fabrication with photocurable acrylate resin.	[122, 123]

Table 5: Recent Development of Stereolithograpy in Bone Tissue Engineering Research

a homogeneous suspension of a glass slurry. This material was then cast in this mold. It has been hypothesized that bioactive glass material is biocompatible like HA [125], could control osteogenic differentiation, and could bring about osteogenic gene expression [126-128]. These indirect fabrication techniques using an SLA fabricated mold and ceramic suspension have shown the versatility of controlled architecture manufacturing and its application in animal models.

2.5. Clinical Approaches utilizing SLA

Since 1987, 3D CT-scans of the skull have been used for maxillofacial preoperative planning [129]. Indeed, SLA-derived models have become widely used in the preparation of surgical guides or for planning the manipulation of boney and/or soft tissue structures [130]. More recently CAD techniques have been used to model [131-133] the performance of inert [113] and tissue engineered implant models that are to be produced via SFF techniques.

2.5.1. Limitations

The clinical application of SLA fabricated scaffolds involve several critical steps, including (1) scaffold manufacturing based on 3D CT images, (2) virtual surgical procedure simulation and validation, and (3) the final surgical procedure of implantation [91, 92, 129, 134]. Specifically, the first step of scaffold fabrication using SLA includes data acquisition from CT images of the defect site of patients,

virtual model reconstruction using computer software, physical 3D scaffold manufacturing using SLA, and 3D model validation. Therefore, for the successful manufacturing of 3D SLA scaffold architectures, close cooperation of surgeons and tissue engineers is of critical importance. However, research into SLA scaffolds is still limited to fabrication itself and simple *in vitro* (cell attachment) or *in vivo* (animal trial) studies, rather than successful surgical implantation into defect sites in human clinical trials. Moreover, a variety of technical limitations still remain unsolved [135, 136]. During the step of image acquisition, CT data import error may occur when determining the pixel size and slice thickness and numerical errors in this step may lead to incorrect virtual reconstruction. Moreover, other drawbacks on obtaining CT data from the patient are also reported such as inhibition of metal or other implant material on the patient's body due to the signal intervention and patient's movement during the CT scan. In addition, during the step of scaffold manufacturing, model stair-step artifact and irregular surface feature may also be found [136, 137]. Furthermore, the degree of skin contractures can become an issue for surgical procedures [92, 135]. Since obtaining the accuracy of both external implant surface geometry is critical for fitting the implant into the defect sites while the inner pore architecture of a 3D scaffold is related to promoting host tissue ingrowth, the technical difficulties related to scaffold fabrication will need to be addressed in the future. Due to these complex limitations as well as the limited numbers of clinically available biomaterials for the implantable scaffold fabrication, the number of reports about surgical implantation using SLA-manufactured scaffold is few. Clinical use of SLA is currently restricted to models based on CT images of a

patient's defect for guidance and planning of surgery, which is beneficial on preoperative evaluation [138-140].

2.5.2. The Current Clinical Use of Computer Aided Design for Bone Implants

Dean et al presented CAD of cranial implants [91] and the CAD models that were rendered using SFF were then recast in implantable materials, such as PMMA [92, 137] or titanium. The milling of titanium (inert) prosthetic cranial plates has been demonstrated [141-143] and the performance of these implants and standard of care procedures was compared [144]. In addition, the level of post-operative complications in patients receiving custom cranial implants following decompressive craniectomies was also considered [145]. Research into the use of CAD for hip or knee implants has also been completed. The advantages of patient specific knee implants was discussed, however the expense may prevent access to these implants [146]. It was suggested that custom hip implants were useful for patients with distorted anatomy [147], but the benefit of patient-specific hip implants was also questioned elsewhere [148]. Moreover, the advantages of custom patellofemoral implants were found and it was predicted that this work will shift towards the use of resorbable materials [149, 150]. The use of CAD for cervical spine drill guides and resorbable, patient-specific plating has also been studied [151, 152].

2.6. Summary

In bone tissue engineering, a series of structural cues including pore size, porosity, interconnectivity, and stiffness have been found to be critical factors in activating osteogenic signal expression. Successful manipulation and fabrication of controlled architecture with optimal conditions of construction parameters may stimulate osteogenic signal expression as well as subsequent osteogenic differentiation. To this end, SLA is a promising and feasible strategy for fabrication of a designed architecture, which may show the best performance *in vitro* and *in vivo*. Recently developed SLA-manufactured 3D scaffold systems have shown the possibility of clinical implantation. Therefore, controlling the structural parameters may promise successful integration of the implants into the surgical sites and enhancement of bone regeneration. Despite some limitations of a sequential procedure of the scaffold fabrication by SLA and the surgical implantation into humans, development in scaffold construction parameters and SLA fabrication is a promising means for the fabrication of functional bone tissue engineered substrates. These constructs facilitate osteogenic signal expressions and subsequent osteogenic differentiation of either scaffolds pre-loaded with cells or scaffold-recruited cells from surrounding tissues. Therefore, it is suggested that the following research should be completed to enable successful clinical implementation of implants manufactured via SLA:

(1) Scaffold parameters: extensive investigation optimizing the individual scaffold design parameters and subsequent studies to find synergistic versus negative effects of a combination of individual parameters.

(2) Bulk material production: continued development of human implantable (FDA approved) biomaterials and investigation of composite materials [153].

(3) Tuned SLA fabrication: Achievement of a higher precision of SLA to control the specific range (less than tens of micron level) of scaffold architecture, validation of accuracy of CAD scaffolds, and feasible reproduction of the scaffolds.

(4) Successful data acquisition from human patients: data acquisition using clinical visualization techniques and the transfer of this data to 3D images to reflect defect sites with higher resolution and minimal error.

(5) Clinical applications: more intensive case studies to accrue clinical information and to direct treatment.

Chapter 3: Nanoparticle Technology in Bone Tissue Engineering

3.1. Introduction

The three fundamental components of bone tissue engineering have been well described as (a) parenchymal or progenitor cells which subsequently express tissue matrix, (b) scaffolds which can act as temporary frameworks to support bone growth, and (c) growth factors to induce bone-forming cell regeneration. Although a number of investigations have been performed to elucidate these bone regenerative strategies, these approaches are often associated with limitations including improper mechanical strength of scaffold materials, insufficient cell growth for bone fracture-healing, and low growth factors expression to stimulate osteogenic differentiation and proliferation. In order to overcome these drawbacks, nanoparticle technology has been increasingly combined with bone tissue engineering methods. Nanoparticles, defined as a submicron-sized particle and typically less than 100nm in diameter, have enormous potential to be used as pharmaceutical, therapeutic, and diagnostic agents for biomedical applications as well as enablement of tissue engineering. Due to their extremely small size, surface-to-volume ratio, and surface functionality, nanoparticles may be one of the promising candidates to create novel composite materials and delivery system for bone regeneration. Therefore, this review provides the recent nanoparticle-based strategies utilized in bone tissue engineering applications.

As published in **K. Kim** and J.P. Fisher, "Nanoparticle Technology in Bone Tissue Engineering", Journal of Drug Targeting, 15:241-252 (2007).

In particular, we emphasize on three major areas of bone regeneration which have been recently studied by bionanotechnology: (1) nanoparticle-composite bone tissue engineering scaffolds with enhanced mechanical properties, (2) nanofibrous scaffolds that promote cellular functions and (3) nanoparticles that deliver osteogenic genes. Several examples in each area are explored and critically discussed in order to introduce the state of the art nanotechnologies that have been recently applied to bone tissue engineering.

3.2. Composite Scaffolds

3.2.1. Nanoparticle/Polymer Composite Scaffolds

Bone tissue engineering scaffolds are often designed to be mechanically strong, osteoconductive, biocompatible, and biodegradable. However, biodegradable polymeric materials or ceramics sometimes have significant limitations, including insufficient mechanical properties. Nanoparticles may be an excellent method to improve a tissue engineering scaffold's properties since they have similar length scale of many cellular and molecular components. Furthermore, as organic substances and inorganic minerals in bone formations exhibit nanoscale structures, nanosized materials may provide the proper surface and mechanical properties for bonding to surrounding tissue and supporting a loading condition [154]. Similarly, stress and strain balances between an implanted scaffold and the surrounding tissue are required for proper implant-tissue integration and sufficient bone regeneration [154]. Composite materials, such as a polymeric scaffold blended with nanosized material, can be a promising solution. In particular, a stronger interaction between nanosized

particles and the surrounding polymer material may result in better mechanical strength in the composite scaffold, while increased surface roughness may enhance osteoblastic functions. As a result, a number of investigations have been performed to develop nanoparticle-polymer composite materials.

Calcium phosphatase bioceramics, such as hydroxyapatite (HA) and tricalcium phosphate, are promising materials for bone tissue engineering since these ceramics reflect the chemistry and structure of the native mineral components of bone tissue. Despite the fact that bioceramics enhance osteodifferentiation and osteoblast proliferation, a number of limitations are associated, including brittleness, difficulty of processing, and slow degradation rate. Therefore, the incorporation of HA nanoparticles into a poly(ethylene glycol) (PEG) and poly(butylene terephthalate) (PBT) copolymer has been examined [155]. This approach attempts to combine the osteoconductivity of HA with biodegradability of polymer. Based on the finding that organic isocyanate groups can react readily with surface hydroxyl groups of HA, direct chemical bonding of HA particles with the surrounding polymer had a significant improvement on mechanical properties (Young's modulus, tensile strength, and elongation at a break) of the composites. Furthermore, composite scaffolds composed of HA nanoparticles and poly(L-lactic acid) (PLLA) showed not only increased compressive modulus, but also protein adsorption [156]. The incorporation of HA nanoparticles into the polymer scaffold altered the pore surface morphology of the composite scaffolds to be more suitable for protein adsorption, with the resulting properties dependant upon the ratio of HA and polymer. Higher porosity and refined microarchitecture are also associated with nanoparticle

composite scaffolds. In addition to bone binding ability of HA, mimicking the size scale of HA in natural bone may enable this composite scaffold to serve as a mechanically improved three dimensional substrate for cell attachment and migration. Alternatively, a poly(D,L-lactic-co-glycolic acid) (PLGA)/HA nanoparticle composite scaffold fabricated by gas forming and particulate leaching method improved mechanical properties and enhanced osteogenic potential in vitro and in vivo. This research also demonstrated that enhanced exposure of the bioactive HA particles allowed direct contact with cells and stimulated their proliferation and osteogenic differentiation [157]. 8 weeks after implantation of PLGA/HA composite scaffold into the succutaneous space of athymic mice [157] and to critical size defects in rat skulls [158], new bone with lamellar structure and osteoid formation was appeared. PLGA scaffold without HA had produced nearly no new bone in vivo and this indicated that the direct contact of cells with HA nanoparticles exposed on the scaffold surface may stimulate the cellular functions and enhanced bone regeneration.

Single-walled carbon nanotubes (SWNT) have also been incorporated in a nanocomposite scaffold in an attempt to take advantage of their significant mechanical properties and high aspect ratio. After modification of the side walls of SWNT, a cross-linked poly(propylene fumarate) (PPF) nanocomposite showed an increase in compressive/flexural modulus, compressive offset yield strength, and flexural strength when compared to pure PPF networks [159]. It was also demonstrated that functionalization might result in more monodispersed SWNTs in the PPF matrix than unfunctionalized SWNT composite. Significant enhancement in

mechanical properties may explained by the formation SWNT-PPF cross-links and resulting effective load transfer.

Silica nanoparticles may be the basis for an alternative approach for scaffold reinforcement. A silica nanoparticle composite with poly(ε-caprolactone) (PCL) exhibited improved mechanical strength and bioactivity [160]. The condensation reaction between the silanol groups in the silica and PCL end capped with triethoxysilane led to the formation of siloxane linkages and the reduction in the concentration of silanol groups in the composite. This structure resulted in an increase in tensile strength and Young's modulus of the composite, but a decrease in the initial rate of apatite formation. Overall, the enhanced mechanical properties were similar to those of human cancellous bone. Another example can be seen in a bisphenol-a-glycidyl methacrylate and calcium phosphate cement (CPC) composite with nano-silica-fused whiskers which exhibited significantly higher flexural strength than the composite containing only CPC fillers [161]. Results showed that the cytocompatible composite possessed enhanced flexural strength, elastic modulus and hardness that nearly matched cortical and trabecular bone. It was also demonstrated that the increased whisker surface roughness by nanozised silica conjugation may result in its retention in the matrix and substantially increase composite strength and toughness [162].

Metal nanoparticles have also been investigated as a mean to augment cellular responses in bone regeneration as well as to enhance the mechanical strength of the composite scaffolds. Nanocomposite reinforcement with a fine dispersion of alumoxane nanoparticles within PPF/PPF diacrylate has been described [163].

Alumoxane nanoparticles were hybridized with activating groups containing reactive double bonds and surfactant groups as separate ligands. This research reported that surfactant functional group improved the nanoparticle dispersion in the polymer matrix, which thereby enhanced the mechanical properties of composite, while activating groups provided additional covalent bonding with the control polymer. Significantly, the resulting 3-fold increase in flexural modulus of the nanocomposite compared to the polymer may allow the composite material to be utilized in load-bearing hard tissue engineering applications. Similarly, a poly(methyl methacrylate) (PMMA) scaffold containing nano-sized titania particles showed superior osteoconductivity and compressive strengths [164]. The effect of nanophase alumina and titania has also been investigated in vitro and in vivo, with results demonstrating significant osteoblast and chondrocyte adhesion [165-169]. These works are a critical development as osteoblast adhesion is the first step for subsequent cellular responses including proliferation, formation of extracellular matrix protein and mineral deposits [168]. As biomaterial surface such as topography and chemistry controls the cellular and molecular events at the tissue-implant interface, simulating the normal bone surface using nanophase metal particle may enhance cellular responses and interactions, thus promoting osseointegration. In addition to increased cellular adhesion [165, 168], it has been also shown that the composite scaffolds with PLGA and metal nanoparticles stimulate increased long-term osteoblast functions including collagen synthesis, alkaline phosphatase (ALP) activity, and calcium deposition [166, 167, 169]. Enhanced osteoblast adhesion is more dependent on the optimal surface topography of nanophase composite rather than specific material type [168].

Similarly, nanometer surface roughness may be the key factors stimulating osteoblast adhesion and its long-term functions for bone regeneration [166].

Nanoparticle Class	Nanoparticle Material	Function and Biological Improvements	Reference
Bioceramics	HA and PEG/PBT	Increased Young's modulus, tensile strength, and elongation at break of composite scaffold	[155]
	HA/PLLA	Increased compressive modulus and protein adsorption	[156]
	HA/PLGA	Stimulated cell proliferation and osteogenic differentiation	[157]
		In vivo bone formation after 8 week of implantation to critical size defects in rat skulls	[158]
Metals	Titania	Superior compressive strength and osteoconductivity of PMMA composite	[164]
		Enhanced cellular adhesion	[165, 168]
		Increased osteogenic functions in PLGA composite scaffolds	[166, 167, 169]
	Alumoxane	Increased flexural and compressive strength of PPF composite scaffold	[163]
Others	SWNT/PPF	Significantly improved flexural and compressive modulus, compressive offset yield strength, flexural strength	[159]
	Silica/PCL	Similar mechanical properties of natural bone	[160]
	Nano-silica fused whisker	Increased strength and toughness of whisker surface	[162]

Table 6: Nanoparticle/Polymer Composite Scaffolds

Overall, using various nanoparticles as fillers into scaffold material generally creates a superior nanocomposite material with enhanced mechanical properties and facilitated cellular function (See Table 6). Present investigations with nanoparticle/polymer composite scaffold demonstrate that such engineered composite scaffold could be considered for bone tissue engineering applications. However, it is not clear that any one approach is significantly superior to another for scaffold fabrication. Therefore, more development and investigations on the surface chemistry of materials as well as specific interactions between cell/material and material/polymeric scaffold may be required.

3.3. Nanofibrous Scaffolds

Nanofibrous scaffolds are another approach for engineering scaffolds with nanotechnology. In addition to the suitable mechanical strength for load-bearing applications, scaffolds for bone tissue engineering may have an artificial extracellular matrix (ECM) with morphologies that replicate the natural ECM, composed mainly of collagen and proteoglycans. Therefore, nanofibrous scaffold may provide a more favorable environment for cellular ingrowth and subsequent bone regeneration as they have architectural, functional, and morphological similarities to collagen fibrils, especially due to nanometer-order diameter, high porosity and high surface-to-volume ratio [170]. For example, as collagen is a natural ECM molecule in many tissues and plays an important role as a substrate for cell attachment, proliferation, and differentiation, a biomimetic nanofibrous scaffold may be developed with similar properties to induce favorable cellular responses. Nanofibrous scaffolds have been

developed using various synthetic polymers including PLLA [111, 171-173], PCL [174-178], PLGA [179, 180], copolymer [181], and chitosan [181].

Three-dimensional PLLA nanofibrous scaffolds have been shown to improve protein adsorption, mediating cellular interactions within the scaffold. In particular, these PLLA nanofibrous scaffolds allowed for increased fibronectin and vitronectin adsorption from the surrounding media, promoting osteoblast attachment to increase more than 1.7 times when compared to control scaffolds [172]. As cell attachment is the very initial step to promote long-term cellular functions such as migration, proliferation, and differentiation, enhanced protein adsorption and cellular adhesion imply that nanofibrous scaffold may provide more biocompatible microenvironment for cell-matrix interaction.

Subsequently, it has been verified that osteoblast cultured on PLLA nanofibrous scaffolds exhibited significantly increased proliferation, mineralization throughout osteogenic differentiation, and bone marker protein expression [173] when compared to unmodified PLLA. Specifically, osteoblastic cells cultured on PLLA nano-fibrous scaffolds showed higher ALP activity, increased runx2 protein expression, increased bone sialoprotein mRNA, and increased mineralization versus solid-walled control scaffolds. Moreover, nanofibrous scaffolds are thought to be comparable to natural collagen fibers. Here, cells seeded on nanofibrous scaffolds sustained alpha2 integrin expression in the presence of dehydroproline, while suppression of the same marker protein was evident in cells seeded on solid-walled scaffolds. Similar results have been found in a series of PCL studies [178]. Under dynamic culture conditions, mesenchymal stem cells derived from neonatal rat bone

marrow were cultured on PCL nanofibrous scaffolds. After 1 week, significant cell migration and enhanced formation ECM were detected in the scaffold. Cell multilayers formation, mineral deposition, and type I collagen expression were also observed after 4 weeks. Similarly, in an in vivo study [176], it was confirmed that cell-PCL constructs gave rise to a bone-like appearance with sufficient cell/ECM formation on the surface of the scaffold construct, mineralization, and type I collagen expression.

Interestingly, it was also shown that the presence of nanofibers had an influence in cell shape and morphology, including increased cell spreading [177]. Cell culture studies with a SaOs-2 human osteoblast-like cell line and rat bone marrow stromal cells demonstrated stretched cell morphology, cytoskeletal rearrangement, and quicker scaffold colonization. Human mesenchymal stem cell (hMSC) studies in a nanofibrous scaffold have described the potential use of nanofibrous scaffold in injured bone healing. PCL nanofibrous scaffolds demonstrated the ability to support and maintain multilineage differentiation of bone marrow-derived hMSCs in vitro. For example, hMSCs seeded onto PCL nanofibrous scaffold differentiated into adipogenic, chondrogenic, and osteogenic lineages [174]. hMSCs cultured in PLGA nanofiber scaffolds (approximately 700nm in diameter) also demonstrated cell viability and proliferation as well as the promotion of multiple cell lineages [180]. Chitosan-based nanofibers, with an average diameter below 40 nm, exhibited directional alignment and a potential for bone regeneration graft [101]. Finally, nanofibrous materials consisting of a chitosan and poly(ethylene oxide)

(PEO) blend promoted the attachment of human osteoblasts and chondrocytes, as well as maintained cell viability.

Taken together, nanofibrous scaffolds with high surface-to-volume ratio may possess a great advantage by providing a more favorable environment for bone tissue formation such as enhanced cell attachment and proliferation (See Table 7). In addition to three dimensional configuration and similar nanometer order morphology to natural ECM, the relatively large porosity and pore size found in nanofibrous scaffolds may enable sufficient cell propagation and differentiation. These architectural characteristics may also enable to proper transport of cellular substances including signaling molecules, nutrients, and metabolic wastes [170]. As a result, nanofiber scaffolds may be a promising bone tissue engineering scaffold based on their ability to facilitate various cellular functions including adhesion, proliferation, and differentiation.

Nanofiber Material	Function and Biological Improvements	Reference
PLLA	Improved protein adsorption and osteoblastic cell attachment	[172]
	Increased proliferation, mineralization, bone marker protein expression	[156]
PCL	Enhanced penetration of MSCs into the scaffold and increased formation of ECM in vitro	[178]
	Sufficient cell/ECM formation on the surface of scaffold in vivo	[176]
	Supports in vitro multilinage of hMSCs	[174]
PLGA	Supports in vitro multilinage of hMSCs	[180]

Table 7: Nanofibrous Scaffolds

3.4. Nanotechnology for Growth Factor Delivery

Growth factors are one of the essential factors that induce or stimulate intracellular functions including cell recruitment to the healing site, mitogenesis, differentiation into the osteogenic linage, and renewal for bone formation [15, 182]. Considering some of the disadvantages of conventional scaffold implantation for bone tissue regeneration (inflammation, low growth factor expression, and low cell proliferation), a growth factor delivery system or the growth factor gene delivery system has become a probable and promising solution for improved bone regeneration. Among the various growth factors involved in bone tissue engineering, those of particular interest include, bone morphogenetic protein (BMP), transforming growth factor beta, platelet derived growth factor, and vascular endothelial growth factor (VEGF). These growth factors and the effect on bone formation has been well described [15, 183-186].

Osteoblast growth and subsequent bone formation strongly depends on the growth factor signaling. The combination of various growth factors and their sequential functions directs osteogenic differentiation as well as other downstream cellular functions. Nevertheless, direct injection of growth factor in solution is often not effective strategy due to rapid diffusion and excretion from the defect site [187]. Furthermore, unstable biological activity of the growth factors, short half-life, and minimal tissue penetration could result in inefficient delivery [183]. To reduce growth factor delivery failures associated with direct injection, the utilization of various carrier materials has been attempted. Compared to direct adsorption of a growth factor on the surface of an implanted scaffold, a carrier delivery system provides

controlled, long-term release with adequate efficacy [184]. Delivery carriers, themselves either implanted or injected, require materials that are biocompatible, biodegradable, as well as suitable for protein encapsulation. As many synthetic polymers possess these attributes, micron sized polymeric sphere have been widely used for encapsulation of growth factors. In particular, an encapsulated growth factor may be released as the polymer degrades following a controlled and predetermined profile. In addition to synthetic polymers [188-190], there are also other possible carrier materials including inorganic materials (hydroxyapatite, tricalcium phosphate, carbonate apatite, silica) and natural polymers (collagen, hyaluronic acid, chitosan, alginate). A series of reviews have already covered various types of growth factor delivery materials [183, 185, 191-194]. Here, we consider nanoparticle technology for the delivery of genes encoding growth factors (See Table 8).

3.4.1. Nano-Scaled Gene Delivery Systems

Growth factor gene delivery can be more effective than the delivery of growth factors due to the sustained production and secretion of growth factors achieved by gene transfection. Transport of exogenous DNA is a sequential process (Mansouri et al., 2004); (a) internalization of DNA-nanoparticle complex through the cell membrane, (b) uptake by intracellular endosome, (c) release into the cytoplasm, (d) uptake of the complex in the nucleus, (e) dissociation from the nanoparticle vector, (f) protein expression, and (g) secretion of the growth factor protein. Over these steps, the carrier vector should be small enough to be internalized into the cell over several barriers, and capable of escaping endosome-lysosome processing in order to protect

DNA until it reaches the target cell [195]. Considering their size and physical properties, nanoparticles can be an excellent carrier vector. Nanoparticles with sub-cellular size can penetrate into tissues and cells in the targeted sites, and easily deliver a therapeutic through endocytosis. In addition, nanoparticles are also able to cross the blood-brain barrier by opening tight junctions in the paracellular pathway and passage to the cellular nucleus. Finally, nanoparticles often allow more effective and efficient targeted delivery even in distant healing sites [196]. In contrast to viral vectors which are based on virus as a carrier system, non-viral vectors system using nanoparticles have several advantages like flexibility toward the molecular size of loaded DNA, nonimmunogenic route, the ability to target specific tissues, low toxicity, and no risk of recombination to an infectious virus [185, 186, 197]. Due to these reasons, non-viral vector must be preferable for clinical usages despite low transfection efficiency in vivo [197].

Nanoparticle System	Function and Biological Improvements	Reference
Polymeric Nanoparticle + DNA	Up to 70% high DNA encapsulation efficiency with sustained release both in vitro and in vivo	[198]
	Polymerized nanogel with stability in aqueous media, low toxicity, and enhanced DNA uptake in HeLa cell	[199]
	PLGA nanoparticle with tetracycline with affinity for HA	[200]
	Higher gene expression level with smaller size of PLGA	[201]
	Penetration of PLGA-VEGF nanoparticle carrier in myocardial cells and successful in vivo angiogenesis	[202]
PEGylation	Extended half-life of BSA with PEG-PLGA nanoparticle	[203]
	Effective gene release with AMPEG/PCL nanoparticle with low density of primary amine groups	[204]
	Higher DNA protection to enzymatic degradation and higher reporter gene expression with PEG-cationized gelatin	[205]
	Increased DNA penetration into the cells and luciferase activity with DNA-PEG-gelatin nanoparticle	[206]
Micelle	Adherence of aldehyde-terminated PEG-PLA block polymer to a tissue surface in vivo	[207]
	Efficient and less toxic transfection toward primary osteoblast cells using polyplex micelles	[208]
Liposome	Enhanced bone formation in cranial defect on rabbit model using cationic liposome loading BMP-2 cDNA plasmids	[209]
	Critical size defect healing in rat model, less efficient BMP-2 gene transfer of liposome than adenoviral carriers	[210]
	More effective bone formation in a rat bone-defect model using magnetic rhBMP-2 liposomes	[211]
Dendrimer	Targeted delivery of anti-arthritic drug with folate-PAMAM dendrimer	[212]
	LacZ gene transduction in human chondrocyte-like cell without cytotoxic effect and morphological changes	[213]
	Increased nucleus penetration and enhanced gene transfection using dexamethasone conjugated PAMAM	[214]
Nanosized Inorganic Material	In vitro DNA transfection using DNA-chitosan nanoparticle	[215]
	Enhanced DNA internalization of DNA mediated byfolate receptor binding, improved gene transfection rate subsequently	[216]
	Co-precipitated DNA with calcium phosphate nanocomposites onto the cell-culture surface enhanced β-gal expression level in MG-63 and Saos-2 cells	[217]

Table 8: Nanoparticle Gene Delivery Systems

3.4.2. Polymeric Nanoparticles

Owing to the biodegradability of many synthetic polymers, nanosized polymeric particles are often some of the best candidates for non-viral gene delivery in tissue engineering applications. PLGA nanoparticles have been shown to offer protection of genes to nuclease degradation, increased DNA uptake, and sustained duration of DNA administration, as well as subsequent gene transfection and expression. In addition to the sustained release of encapsulated pDNA, biologically compatible degraded material such as lactic acid and glycolic acid may be another advantage of polymeric nanoparticle delivery. For example, PLGA containing human placental ALP plasmid DNA (pDNA) exhibited high encapsulation efficiency of 70% and sustained release of pDNA [198]. In vitro transfection using human endothelial cell lines demonstrated both higher gene expression level than naked pDNA and a sustained gene release (higher at 1 wk than 48 hr after transfection). Similarly, In vivo transfection utilizing a rat tibial muscle indicated that this nanoparticle gene delivery showed 28 d of sustained gene transfection although ALP expression level after 3 and 7 d of a single intramuscular injection of naked pDNA injection is higher than that of pDNA-PLGA nanoparticle injection. Polymerized hydrophilic nanogels composed of 2-acryloxyethyl trimethylammonium chloride, a nonionic crosslinker poly(ethylene glycol) diacrylate, and a nonionic monomer 2-hydroxyethlynacrylate were also fabricated into 40-200nm nanoparticles [199]. This monodispersed nanogel demonstrated stability in aqueous media, low toxicity and enhanced DNA uptake in HeLa cell culture. Surface-functionalized PLGA nanoparticles have also been reported for bone-specific drug delivery [200]. The conjugation of PLGA with

tetracycline showed a great affinity with HA, a significant inorganic component of hard tissues such as bone and teeth. Tetracycline has a strong affinity for adsorption to calcium phosphate and serves as a targeting moiety for bone-specific drug delivery. This resulted confirmed that the PLGA complex can be utilized as the carrier and guided material for bone regeneration strategy.

Particle size can vary the efficiency of nanoparticle-mediated gene transfection. Smaller-sized PLGA nanoparticle (70nm in diameter) containing pDNA encoding luciferase marker protein produced 27-fold higher transfection in COS-7 cell line and a 4 fold higher transfection in HEK-293 cell line than larger-sized particles (202nm in diameter) [201]. This work indicated that smaller particle size and uniform size distribution are critical factors for higher gene transfection efficiency.

In other tissue applications necessary for bone regeneration, such as blood vessel growth, polymeric nanoparticle has been utilized for gene delivery. For example, the stability, in vitro release, in vitro cell transfection efficiency, and in vivo gene transfer of VEGF-DNA loaded PLGA nanoparticles were investigated [202]. The diameter of VEGF pDNA-PLGA nanoparticle ranged 100-300nm in diameter and these gene carriers successfully penetrated in myocardial cytoplasm and nucleus. Furthermore, in vivo angiogenesis was identified by increased capillaries.

3.4.3. PEGylation

Critical parameters for gene delivery to target cells includes prolonged circulation time, stability within blood circulation, access to target tissue/cells, easy elimination from body, minimal toxicity, and minimal immunogenicity are required

[218]. Surface coverage by amphiphilic polymeric surfactant like PEG over nanoparticles increases the blood circulation time by preventing recognition of reticuloendothelial system located in the liver and lung [218, 219]. PEG has a flexible, hydrophilic polymer chain that effectively creates a 'water shell' to help to mask the bound proteins [219] and provide steric protection to the entrapped DNA from DNase degradation. PEG has also been introduced to address low DNA encapsulation efficiency of polymeric nanoparticle by mediating the weakly bound hydrophilic DNA and hydrophobic polymeric nanoparticle.

To this end, PEG-PLGA nanoparticles have shown that PEG enhances protein delivery [203]. Here, PEG-PLGA particles extended the half-life of bovine serum albumin (BSA) from 13.6 min of loaded in PLGA nanoparticles to 4.5 h and, as a result, dramatically altered the protein biodistribution in rats. Similarly, methoxy poly(ethylene glycol) (MPEG)/ PCL diblock copolymers have been investigated for the effect of charge group on transfection efficiency [204]. This work confirmed that amine-terminated MPEG (AMPEG)/PCL nanoparticles with cationic charge groups exhibited somewhat higher DNA transfection efficiency in comparison with the nonionic MPEG/PCL nanoparticles. The terminal amine group may also allow more effective DNA condensation due to the electrostatic interaction, and therefore result smaller gene-loaded particle size. PEG-cationized gelatin has also been used as non-viral gene delivery carrier. Gelatin was cationized by the introduction of amine residues to its carboxyl group. In particular, PEG was modified with one terminal of an active ester group coupled to the amino groups of cationized gelatin, resulting in PEG-cationized gelatin [205]. This PEGylation step guaranteed a higher level of

DNA protection to enzymatic degradation compared to the cationized gelatin and, as a result, higher luciferase reporter gene expression compared with the injection of pDNA solution. DNA-gelatin nanoparticles, whose molecular size was approximately 150 nm, were made by self-assembly due to electrostatic interaction between positively charged gelatin-derivatives and negatively charged DNA [206]. As it is difficult for negatively charged pDNA to internalize into cells due to repulsion, positively charged gelatin-DNA complex aids plasmid DNA to adhere onto the cell membrane and internalize into cells. As a result, this ionic interaction enhances the penetration of pDNA into the cell and the transfection efficiency. The amount of DNA penetrated into the cells was increased by the DNA-gelatin complexation, and luciferase activity was also significantly increased in the cell incubated with the DNA-gelatin nanoparticles than naked pDNA. Therefore, PEGylation could be used with other nanoparticle delivery system to enhance more growth factor secretion in defect sites due to two major advantages; higher pDNA transfection efficiency and pDNA protection from DNase degradation.

3.4.4. Micelles

Micelles are 50 - 100 nm sized spherical self-assemblies of block copolymers with a hydrophobic core and surrounding hydrophilic outer shell [220]. When fabricated with poly(ethylene glycol), the PEG outer shell often provides biocompatibility and longer blood circulation time, while the inner hydrophobic core allows encapsulation of a hydrophobic drug, DNA, or protein either physically or through covalent linkages. Through hydrophobic and electrostatic interactions

between the charged block copolymer and oppositely charged molecule, core-shell nanosized micelles have formed [221]. Polymeric micelles have several advantages as drug and gene carriers because of easy loading of drugs without chemical surface modification, wide availability to various therapeutics, simple fabrication methods, high loading capacity, and controlled release pattern [222]. A polymeric micelle consisting of an aldehyde-terminated poly(ethylene glycol)-poly(D,L-lactide) (PEG-PLA) block copolymer was shown to adhere to tissue surfaces in vivo, and therefore may be applied as tissue-adhesive material [207]. A PEG/PLA hydrogel could be also used for bone tissue engineering applications as the copolymer introduces favorable characteristics to the hydrogel carrier including PEG core hydrophilicity and biodegradable PLA linkages. Polyplex micelles, consisting of pDNA and cationic polymer complexes, have also been utilized in gene transfection in primary osteoblasts [208]. Results showed that the block catiomers carrying the ethylenediamine unit at the side chain are capable of efficient and less toxic transfection of primary cells.

Although many gene delivery researches using micelles have not been done in bone tissue engineering filed, DNA-micelle construct could be applied as potential gene delivery strategy. As there are several advantages of polymeric micelles such as excellent ability to carry poorly soluble pharmaceutical molecules and very hydrophobic compounds, possible targeting by attaching specific ligand molecules, and tumor-infiltrating ability, micelles could also be a candidate for growth factor gene delivery system. The further development of micelle with specific tissue-targeting may be required for elevating its clinical usage.

3.4.5. Liposomes

Liposomes are spherical vesicles encircled with a phospholipid bilayer membrane. Drug molecules or genes can be either entrapped in the aqueous space of the liposome or intercalated into the lipid bilayer [220]. Liposomes have been investigated as gene delivery device because of their ability to pass through lipid bilayers, including cell membranes, and amenability towards surface modification with targeting ligands or polymer [223]. Enclosed aqueous core can be utilized to carry hydrophilic agents, while multilamellar liposomes provide cargo space for lipophilic actives as well [224]. There are also some limitation of liposome based delivery; cellular and systemic impeding factors [225]. For cellular impeding factors, poor endosomal release of pDNA into the cell cytosol after internalization through the cell membrane is the major disadvantage of liposomal gene delivery. After releasing from the endosome, it might also be possible that the dissociation of polymer/pDNA complex is hard due to tight complex formation initially, that subsequent degradation of pDNA by cytosolic nucleases occurs, and that nuclear uptake efficiency of pDNA is very low. The instability of the injected liposome-gene complex in biological fluids containg serum proteins and high salt concentration may results in the systemic impeding factor. This is why lipofection is generally considered to be less potent in vivo than in vitro. For example, ALP expression after 7 d of injection resulting from pDNA-liposome complex in rat tibial muscle was found to be lower than that observed in naked pDNA and pDNA-PLGA nanoparticle injection [198].

Nevertheless, promising in vivo researches have also been performed recently in terms of bone tissue regeneration. Cationic liposomes loaded with BMP-2 cDNA

plasmids showed great effect on bone formation within cranial defects of a rabbit model [209]. In this study, BMP-2 gene and liposome were sprayed with 1:4 wt ratio on the defect area. Histopathological examination and X-ray image analysis data exhibited that BMP-2 gene with liposome apparently promoted the progress of osteogenesis and the bone defect area was almost filled with new bone by six week. Ex vivo cell-mediated BMP-2 gene transfer has also proven that liposome vector can be an attractive option for bone regeneration [210]. Rat bone marrow stromal cells pre-treated with either an adenovirus or a liposome carrying human BMP-2 cDNA were transplanted into critical size defects in the rat mandible. Although adenoviral vector showed more efficient gene transfer, the critical size defects treated with liposome-gene complex were found completely healed at 6 weeks after the gene transfer. Furthermore, liposome may be further modified for bone tissue engineering applications with the assistance of magnetic particle targeting system. Nanosized magnetic liposomes with incorporated recombinant human BMP-2 (rhBMP-2) have been investigated in a rat bone-defect model [211]. Treatment with rhBMP-2 liposomes under magnetic force showed nearly complete bone bridge formation. The greater efficacy of magnetic liposomes over conventional liposomes is due to the increased retention of BMP at the target site by magnetic induction. It is noteworthy that the combined treatment of topical magnetic rhBMP-2 liposomes and magnet implantation at the injured site was effective for bone defects treatment.

3.4.6. Dendrimers

Dendrimers are synthetic polymers with highly branching structures. By a

series of polymerization reactions, dendrimers grow from a central core molecule in outward direction [220]. This growing pattern results in a highly branched dendritic architecture, which is similar to the structure of glycogen, amylopectin, and proteoglycans. As a result of this structure, dendrimers may offer unique interfacial and functional advantages. [224] As a nanoscale container, cavities in the core structure and folded branches of the interior shell create cages and channels which are protected from outside environments. Furthermore, a muitivalent surface containing a number of active sites can be functionalized for the attachment of targeting groups [224]. As a dendrimer's size, shape, branching length, branching density, and surface functionality may be easily controlled, these molecules may provide another avenue for nanoscaled delivery of proteins and genes to tissue defects, including osteochondral sites. For example, folate-polyamidoamine (PAMAM) dendrimer conjugates have been utilized as targeted delivery vehicles for the anti-arthritic drug indomethacin [212]. Folic acid was coupled to the surface amino groups of the dendrimer, with the resulting drug content and encapsulation efficiency increasing with increased folate content. Gene delivery with PAMAM dendrimer was also demonstrated in chondrocytes [213]. A pDNA containing LacZ gene was utilized to transduce a human chondrocyte-like cell line, HCS-2/8. As LacZ encodes β-galactosidase (β-gal), transfected gene expression level was evaluated both by β-gal activity assay and by X-gal staining. The results showed that optimal DNA to dendrimer complex ratio for enhanced β-gal activity was 2 μg of the plasmid vector containing LacZ gene combined with 21 μg of dendrimer. At this ratio, the highest proportion of X-gal staining was observed and β-gal activity peaked 3days after the

dendrimer-mediated transduction without any cytotoxic effect. This research demonstrated the potential use of nano-scaled dendrimers as gene delivery vehicles to chondrocytes. Finally, PAMAM-glucocorticoid conjugation has been attempted in order to increase nuclear membrane penetration and enhance subsequent gene transfection efficiency [214]. To this end, dexamethasone, a potent glucocorticoid, was conjugated to PAMAM dendrimer. The resulting complex exhibited higher gene transfection efficiency, when compared to PAMAM or polyethyleneimine alone, as the glucocorticoid receptor dilated the nuclear pore and translocated into nucleus after ligand binding, demonstrating the utility of a dexamethasone conjugated dendrimer/DNA complex for non-viral gene delivery.

3.4.7. Inorganic Nanoparticles

Chitosan, a natural polymer derived from chitin, has also been used as a gene carrier as its cationic polyelectrolyte property allows a strong electrostatic interaction with negatively charged DNA. Chitosan has been shown to condense DNA and form nano-size discrete particles for gene delivery [215]. Stable DNA-chitosan particles, which are typically 50-100nm in diameter, were fabricated and successively transfected HeLa cells. In addition, transfection was resistant to 10% fetal calf serum condition, suggesting applicability as an in vivo gene delivery system. However, results have shown that the efficiency of chitosan-DNA nanoparticle mediated transfection may be cell type dependent. For example, transfection efficiency was tested with human MSCs, human osteosarcoma cells (MG63), and human embryonic kidney cells (HEK293) [226]. Although mesenchymal stem cells showed less

transfection efficiency than embryonic kidney cell, chitosan mediated gene delivery still demonstrated homogeneous DNA distribution and cytocompatibility. In order to increase transfection efficiency, folic acid again has been used as a ligand for targeting cell membranes, with results indicating nanoparticle endocytosis via the folate receptor [216]. As cellular folic acid uptake may be utilized to promote targeting and internalization, a folic acid-chitosan nanoparticle can be used in gene therapy in diseases where folic acid receptors are overexpressed.

Other inorganic materials such as calcium phosphate have also been developed as nano-scale delivery devices. Nanocomposites based on calcium phosphate co-precipitated with DNA have been evaluated as gene delivery systems [217]. While some gene delivery systems contain drawbacks including inefficiency and toxicity when maintaining a high DNA concentration near the cell surface, the resulting DNA nanocomposites provided regions of high DNA concentration in the immediate microenvironment of the cultured cells and enhanced gene transfer. Enhanced gene transfer was measured via β-galactosidase expression level in both the osteoblastic MG-63 cell line and the Saos-2 human bone tumor cell-line, with resulting indicating that transfection was as efficient as a commercial, lipid-based transfection reagent.

3.5. Summary

Nanoparticle technology has been increasingly applied to biological research due to advantageous characteristics of nanoparticles including extremely small size, surface functionality, and comparability with cellular components. For bone tissue

engineering, nanoparticle technology may be the one of the best supporting strategies to solve existing limitations of conventional tissue engineering approaches. For example, the mechanical strength of scaffold materials may be improved by fabrication of nanoparticle/polymer composite scaffold. Nanofibrous scaffold may provide more favorable microenvironment for cell growth in healing sites, as they often resemble extracellular matrix components. Finally, nanoparticles are also able to act as a carrier device for gene delivery. With the assistance of nanoparticle non-viral delivery system, more effective and efficient delivery of growth factor genes may be achieved and, as a result, enhanced bone regeneration realized.

Each nanotechnology discussed in this review could provide significantly different improvement for bone regeneration including enhanced rigidity of bone substitute, biomimic architecture of implanted sites, and improved osteoinductive growth factor production. Future studies will consider the incorporation of each individual strategy to set up the integrated clinical platform. Furthermore, in vivo studies to verify effective gene delivery using each nanoparticle system, following growth factor secretion, and improved osteogenesis are essentially required to assure its clinical application. Nanoparticle technology conjugated with tissue engineering strategies promises new avenues for bone regeneration.

Chapter 4: The Effect of Initial Cell Seeding Density on Early Osteogenic Signal Expression of Rat Bone Marrow Stromal Cells Cultured on Crosslinked Poly(propylene fumarate) Disks

4.1. Introduction

Functional engineering of natural bone tissues involves three fundamental components: (1) parenchymal or progenitor cells which enable lineage-specific differentiation and subsequently express tissue matrix, (2) scaffolds as temporary frameworks to support bone growth, and (3) osteogenic signals such as growth factors to induce bone-forming cell regeneration. The successful conjugation of these principal components is the most critical and challenging problem to develop functional bone replacements.

As a cell source in the tissue engineering field, bone marrow stromal cells (BMSCs) have been extensively investigated since this heterogeneous cell source contains mesenchymal stem cells. These progenitor cells have distinctive characteristics that allow them to be (1) expanded cell numbers by replication *in vitro* and (2) differentiated into a variety of cell types such as osteoblasts, chondrocytes, and adipocytes [174, 227-229]. Since these differentiated cell types can be developed into various tissues and organs, including bone, cartilage, adipose, tendon and ligament, BMSCs are considered as an excellent source for autologous cell therapy

As published in **K. Kim**, D. Dean, A. Mikos, and J.P. Fisher, "Effect of Initial Cell Seeding Density on Early Osteogenic Signal Expression of Rat Bone Marrow Stromal Cells Cultured on Cross-Linked Poly(propylene fumarate) Disks", Biomacromolecules, 10:1810-1817 (2009).

and regenerative strategy in tissue engineering research [15, 230, 231]. Therefore, BMSC-seeded polymeric scaffolds have been widely utilized to create successful *in vitro* models for bone tissue repair.

As a potential scaffold material, poly(propylene fumarate) (PPF) is known to be injectable, *in situ* polymerizable, and a biocompatible linear polyester [232]. This polymer contains carbon-carbon double bonds that allow constructs of cross-linked networks, and ester linkages that allow for hydrolytic degradation [233]. PPF degradation products, including propylene glycol, poly(acrylic acid-co-fumaric acid), and fumaric acid, do not shift pH to a level that is hazardous to natural tissues, and can be metabolized as a constituent of the Krebs cycle [233]. PPF can be crosslinked by ultraviolet (UV) radiation with the aid of a photoinitiator such as bis(2,4,6-trimethylbenzoyl) phenylphosphine oxide [234]. PPF also possesses sufficient mechanical strength for use as a bone substitute at load bearing sites [235]. A series of studies have revealed that PPF is a promising biomaterial for bone tissue engineering. It has been used for fabrication of composite materials [77, 163, 236-238], rapid prototyping using laser-stereolithography to create controllable microarchitecture for patient-specific bone implants [102, 239, 240], and growth factor delivery vehicles [241, 242].

Lineage-specific differentiation of BMSCs on polymeric scaffolds is correlated with the activation of inductive signaling molecules such as various cytokines, hormones, and growth factors. In order to establish the optimal fabrication parameters necessary for successful bone tissue engineering scaffolds, we propose that it is critical to understand the intercellular signaling mechanisms among the

transplanted cell population. Our overall hypothesis is that the proper microenvironment could facilitate osteogenic signals among a transplanted cell population, and paracrine cell-to-cell distance is one of the critical parameter which is determined by initial cell seeding density.

The artificial microenvironment of a cell population seeded on a synthesized polymeric material may facilitate osteogenic signals. A strong understanding of these signaling profiles may be critical to the successful development of a functional cell/scaffold construct. There have been several recent studies to investigate the effect of cell seeding density on cellular activities. Rat bone marrow stromal cells (BMSCs) on three dimensional (3D) poly(DL-lactic-co-glycolic acid) scaffolds showed rapid proliferation at a lower seeding density over the first 7 days, but no changes in osteoblastic functions such as alkaline phosphatase (ALP) activity and mineralization after 56 days in culture [243]. However, increasing the seeding density of rat BMSCs in titanium fiber mesh had a positive effect on osteogenic expression [244] and a higher seeding density on polystyrene well plate led to higher ALP activity and more mineralization [245]. In addition, an optimal seeding density was determined to best promote intracellular signals, such as Runx2, in MG-63 cells cultured within dense 3D collagen gels [246]. Similarly, a recent study also demonstrated the existence of the minimum and optimum cell seeding density in 3D hydroxyapatite/tricalcium phosphate (TCP) scaffolds for bone yield (i.e., bone contact and bone area) in a goat *in vivo* model [247]. However, another study reporting a contrary result, found that a lower seeding density of human alveolar osteoblasts on 3D polycaprolactone/TCP was associated with higher ALP activity and osteocalcin

(OC) secretion [248]. Despite of the fact that there have been many studies about the effect of adding growth factors (i.e., exogenous signals) on the osteogenic differentiation of BMSCs [6, 249-251], changes in endogenous gene expression of signaling growth factors caused by altering the intercellular paracrine communication distance have not been extensively studied. Therefore, the objectives of the present study were to determine the effect of initial seeding density of rat BMSCs onto two dimensional (2D) PPF disks on cell viability, proliferation, and differentiation, as well as to describe the effect of cell seeding density on osteogenic signal expression profiles. Most critically, this study demonstrates for the first time that the expression profiles of endogenous osteogenic growth factors can be controlled by the initial cell seeding density on PPF disks.

4.2. Experimental Section

4.2.1. Materials

Diethyl fumarate, propylene glycol, zinc chloride, hydroquinone, ascorbic acid, β-mercaptoethanol, and Alizarin Red S were obtained from Sigma-Aldrich (St. Louis, MO). Analytical reagent grade methylene chloride was purchased from Fisher Scientific (Pittsburgh, PA). Polystyrene standards were received from Polymer Laboratories (Amherst, MA). Bis(2,4,6-trimethylbenzoyl) phenylphosphine oxide (BAPO) was obtained from Ciba Specialty Chemicals (Tarrytown, NY). Alpha-minimum essential medium (α-MEM), penicillin/streptomycin antibiotics, fetal bovine serum (FBS), and trypsin/EDTA were purchased from Invitrogen (Carlsbad, CA). PicoGreen assay kit was obtained from Molecular Probes. Collagenase-P was

purchased from Roche (Indianapolis, IN). RNeasy Mini plus kit was received from Qiagen (Valencia, CA). High Capacity cDNA Archive kit, Universal PCR Master mix (2x), and Taqman® Gene Expression Assay for growth factors and osteogenic differentiation marker were purchased from Applied Biosystems (Foster City, CA).

4.2.2. PPF Synthesis and PPF Disk Fabrication

PPF was synthesized with diethyl fumarate and propylene glycol following a two step procedure [232, 234]. Briefly, 1 mol of diethyl fumarate and 3 mol of propylene glycol were reacted with 0.01 mol of zinc chloride as a catalyst and 0.002 mol of hydroquinone as a crosslinking inhibitor with nitrogen gas purge, heat supply, and mechanical stirring. The resulting diester intermediate, bis(2-hydroxypropyl) fumarate, underwent transesterification with vacuum, heat supply, and mechanical stirring until the desired molecular weight was obtained. The final PPF polymer was dissolved in methylene chloride for further purification. The PPF/solvent mixture was purified during serial washing steps with 5 v/v% HCl solution, water, and brine. Residual methylene chloride was evaporated using a rotor-evaporator and vacuum pump. Then, hydroquinone was removed by ethyl-ether precipitation on ice, and excess ethyl ether was completely evaporated again using a rotor-evaporator and vacuum pump. Gel permeation chromatography (GPC) was used to measure the molecular weight and polydispersity index (PDI) of purified PPF. Polystyrene standards with a peak molecular weight of 580, 1180, 2360, and 4490 g mol^{-1} were used to create a calibration curve. The resulting number average molecular weight (Mn) was 2100 g mol^{-1} and PDI was 2.4. For the photocrosslinked disk fabrication,

the photoinitiator BAPO was employed (0.5 g BAPO/ g PPF) for photocrosslinked disk fabrication. A homogeneous 1.5 mm thick PPF/BAPO mixture was placed between the glass plates. After 2 hr of ultraviolet (UV) radiation exposure (intensity of 2.68 mW/cm^2), a crosslinked sheet of PPF was retrieved and cut into disks that were 18 mm in diameter and 1.5 mm thick.

4.2.3. Rat Bone Marrow Stromal Cell Isolation and Culture

Rat BMSCs were isolated from femora and tibiae of young male Wistar Hanover rats (101-125g, Taconic, Hudson, NY) following a University of Maryland approved IACUC animal protocol (R-07-94). Following euthanasia by carbon dioxide gas, the femora and tibiae were excised and all soft tissues were removed. The explanted bones were incubated in 10 ml of cell culture medium for 10 min three times. The culture medium contained α-MEM supplemented with 10 % (v/v) penicillin/streptomycin antibiotics, 10 % (v/v) FBS, 0.2 mM of ascorbic acid. Both ends of each bone were clipped off and bone marrow was flushed out with 10 ml of culture media using a syringe and 18-gauge needle under sterile conditions. The collected marrow was homogenized by mixing with a syringe, passed through a 70 μm cell strainer, and centrifuged at 500 g for 5 min. The resulting cell pellets were resuspended with 5 ml of culture media and plated in T-25 cell culture flasks. The media was first changed to remove non-adherent cells after 48 hrs, and changed every 2-3 days over the course of each subculture periods. When 80 % confluency of the cells was reached, cells were enzymatically lifted using trypsin/EDTA. The cells were passaged every 5-7 days until the proper cell number was obtained for further

cell seeding. All flasks were incubated under standard cell culture conditions (37°C and 5% CO_2 gas).

4.2.4. Cell Seeding

The PPF disks were prewashed before cell seeding in the following manner: All disks were soaked first in phosphate buffered saline (PBS) for 15 min to eliminate surface debris, second in acetone for 3 min to remove any unreacted monomers, and, third in PBS again for 30 min. After these washing steps, the samples were sterilized with UV radiation in a biosafety laminar flow hood overnight. Each disk was placed in a 12 well tissue culture polystyrene (TCPS) plate. Next, autoclaved stainless steel rings (outer diameter: 19 mm, inner diameter: 16 mm, height: 15mm) were placed onto each disk to confine the cell seeding area, to prevent the disk from floating, and to inhibit the loss of cells at the periphery between the disk and the well. Second passage rat BMSCs were trypsinized from culture flasks and the total cell number was counted using a hemacytometer to calculate the required volume of media for resuspension. After centrifugation, the cell pellet was resuspended with osteogenic media (control media supplemented with 10 mM Na-β-glycerophosphate and 10^{-8} M dexamethasone) to create a series of cell density (0.06, 0.15, 0.30 million cells/200 μl suspension). All of the experimental groups are listed in Table 9. Next, 200 μl of suspension was dropped onto the center of the PPF disks in the stainless steel ring, and 1800 μl of osteogenic media was added to the outer region between the ring and the well (Day 0). The same volume of cell suspension with 0.06 and 0.30 million cells was dropped into a TCPS well plate without a PPF disk as a positive control

sample. The cell/disk constructs were incubated for 24 hrs to allow complete cell-attachment. The steel rings were removed and the osteogenic media was changed every 2-3 days during the experimental time periods. All the assays except the cell viability test were performed at day 1, 4, and 8.

Groups	Description	Cell Density (cells/cm^2)
PPF Min	60,000 cells on PPF disk	30,000
PPF Med	150,000 cells on PPF disk	75,000
PPF Max	300,000 cells on PPF disk	149,000
TCPS Min	60,000 cells per well of tissue culture polystyrene 12 well plate	30,000
TCPS Max	300,000 cells per well of tissue culture polystyrene 12 well plate	149,000

Table 9: Experimental and Control Groups

4.2.5. Cell Viability

Cell viability was examined using a Live/Dead viability/cytotoxicity assay kit to evaluate the initial cell attachment to PPF disks and the viability at day 1 and 8. Osteogenic media was removed from the well and the cell/disk constructs were rinsed with PBS two times to remove unattached cells. Each construct was labeled with 700 μl of calcein AM (2 μM) and ethidium homodimer-1 (4 μM) fluorescent dye/PBS solution per well. After 30 min incubation at room temperature, images were taken to observe the cell attachment, localization, and viability over the culture periods under a fluorescence microscope (Axiovert 40 CFL with filter set 23, Zeiss, Göttingen, Germany) equipped with a digital camera (Diagnostic instruments 11.2 Color Mosaic, Sterling Heights, MI).

4.2.6. DNA Quantification

To assess cellular proliferation, DNA was isolated and the double-strand DNA amount was quantified using a PicoGreen assay kit. After removing the culture media from the well, the cell/disk constructs were washed with PBS two times. Cell layers on the disks were lifted with 600 µl of trypsin/EDTA, and 600 µl of collagenase-P was added to disrupt the extracellular collagen matrix. After transferring 1200 µl of cell suspension to a new sterile tube, each disk was rinsed with 600 µl of culture media and then transferred to the same tube. Calcein AM staining, and specifically the lack of any stain, was utilized to confirm that all cells had been removed from the disk. A 1,800 µl suspension was centrifuged down (1,000 g, 5 min) to form a cell pellet. After aspirating the supernatant, 1 ml of autoclaved distilled water was placed in each tube and the pellet was homogeneously resuspended. DNA was extracted from the suspension by 3 cycles of freeze (30 min at -80°C), thaw (30 min at 37°C), and sonication in a bath sonicator (30min). After cell-lysis, the cell debris was pelleted by centrifugation at 12,000 g for 10 min and 900 µl of supernatant was transferred to a new sterile tube. Next, 100 µl of supernatant containing DNA was mixed with 100 µl of diluted PicoGreen fluorescent dye in a 96 well plate. The samples in the well plate were incubated for 10 min at room temperature. Fluorescent intensity was recorded at 490 nm of excitation and 520 nm of emission using a M5 SpectraMax microplate reader (Molecular Devices, Sunnyvale, CA). The final double strand DNA amount was calculated based on an λ-DNA standard curve with known DNA concentrations.

4.2.7. RNA Extraction

Total RNA was isolated from each cell/disk construct with a RNeasy Mini plus kit following the protocol provided by the manufacturer. First, cells were lifted and collected in the same manner described above. Once the cell pellet was obtained, 350 µl of RLT lysis buffer with 3.5 µl of β-mercaptoethanol was added. Cells were homogenized by mixing within a 1 ml syringe using a 22 gauge needle. Genomic DNA was removed by passing the lysate through a genomic DNA elimination membrane column. After several washings in a spin column, total RNA was captured by a RNeasy mini-column membrane and eluted with 33 µl of Rnase-free water. RNA concentration and purity were assessed using Nanodrop UV/Vis spectrophotometry (Nanodrop Technologies, Wilmington, DE) with absorbance at 260 and 280 nm.

4.2.8. Quantitative Reverse Transcription Polymerase Chain Reaction (qRT-PCR)

Isolated total RNA was reverse transcribed to complementary DNA (cDNA) using the High Capacity cDNA Archive kit. The cDNA sample was subsequently mixed with Universal PCR Master mix (2x) and Taqman® Gene Expression Assays. Four target growth factor genes including bone morphogenic protein-2 (BMP-2, Taqman Assay ID: Rn00567818_m1), transforming growth factor-β1 (TGF-β1, Rn00572010_m1), platelet-derived growth factor-A (PDGF-A, Rn00709363_m1), and fibroblast growth factor-1 (FGF-1, Rn00563362_m1), as well as two osteogenic differentiation marker genes, including ALP (Rn00564931_m1) and osteocalcin

(OC), were assessed for relative gene expression level profiles. Pre-developed 18s ribosomal RNA was used as an endogenous control gene. The oligonucleotide primer and Taqman probe sequences for OC were 5' GGCTTCCAGGACGCCTACA 3' (forward primer), 5' GGGCAACACATGCCCTAAAC 3' (reverse primer), and 5' CGCATCTATGGCACCAC 3' (probe). Real time quantitative polymerase chain reaction (qRT-PCR) was performed on an ABI Prism 7000 sequence detector (Applied Biosystems). The thermal conditions for the PCR were 2 min at 50°C, 10 min at 95°C, and 50 cycles of 15 s at 95°C and 1 min at 60°C. The relative gene expression level of genes of interest (fold change) was first normalized to the mean of 18s control gene data in each group. The TCPS Min group was chosen as a calibrator and fold change was calculated by ΔΔCt method using the mean of the calibrator data. Mean of fold changes compared to the calibrator group (The TCPS Min group) and standard deviations are reported (n=3).

4.2.9. Mineralization Assay

Calcium mineralization was first qualitatively measured by Alizarin Red S staining and light microscopic images. Generally, Alizarin Red S stains calcium deposition orange-red and indicates mineralization of tissues or cells. At day 8, the cell layer on the PPF disk was washed with PBS two times and fixed with 4% paraformaldehyde for 10 min at 4 °C. The fixed cells were stained with 700 μl of 0.5 % Alizarin Red S/PBS solution (pH 4.2) for 10 min at room temperature, washed with PBS 5 times, and observed under an inverted light microscope to verify the presence of a red-colored calcium deposit. Images with x100 magnification were

taken from three different spots on each construct (i.e., one in the center and two at the corners, which were 5.66 mm away from the center along a diagonal axis) to quantitatively assess the images. A total of 9 images were obtained from each PPF group (six from the TCPS group). Each image (1.5×1.1 mm^2 dimension at a resolution of 1600 ×1200 pixels) was exported to the ImageJ program. After the subtraction of the background image, all images were converted to black and white binary images. The total black area was automatically calculated. The result was normalized with the DNA amount and presented as total mineralized area per DNA amount.

4.2.10. Statistical Analysis

In order to demonstrate the reproducibility of the data, all experimental groups were analyzed with biological triplicates, and all control groups were analyzed with biological duplicates. In addition, all measurements were collected in triplicate (technical triplicates). The data from all experiments were analyzed by one-way analysis of variance (ANOVA) and Tukey's multiple-comparison test was performed to verify the statistical difference between the experimental groups with 95% confidence ($p < 0.05$). The means and the standard deviations are reported in each figure.

4.3. Results

4.3.1. Attachment, Viability, and Differentiation of Rat BMSCs

The initial cell attachment, cell distribution, and viability of the rat BMSCs over 8 days were demonstrated by Live/Dead fluorescent staining (Figure 4). Compared to the TCPS positive control, rat BMSCs showed the same initial attachment pattern and distribution throughout the seeding area (Figure 4A). Cells were spread and exhibited cuboidal morphological changes (Figure 4B); few non-viable cells were found in any of the experimental groups at any time points. It was qualitatively demonstrated that as the culture period (i.e., 8 days) progressed, the cells proliferated to cover more surface area of the PPF disks, eventually initiating direct contact between adjacent cells. In addition, rat BMSCs were viable for 8 days in all density groups, implying that the PPF biomaterial provided a suitable 2D substrate.

As measured by DNA content, rat BMSCs proliferated on the surface of PPF disks over the 8 day period in all cell density groups (Figure 5). Except for the PPF Max group, all groups on days 4 and 8 contained a significantly higher DNA amount than at previous time points. The rate of proliferation in the PPF Min group was highest among the three different density groups, and this observation was in agreement with the qualitative fluorescent images in Figure 4. On the other hand, the PPF Max group displayed minimal proliferation during the first 4 days of culture. These results demonstrated that the lower cell seeding density stimulated more rapid proliferation and that PPF disks can support the rat BMSCs proliferation as a 2D monolayer substrate.

(A)

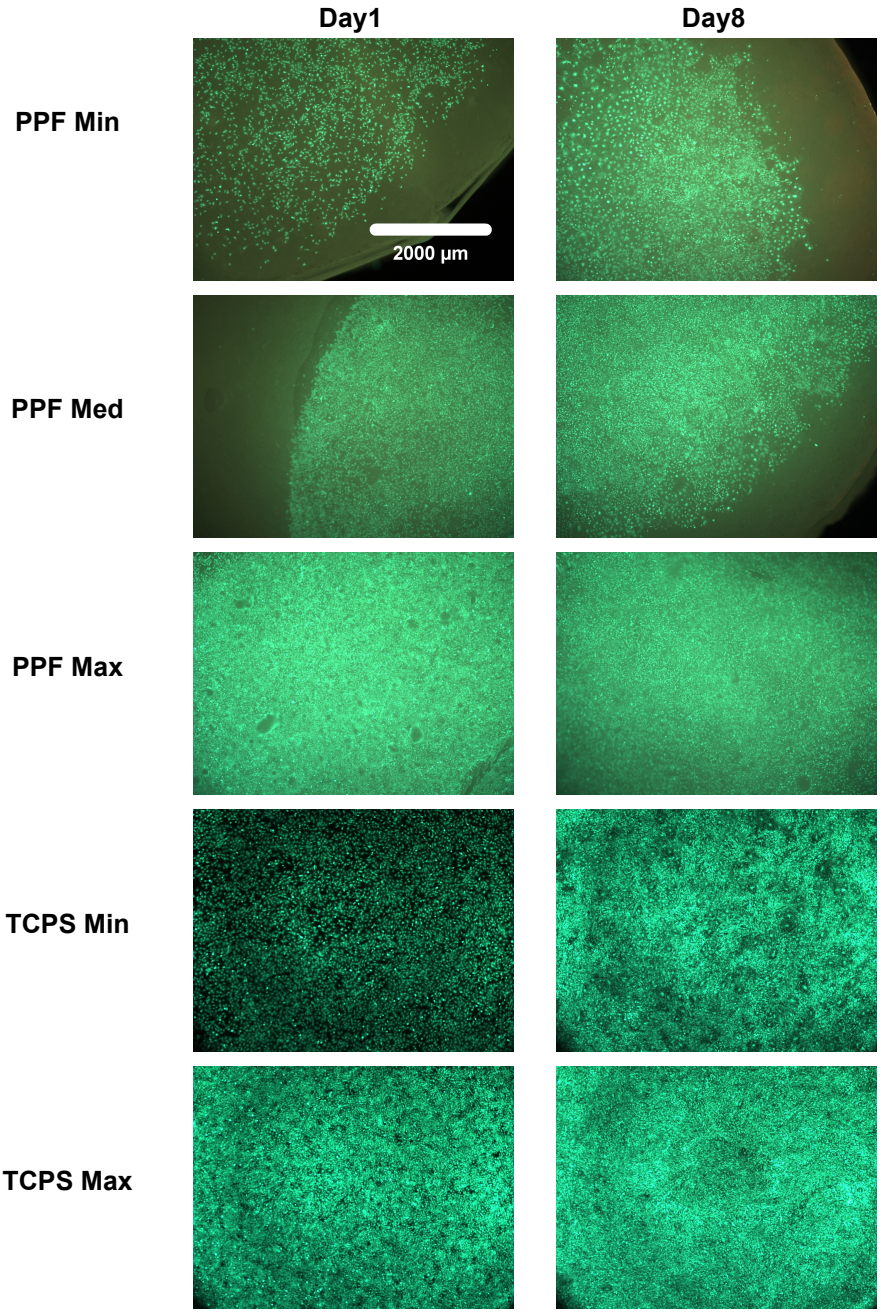

(B)

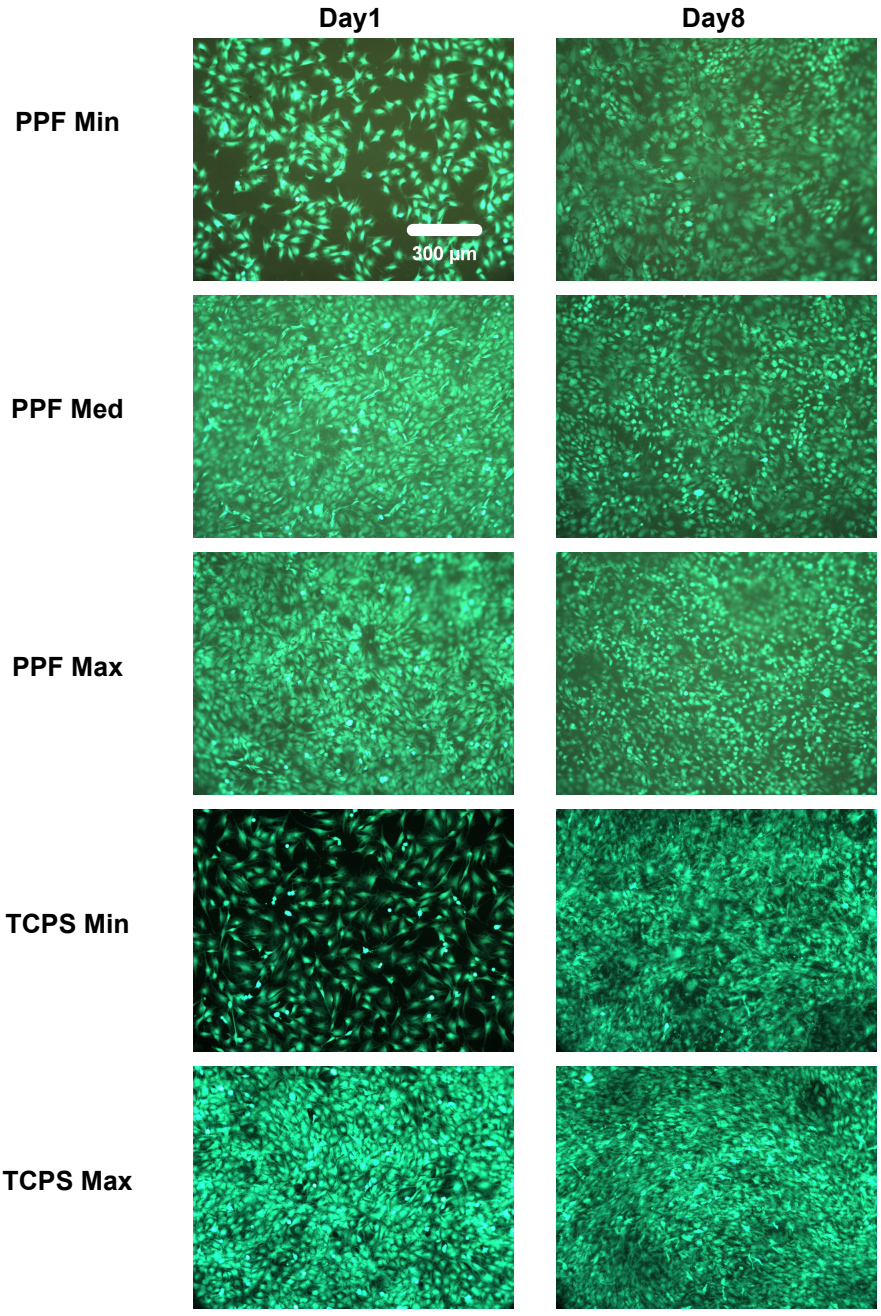

Figure 4: Qualitative Live/Dead fluorescent staining images with a 2.5x magnification in (A) and 10x magnification in (B) of PPF disks and TCPS well plates (positive control). The result demonstrated that rat BMSCs are viable over an 8 day culture period in all experimental groups. The fluorescent images also qualitatively demonstrated a similar attachment pattern and viability of rat BMSCs on PPF disks compared with the control groups. The scale bar shown in 1A represents 2000 µm and applies to all images. The scale bar in 1B represents 300 µm and applies to all images.

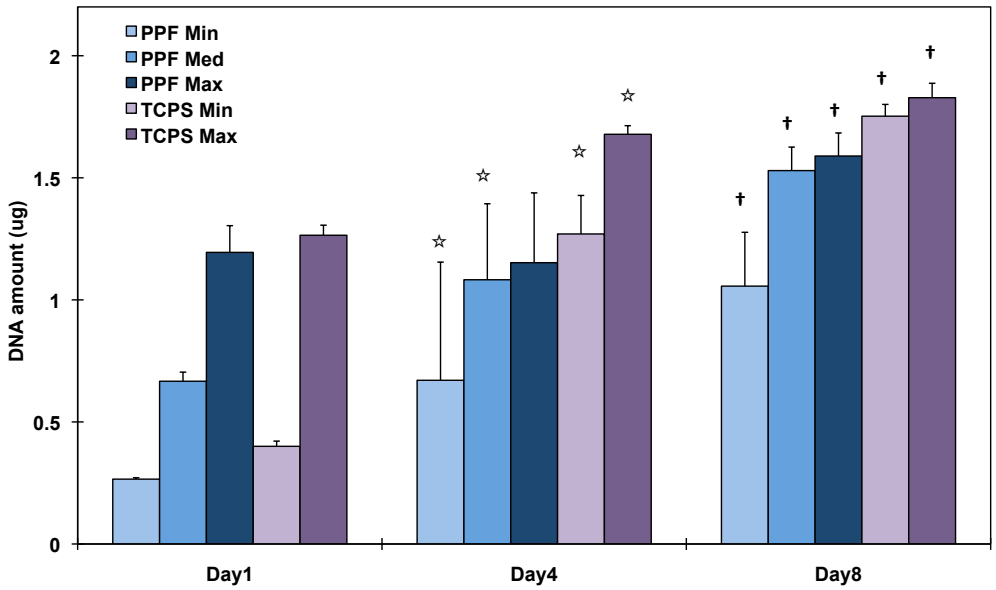

Figure 5: The quantitative DNA amount represents levels of cellular proliferation on the 2D PPF disks and TCPS groups over the course of 8 days (n=3 per group). The DNA amount per experimental group is shown in μg per disk and as average ± standard deviation. ☆ indicates a statistical difference compared to data on day 1 while † indicates a statistical difference compared to data on day 4 in each experimental group ($p<0.05$).

ALP mRNA expression (Figure 6) in the PPF groups showed no significant differences on either day 1 or day 4. ALP expression in the TCPS groups peaked on day 4 and was downregulated on day 8. The lower cell seeding density group (TCPS Min) exhibited higher ALP expression than the higher cell seeding density group (TCPS Max) on day 4. On day 8, the PPF Med group showed statistically higher ALP expression than the Min or Max PPF groups ($p=1.75 \times 10^{-10}$). This ALP mRNA expression pattern at the last time point of day 8 was recorded in all four growth factors. PPF Min and PPF Med groups showed an increase from the initial level of expression by day 4 and this level remained constant until day 8, while ALP

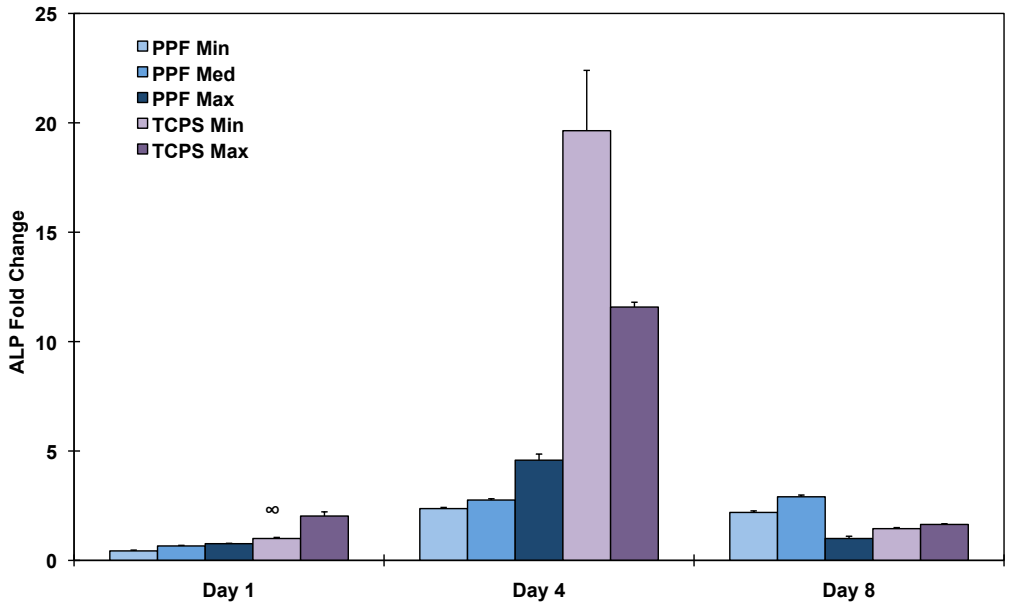

Figure 6: Quantitative RT-PCR analysis of gene expression profiles of ALP osteogenic differentiation markers for 1, 4, and 8 days. The fold changes in gene expression level are reported as average ± standard deviation (n=3) and the calibrator for all experimental groups is indicated by a ∞ marker.

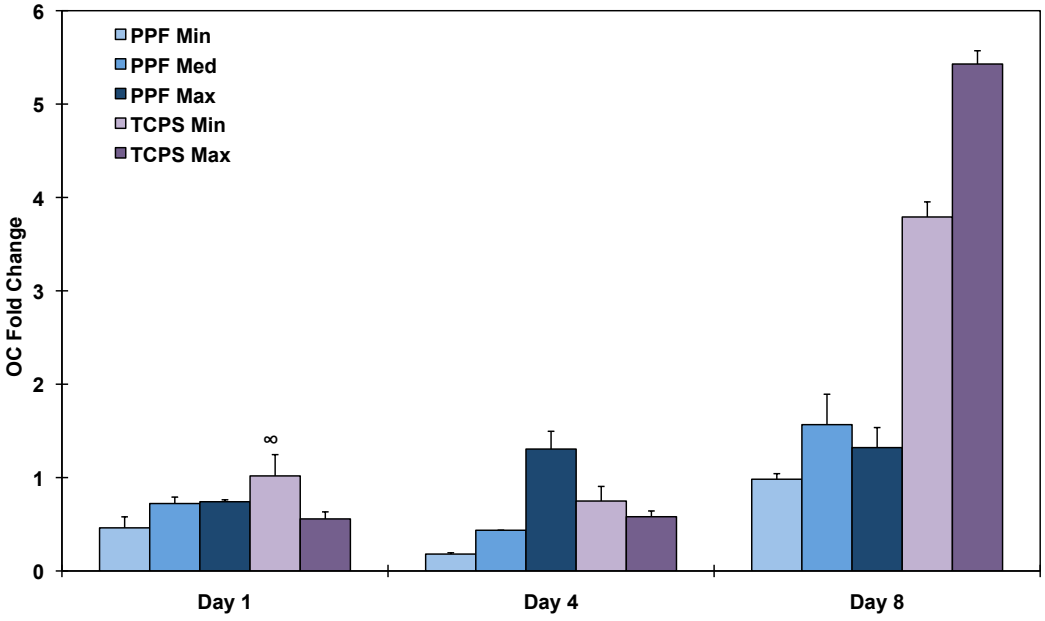

Figure 7: Quantitative RT-PCR analysis of gene expression profiles of OC osteogenic differentiation markers for 1, 4, and 8 days. The fold changes in gene expression level are reported as average ± standard deviation (n=3) and the calibrator for all experimental groups is indicated by a ∞ marker.

expression of PPF Max peaked on day 4 and was more than one-fourth down-regulated on day 8. In Figure 7, all three PPF density groups had similarly low levels of OC expression on day 1. By day 4, the PPF Max group exhibited a higher expression level than all of the other groups. On day 8, there was no significant difference in OC expression between different cell densities on PPF, while TCPS Max showed higher OC expression than TCPS Min and all three PPF groups. All three PPF groups showed an initially constant level of OC expression level that increased when next observed on day 8 (i.e., approximately a two-fold increase compared with day 1). This trend was also observed for the two TCPS groups, where the OC expression level in the TCPS Max group on day 8 was more than nine times that of day 1.

Calcium deposition was assessed by (1) qualitative microscopic images of Alizarin Red S stained specimens, and (2) subsequent quantitative image analysis (Figure 8). The images of stained calcium deposition indicate that all density groups cultured in osteogenic-supplemented media for 8 days demonstrated mineralization, with higher cell density groups of both the PPF and TCPS substrates showing more extensive mineralization (Figure 8A). Data in Figure 8B confirmed the qualitative assessment of the images shown in Figure 8A by showing that the PPF Med and Max groups had significantly larger mineralized areas than were seen in the PPF Min group specimens. Similarly, TCPS Max was found to have a significantly larger area of calcium deposition than was seen in the TCPS Min group.

(A)

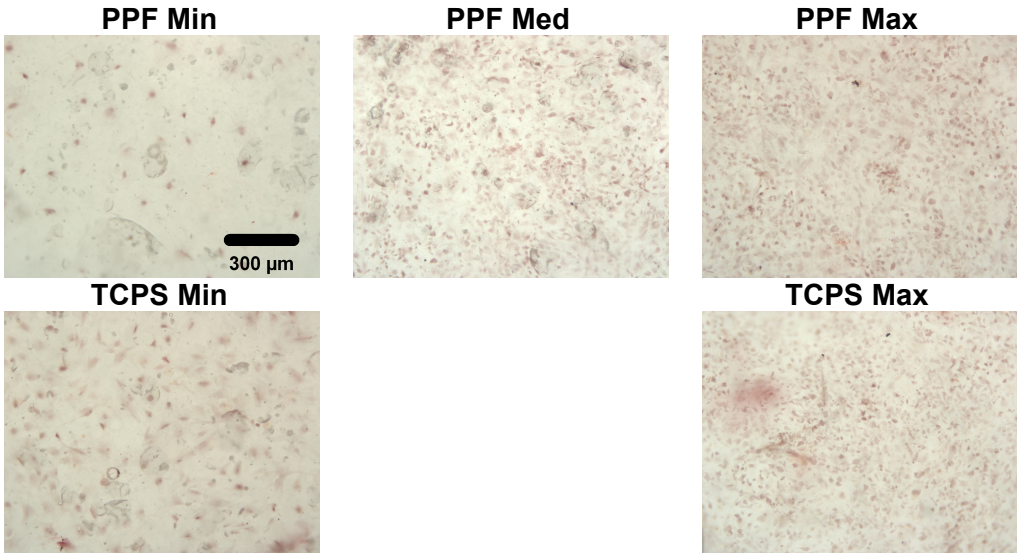

(B)

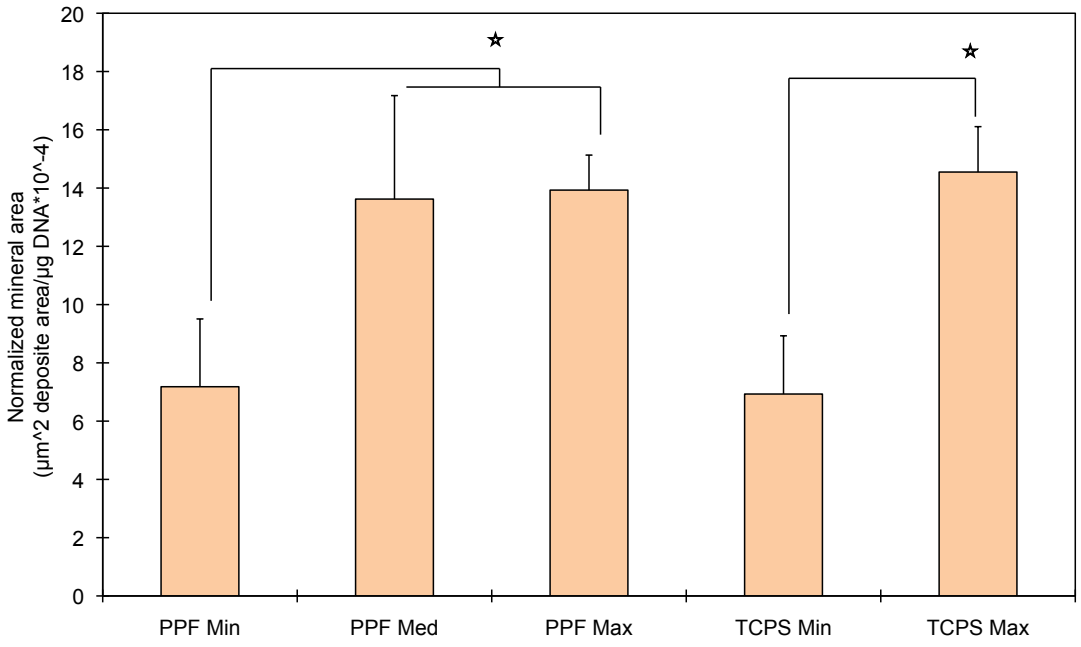

Figure 8: Mineralization assay by Alizarin Red S staining at Day 8. (A) Qualitative light microscopy images of calcium deposits in rat BMSCs. The scale bar represents 300 µm and applies to all images. (B) Normalized calcium deposition. ☆ indicates a statistical difference between groups ($p<0.05$).

4.3.2. Osteogenic Signal Expression

The BMP-2 expression of the PPF Min and Med groups were statistically higher than both the PPF Max and TCPS groups on day 1 ($p = 1.60 \times 10^{-7}$). The PPF Min and Med groups showed a 4-fold downregulation in BMP-2 expression from day 1 to day 4 (Figure 9A). On day 8, the BMP-2 results demonstrated that both the PPF Min and Med groups exhibited significantly higher BMP-2 expression than did the PPF Max samples ($p = 1.60 \times 10^{-5}$), a result that was similar to what was seen on day 1. BMP-2 expression by rat BMSCs on PPF disks was seen to decrease between days 1 and 4 and then, except for PPF Max, to increase by day 8. Consistent BMP-2 expression over 8 days was observed in All TCPS groups.

Figure 9B represents rat BMSC expression of FGF-2. The PPF Max group exhibited a statistically higher level of FGF-2 expression on day 4 versus the PPF Min and Med groups ($p = 3.46 \times 10^{-4}$). The TCPS Min group showed a higher level of FGF-2 expression than all of the other groups at the day 1 and 4 time points. On day 8, all three PPF groups exhibited higher FGF-2 levels of expression than both TCPS groups. The levels of FGF-2 expression in the PPF Med group were higher than that seen in all of other experimental groups ($p = 3.35 \times 10^{-8}$).

(A)

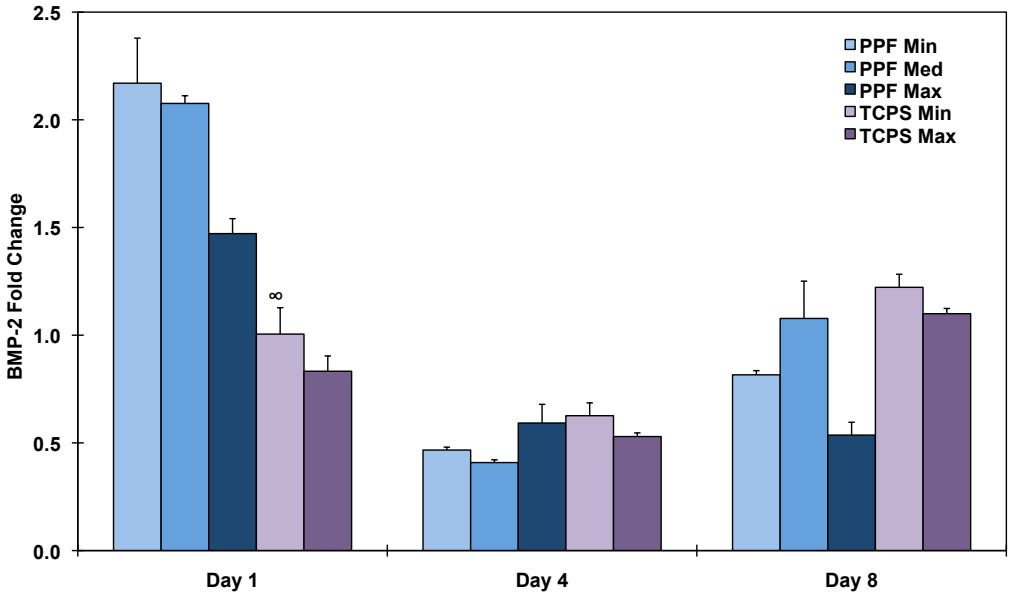
2.5
2.0
1.5
1.0
0.5
0.0
BMP-2 Fold Change
PPF Min
PPF Med
PPF Max
TCPS Min
TCPS Max
Day 1
Day 4
Day 8

(B)

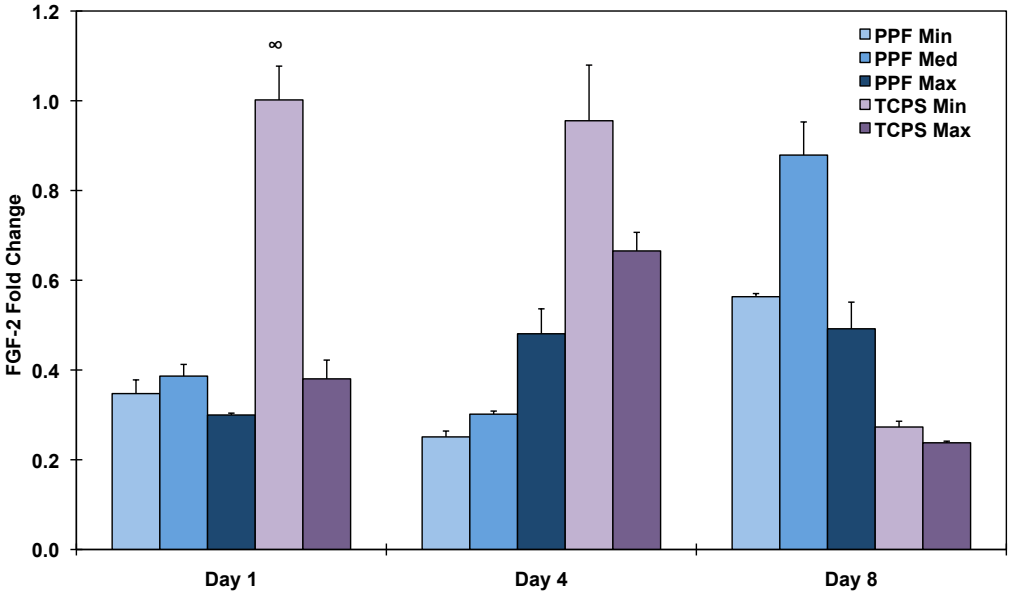
1.2
1.0
0.8
0.6
0.4
0.2
0.0
FGF-2 Fold Change
PPF Min
PPF Med
PPF Max
TCPS Min
TCPS Max
Day 1
Day 4
Day 8

(C)

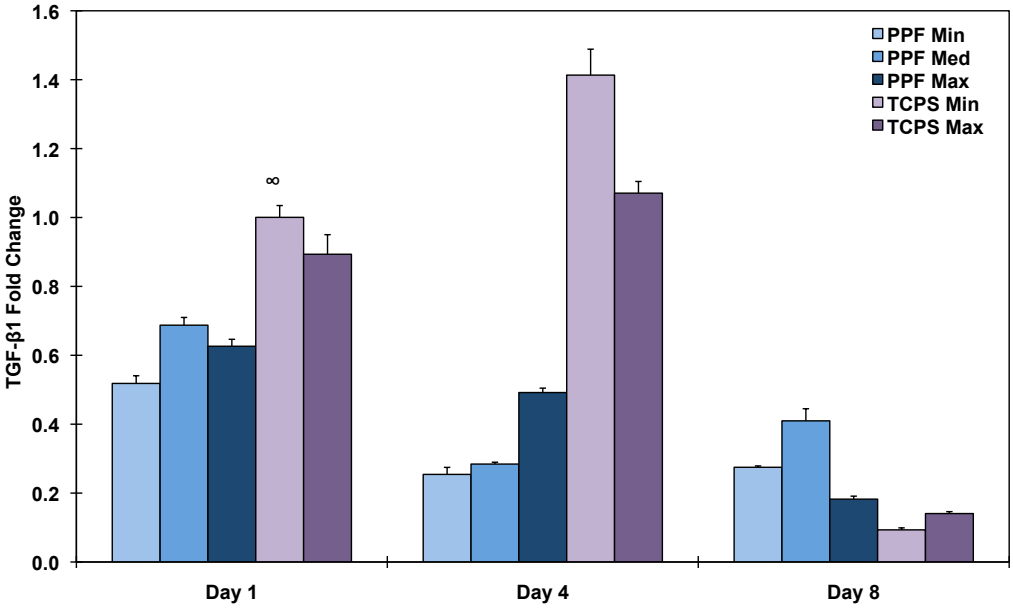

(D)

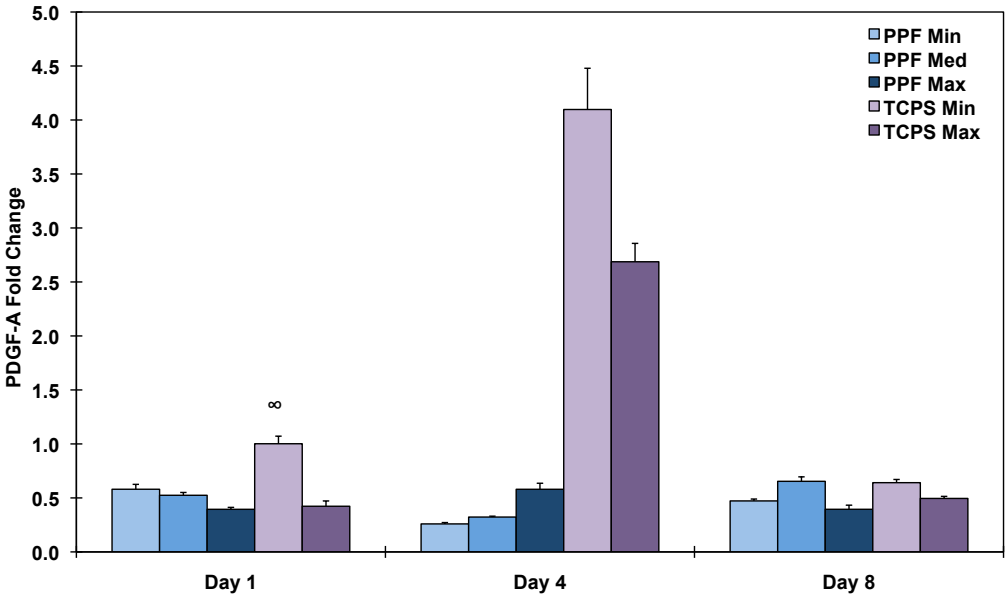

Figure 9: Quantitative RT-PCR analysis of gene expression profiles of growth factors (A: BMP-2, B: FGF-2, C: TFG- β_1, and D: PDGF-A) for 1, 4, and 8 days. The fold changes in gene expression level are reported as average ± standard deviation (n=3) and the calibrator for all experimental groups is indicated by a ∞ marker.

TGF-β_1 expression exhibited a similar pattern to PDGF-A (Figures 9C and 9D). The expression of both TGF-β_1 and PDGF-A in both TCPS groups peaked on day 4, followed by a more than one-fifth fold decrease between day 4 and day 8. The PPF Med and PPF Max groups showed higher TGF-β_1 expression on day 1 than the PPF Min group, while the PPF Max group showed higher TGF- β_1 expression than the other two PPF groups on day 4. The PPF Med group had significantly higher TGF-β_1 expression than all other groups on day 8 ($p= 3.85 \times 10^{-9}$). Overall, rat BMSCs on PPF disks showed decreasing TGF-β_1 expression over 8 days, with a lower expression level than the TCPS groups by day 4. The data in Figure 9D indicates that the PDGF-A levels presented an expression profile similar to the TGF-β_1 expression profile. While the TCPS Min group exhibited a higher PDGF-A expression level than the TCPS Max group at all time points, both the PPF Min and PPF Med groups showed significantly higher levels of expression than the PPF Max group on day 1 only ($p=1.03 \times 10^{-3}$). By day 4, there was no significant difference in PDGF-A expression between all three PPF groups, but the PPF Med group showed a higher level of PDGF-A expression on day 8 than the other two PPF groups ($p=3.99 \times 10^{-6}$). Sustained expression levels were observed in all three PPF groups over the 8 days; however PDGF-A expression levels of rat BMSCs on the TCPS substrate peaked on day 4 and then decreased on day 8.

4.4. Discussion

Intercellular signaling via endogenous signal molecules among a transplanted cell population may be determined as much by the cell population itself as by the

surrounding environment. To mimic a natural bone healing environment, and to optimize the components for an engineered bone substitute, it is of particular importance to characterize the endogenous signaling profiles of that cell population. Cell seeding density, which can alter cell-cell distance, may be a critical parameter controlling subsequent cell proliferation and/or osteogenic signal expression due to changes in paracrine signaling distance among the cells. Furthermore, to determine the optimum seeding density for a specific type of scaffold (i.e., material substrate and surface geometry), it is imperative to stimulate sustained expression of some signals and not others. To this end, we aimed to investigate the effect of initial cell seeding density on the osteogenic gene expression of BMSCs on two dimensional crosslinked PPF disks. Two objectives were addressed in this study: (1) the effect of cell density on rat BMSC viability, proliferation, and osteogenic differentiation and (2) the effect of cell density on signalling profiles of osteogenic growth factors.

We first demonstrated the effect of cell seeding density on the attachment and viability of rat BMSCs (Figure 4). Although it is not possible to conclude there is a direct correlation between cell seeding density and the quality of attachment (or cell viability) from Figure 4, the extent of cellular attachment depends on surface properties of the substrate material. As cell attachment can be affected more by surface wettability and hydrophilicity rather than by surface topology [236], we observed that our PPF disk post-fabrication methods resulted in a suitable environment for the attachment of anchorage-dependent cells such as bone marrow stromal cells and osteoblasts.

Our next goal was to demonstrate the effect of cell seeding density on cell proliferation. As shown in recent literature, cell proliferation is strongly regulated by (1) surface area to allow attachment and (2) contact-inhibition between adjacent cells [243, 246, 252]. Although a highly interconnected porous scaffold is recommended to mimic the native bone, there remains a problem of achieving sufficient seeding efficiency. Alternatively, over-loaded cell numbers may result in limiting nutrient transport, hypoxia of interior cells, and insufficient waste removal from the internal structures. Surface area dependence was also observed in our 2D study, as indicated by a proliferation rate that was lowest in the PPF Max groups (Figure 5). Distribution of rat BMSCs on PPF disks in Figure 1 indicates that lower cell seeding density resulted in a rapid proliferation rate over 8 days. Despite of the fact that high cellularity enhances cell-cell contact, contact-inhibition by gap junctional intercellular communication may suppress cell proliferation [253, 254]. As seen in a previously reported study [252], Figure 5 indicates that contact inhibition reduces cellular proliferation. As a result, we observed that 0.30 million cells per 18 mm diameter PPF disk was sufficient to induce contact inhibition and reduce rat BMSC proliferation rate.

Next, the effect of cell seeding density on the osteogenic differentiation of rat BMSCs was investigated. As a transient early osteogenic differentiation marker, ALP mRNA expression was measured (Figure 6). These data indicate that the PPF Med group exhibited statistically higher ALP expression on day 8 ($p = 1.75 \times 10^{-10}$) and that the PPF Max group showed the lowest expression level. It is known that ALP expression generally peaks prior to mineralization [255]. Since the ALP

expression level in all groups peaked or started to plateau in the middle of the culture period, on day 4, it could be concluded that lower cell density induced early osteogenic differentiation of rat BMSCs after only 8 days. Therefore, it appears to be necessary to optimize rat BMSC cell density in order to stimulate the ALP expression on PPF disks.

Mineralization occurs late during the transition from cellular to osteoid tissue, following a sequential cascade of cell proliferation, ALP expression, and osteoblast phenotypic commitment (i.e., maturation) [256]. As a late marker of osteoid commitment, OC mRNA expression was assessed and calcium deposition was also measured (Figures 7 and 8). OC expression was seen to increase over 8 days and the PPF groups with higher seeding density (i.e., PPF Med and PPF Max) exhibited higher levels of OC expression; OC expression increased significantly in the TCPS Max also by day 8. OC expression, as seen in Figure 7, was consistent with the calcium deposition profile in Figure 8. Thus, the groups with higher cell seeding density presented higher levels of mineralization. Therefore, it would seem that late stage osteogenic differentiation was enhanced by higher cell seeding density, while cell proliferation and early osteogenic differentiation were stimulated by lower cell seeding density.

Our results indicate that three distinct periods in osteoblastic phenotype development may be sensitive to implant cell seeding density. According to the study by Lian and Stein [257], the first period of osteogenic progenitor cell growth exhibits strong proliferation with the formation of extracellular matrix. The second period shows matrix maturation with decreased cell proliferation, and upregulated ALP

expression, a sequence of events also seen in our study. At these two stages, lower cell seeding density might enhance cellular proliferation and ALP expression due to reduced contact inhibition. In contrast, higher cell seeding density may stimulate mineralization, as is expected during the last period of osteoblast formation, along with downregulation of ALP activity and synthesis of osteopontin and bone proteoglycans such as decorin and biglycan. As described earlier, the rat BMSCs temporal growth pattern observed in this study agreed well with the expected cascade of bone formation events. Our observation also suggests that it may be possible to use cell seeding density to promote osteogenic differentiation in a 2D environment. However, optimization of cell seeding density needs to be tested in a 3D scaffold in order to confirm our hypothesis of the consistency between 2D and 3D microenvironments and the possibility of promoting the healing of bone wounds through the use of a tissue engineered implant.

Finally, qRT-PCR was performed to investigate the gene expression profile of endogenous growth factors relevant to bone formation, including BMP-2, FGF-2, TGF- β_1, and PDGF-A1. Natural bone matrix contains a number of growth factors and these growth factors play a critical role in proliferation, differentiation, and other cellular activities that are associated with these signaling molecules [194]. BMP-2 is one of the most investigated signaling molecules in the field of bone biology due to the following hypothesized roles: (1) regulation of cell growth, differentiation, apoptosis, and organ development, and (2) induction of osteoprogenitor cells found in bone fracture sites that are healing [192]. As shown in Figure 9, the two lower density PPF groups had significantly higher BMP-2 expression than did the PPF Max

group on day 1 ($p = 1.60 \times 10^{-7}$). The general trend of BMP-2 expression level over culture periods showed a decline on day 4 and then increased again by day 8. This expression pattern is the opposite of the ALP mRNA expression profile (i.e., peaked on day 4 and downregulated again by day 8), and this may be due to the opposing signal transduction for BMP-2 and ALP during early osteogenic differentiation. BMP-2 is thought to induce ALP production through Wnt expression and the Wnt/LRP5 signaling cascade [258]. Early expression of BMP-2 on day 1 might result in a BMP-2-rich extracellular environment. Subsequently, perhaps through the Wnt autocrine loop, ALP expression was observed to be downregulated by day 4 in our study. This expression profile can be found in other studies with 3D titanium scaffolds seeded with rat BMSCs [259] and 3D coralline hydroxyapatite scaffolds seeded with human mesenchymal stem cells (hMSC-TERT4) [255]. Interestingly, the PPF Med group showed higher expression of BMP-2 than the other two PPF groups on day 8, indicating that cell seeding density might be useful as a means to alter or optimize the BMP-2 expression of rat BMSCs.

It has been suggested that FGF-2 is associated with (1) regulation of skeletal growth and development including the balance between bone forming cells and bone resorbing cells, and (2) stimulation of osteoblasts by activating the Cbfa-1/Runx2 transcription factor [18, 260]. FGF-2 expression in Figure 9B was initially sustained on the PPF disks by day 4, but increased at day 8, showing significantly higher expression levels than in the TCPS groups. An increasing trend of FGF-2 expression at later time points may be due to Runx2-mediated signal transduction. FGF-2 expression is thought to activate Runx2 upregulation via the mitogen-activated

protein kinase (MAPK) pathway, but Runx2 upregulation can also be induced by BMP-2 or TGF- β_1 stimulation via Smad and the MAPK intracellular signaling pathway [18, 261]. We also speculate that an early decline of BMP-2 expression may deactivate Runx2, and subsequently enhance FGF-2 expression in order to restore Runx2 activation via the MAPK pathway.

This hypothesis about the intracellular signaling pattern that is associated with growth factor signaling found during bone formation may also be applied to TGF- β_1 expression in Figure 9C. The decease in TGF- β_1 expression over time was similar to the BMP-2 expression profile, and it may also contribute to Runx2 deactivation and subsequent FGF-2 expression. This is consistent with the PPF Med groups on day 8 that presented statistically higher FGF-2 ($p = 3.35 \times 10^{-8}$) and TGF- β_1 ($p = 3.85 \times 10^{-9}$) expression levels. This result may suggest that over a period of 8 days rat BMSC cultures on PPF disks require an optimized cell density of approximately 75,000 cells per cm^2 (0.15 million cells/disk) to induce an optimal FGF-2 and TGF- β_1 expression profile that is compatible with bone formation. This may also suggest that there is an optimal cell seeding density for 3D scaffolds that is necessary to induce and/or promote the osteogenic differentiation and bone healing cascade.

Finally, it is also been observed that PDGF-A may stimulate DNA synthesis during in vitro bone formation [262]. In the present study, sustained PDGF-A mRNA expression was not correlated with DNA content (Figures 5 and 9D). However, the difference of PDGF-A expression patterns over 8 days between the PPF and TCPS groups might indicate a substrate dependence in the expression of this growth factor.

4.5. Conclusions

The optimum level of bone progenitor cell seeding density for many different implant engraftment strategies is a critical issue for the clinical application of bone tissue engineering. The present study indicates that varying cell seeding density on PPF disks may be utilized to enhance the proliferation and differentiation of rat BMSCs. This study demonstrated (1) the effect of cell seeding density on viability, proliferation, and differentiation of rat BMSCs, and (2) the endogenous growth factor mRNA expression profiles of rat BMSCs on 2D PPF disks. The results of this study revealed that: (1) cell proliferation rate and early osteogenic differentiation were stimulated by a lower cell seeding density, (2) later differentiation, as indicated by mineralization, was enhanced by increasing cell seeding density, and (3) the temporal gene expression profiles of endogenous growth factors can be altered by initial cell seeding density.

Chapter 5: Osteogenic Signal Expression of Rat Bone Marrow Stromal Cells is Influenced by Both Hydroxyapatite Nanoparticle Content and Initial Cell Seeding Density in Biodegradable Nanocomposite Scaffolds

5.1. Introduction

Calcium phosphate bioceramics, such as hydroxyapatite (HA) and tricalcium phosphate (TCP), are promising materials for bone tissue engineered composites due to their mineral composition reflecting native bone tissue both chemically and structurally, with the latter being in regards to their nano-scale features. HA especially is known to posses biocompatibility and osteoconductivity as well as to enhance the functionality of composite materials when combined with biodegradable polymer matrices. However, 3D scaffolds fabricated with only HA or other ceramic materials often exhibit brittleness, difficult manufacturing, and slow degradation rates. Therefore, incorporation of HA within a degradable polymeric network may provide a more favorable synthetic microenvironment to more closely mimicking natural tissue physiology with the additional properties of a higher mechanical strength. Since fabrication of HA/biopolymer composites could take advantages of the properties of both the components, there have been many studies utilizing the incorporation of HA with various synthetic polymers including poly(D,L-lactic acid-co-glycolic acid) (PLGA) [263-265], poly(L-lactic acid) (PLLA) [266], poly(propylene fumarate) (PPF) [236, 267], poly(caprolactone) (PCL) [268], a copolymer [269], and a cyclic acetal hydrogel [270, 271].

Nanoscale features of HA particles exhibit more advantageous cellular responses when compared to microsized HA particles. For example, HA nanoparticles coated on glasses demonstrated higher MG-63 cell attachment and proliferation than microsized HA particles due to higher surface area for cell adhesion and lower crystalinity [272]. Similarly, HA nanoparticles embedded in 3D PCL scaffolds have shown enhanced levels of attachment, proliferation, alkaline phosphatase activity, and calcium deposition (i.e., mineralization) of mesenchymal stem cells (MSC) [268]. Therefore, the size of HA particles can affect cell response, particularly attachment, proliferation, and maturation. If nanocomposite materials produced favorable conditions for tissue formation, they could be a candidate material to improve the surface properties of bone tissue substitutes.

Poly(propylene fumarate) (PPF) offers a variety of advantageous properties as a bone substitute material including degradability in physiological environments and suitable mechanical strength. Crosslinked PPF networks can be fabricated via ultraviolet (UV) radiation with the aid of a photoinitiator such as bis(2,4,6-trimethylbenzoyl) phenylphosphine oxide (BAPO) [273]. This photoinitiation technique for crosslinking allows PPF to be used as a resin material for stereolithography, other additive manufacturing strategies, or even as a translucent mold [102, 104, 105]. PPF composite scaffolds incorporating nanosized materials such as alumoxane [163, 274-276], carbon nanotubes [159], and β-TCP [8, 277] have exhibited improved mechanical properties, enhanced cell attachment, and increased osteoconductivity in an in vivo model. Moreover, PPF/HA composite materials have also shown the superior cell/tissue responses. Specifically, HA incorporation has been

observed to improve MC3TC cell proliferation on 2D PPF composite disks over a 7 day period of in vitro culture [236]. In an in vivo study using rat tibia metaphysic implantation, 3D composite scaffolds with PPF and HA particles with 40 nm in diameter showed a faster rate of new bone formation in tibial defect sites than PPF/microsized HA scaffolds, resulting in superior osseointegration [267]. However, the effect of HA addition to PPF on the endogenous gene expression of a seeded cell population at the molecular level has not previously been investigated, and is the subject of this study.

Heterogeneous bone marrow stromal cell (BMSC) populations may contain mesenchymal stem cells. Lineage specific differentiation of BMSCs on synthetic scaffolds depends upon effective induction of particular signal molecules such as growth factors, hormones, and cytokines, associated with the desired lineage. One of the crucial factors facilitating osteogenic signal expressions may be cell-to-cell distance, which potentially alters paracrine signaling mechanisms. Another factor may be scaffold construction parameters such as 3D geometry or surface properties. In our previous study, the initial cell seeding density of 2D PPF disks was found to be a factor contributing to the enhancement of requisite osteogenic signal expression of implanted heterogeneous cell populations [273]. In addition to the surface modification of 3D PPF scaffolds through the addition of HA nanoparticles, changing the cell-cell signaling distance by varying the cell seeding density may similarly affect the cellular responses within 3D porous environments. There have been many studies describing the effects of cell seeding density on osteolastic differentiation in 3D scaffolds, and it has been observed that an optimal cell seeding density in a 3D

environment may enhance this response and thus promote tissue regeneration [246, 278-280].

Moreover, controlling construction parameters to optimize engineered bone substitutes could affect various cellular functions such as attachment, migration, proliferation and differentiation. In order to achieve the optimized properties of 3D scaffolds inducing host cell integration, we fabricated 3D macroporous composite scaffolds with PPF/HA nanoparticles by porogen leaching techniques and a photocrosslinking reaction. Using these scaffolds, we investigated how both the surface properties altered by HA nanoparticle incorporation and the intercellular signaling distance changed in relation to cell seeding density. The global hypothesis in this study is that the modification of 3D composite scaffold microenvironment of may facilitate enhanced osteogenic signaling among the implanted cell population, where both incorporation of HA nanoparticles and alteration of paracrine cell-cell signaling distance could be controlling parameters. The specific objectives of this study were: (1) to fabricate and characterize the physical properties of the 3D macroporous PPF/HA scaffolds, (2) to investigate the effects of HA content and initial cell seeding densities on osteoblastic differentiation of rat BMSCs, and (3) to determine whether endogenous osteogenic growth factor gene expression profiles would be influenced by 3D macroporous PPF/HA scaffolds.

5.2. Materials and Methods

5.2.1. PPF/HA composite scaffold fabrication

PPF was synthesized as described previously [234, 273]. PPF with number average molecular weight (Mn) of 1300 g/mol and PDI of 3.7 was used throughout this study. Purified PPF was heated to reduce the viscosity and first mixed with 0.5 wt% of BAPO (Ciba Specialty Chemicals Corp., Tarrytown, NY). For composite disk and scaffold fabrication, HA nanoparticles (100 nm, Berkeley Advanced Biomaterials, Berkeley, CA) with the ratio of 0, 10, and 20% of PPF:HA were incorporated into the PPF/BAPO mixture. For 2D solid disks, the PPF/BAPO/HA mixture without any porogen was uniformly placed between the glass plate and crosslinked in an ultraviolet (UV) light box (intensity of 2.68 mW/cm^2) for 2 hrs. Crosslinked composite sheets were cut into the disks with 18 mm in diameter and 1.5 mm thickness. For 3D macroporous scaffolds, the PPF/BAPO mixture was homogeneously mixed with a NaCl porogen (180 - 300 μm, 75 wt %) and HA nanoparticles, respectively. The total mixture was then packed into a glass mold. After 2 hr of UV radiation, the crosslinked PPF/HA cylinders were retrieved by breaking the glass molds and cut into small disks (6.5 mm in diameter and 3 mm in thickness). The disks were then placed in the water for 72 hr to leach out the NaCl porogen. After salt leaching, the resulting macroporous scaffolds were dried and post-cured in the same UV light box for 2 hr. Both 2D disks and 3D scaffolds were washed in acetone for 3 min to dissolve any unreacted components, and air trapped in the inner pores of the scaffold were removed by creating a vacuum by drawing air from a tube with a syringe. The scaffolds were then washed twice with PBS to

remove the residual acetone. Finally, the samples were then either characterized after complete drying or sterilized in 70 % EtOH for cell seeding in subsequent in vitro experiments.

5.2.2. Surface morphology, particle distribution, and atomic composition

A scanning electron microscope (SEM) (SU-70, Hitachi, Tokyo, Japan) was used to examine the morphology of the top surface of the composite substrates and the surface distribution of HA particles on the 2D composite disks. SEM images were obtained after gold sputter coating. Concurrently, the presence of the HA nanoparticles onto the composite surfaces and their atomic composition were assessed by energy dispersive spectroscopy (EDS).

5.2.3. Surface roughness and topography

The surface roughness and topography of the 2D disks was examined by an atomic force microscope (AFM) (Asylum Research, Santa Barbara, CA). The topography of the surface (i.e., a height image) was captured in a tapping mode with 20 x 20 μm^2 scan size and 1 Hz scan rate. A silicon tip with a spring constant of 48 N/m was used for all scans. The height images were flattened with a zero order polynomial function and converted to 3D images. The root mean square (RMS) roughness was calculated from processed images. This test was completed with four replicates in each experimental group (n=4).

5.2.4. 3D PPF/HA composite scaffold characterization

For 3D porous scaffolds, top surface, cross-section, and particle distribution onto the surface were observed by SEM. HA distribution over the 3D macroporous scaffold was qualitatively determined by the simple trypan blue staining as previously described [157, 281]. Briefly, scaffolds were soaked in a 0.4 (w/v) trypan blue for 10 sec with vigorous shaking. After washing the samples twice with diH_20, each scaffold was placed in 100% EtOH for 1 min and sonicated for 5 sec to remove any unbound dye. A top surface image of uniformly stained scaffolds depicting the distribution of HA within each composite scaffold was acquired. The level of adsorbed protein onto the scaffold surface was measured by a previously described method [172]. Briefly, the scaffolds were first completely wetted by a series of pre-soaking: 1hr in ethanol, 2 x 30 min in PBS, and overnight incubation in PBS. Samples were then placed in culture media with 10% FBS for 4 hr at 37°C on a shaker table (25 rpm). After incubation, samples were washed with PBS three times, and adsorbed proteins were extracted during two cycles of 1 hr incubation in 250 μl of 1% sodium dodecyl sulfate solution. A BCA protein assay kit (Pierce, Rockford, IL) was used to determine protein concentration. This test was completed with triplicate samples and triplicate measurements.

5.2.5. Mechanical testing

Compressive mechanical testing was conducted according to the American Society of Testing Materials Standard D695-2a using an Instron mechanical tester (Instron 5565, Norwood, MA). Scaffolds with the PPF:HA ratios of 0, 5, 10, 15, and

20% were prepared as cylinders with 13 mm in height and 6.5 mm in diameter. Samples were compressed along their vertical axis at a speed of 1.3 mm/min until the compressive strain reached 0.5 mm/mm. The Young's modulus and yield compressive stress at 1% offset were calculated using Bluehill 2.16 software (Instron). This test was completed with five replicates in each experimental group.

5.2.6. Flow cytometry analysis

Flow cytometry was performed at the Bioengineering Flow Cytometry Core Facility at the University of Maryland. Briefly, rat BMSCs were isolated from the femurs and tibias of young male Wistar Hanover rats (101-125 g, Taconic) according to methods previously described [273]. Both harvested bone marrow and 3rd passaged cells were then placed in red cell lysis buffer (10 mM $KHCO_3$, 150 mM NH_4Cl, 0.1 mM EDTA for 10 min and washed once with complete media. Approximately 1×10^6 cells were transferred to a 5 ml BD Falcon polystyrene tube and labeled for the following antibodies: CD45-Alexa Fluor 647 (clone OX-1, Biolegend, San Diego, CA); CD29-FITC (clone Ha2/5, BD Biosciences, San Jose, CA); CD90-PE (clone OX7, Santa Cruz Biotech, Santa Cruz, CA); CD34-PE-Cy7 (clone ICO115, Santa Cruz Biotech); and CD44 (clone OX49, Santa Cruz Biotech) with goat anti-mouse Alexa Fluor 700 (Invitrogen, Carlsbad, CA), as well as unstained and appropriate isotype controls, and a panel stain including all surface markers. Each tube was washed with 2 mL FACS staining buffer (1x PBS/1% FBS) and centrifuged for 5 min at 500 rpm at 4°C. The supernatant was discarded and the pellet was resuspended in 200 µl FACS staining buffer and the appropriate antibodies

were added. The tubes were incubated on ice for 20 min during antibody binding in the dark and then washed twice with 2 ml of PBS and centrifuged for 10 min at 500 rpm at 4°C. The supernatant was discarded and the pellet was resuspended in the final volume of 500 µl. The samples were analyzed on a BD FACSAria II flow cytometer BD Biosciences (San Jose, CA) and the data was analyzed using the BD FACSDiva software.

5.2.7. 2D attachment of rat BMSCs

2D PPF/HA composite disks were pre-washed after acetone etching prior to cell seeding in the following manner. Each disk was sterilized with 70% EtOH for 30 min and washed twice with PBS buffer. Then, the disks were soaked in FBS overnight to increase the level of adsorbed serum protein on the composite surfaces. Each disk was then placed in a 12 well plate and an autoclaved stainless steel ring (inner diameter: 16 mm) was also placed onto each disk to confine the seeding area as well as prevent floating of disks [273]. Rat BMSCs in culture flasks that had undergone 3 passages were trypsinized, resuspended in osteogenic (OS) media (Control media contained α-MEM, 10% (v/v) penicillin/streptomycin antibiotics, and 0.2 mM of ascorbic acid while OS media was made of control media supplemented with 10 mM Na-β-glycerophophate and 10^{-8} M dexamethasone) with 10% FBS, and seeded onto composite disks (60,000 cells per disk, 30,000 cells/cm^2) as well as tissue culture polystyrene (TCPS) well plates as a positive control. After 24 hr incubation, the cells on the disks were washed with PBS and stained with 2 µM calcein acetoxymethylester (Calcein AM, Invitrogen) for 30 min at room temperature.

Images were obtained using a fluorescence microscope (Axiovert 40 CFL with filter set 23, Zeiss, Thornwood, Swiss) equipped with a digital camera (Diagnostic instruments 11.2 Color Mosaic, Sterling Heights, MI) from five spots (i.e., one in the center and four along each major axis) to quantify the percent attachment area of cells compared to the TCPS control. A total of 20 images (four biological replicates) were acquired and transferred to Matlab software (The MathWorks, Natick, MA) and converted to black and white binary images. The percentage of cell attachment (total cell attached area per group / total cell attached area in the TCPS group × 100%) was determined.

5.2.8. 3D cell culture

3D PPF/HA composite scaffolds were also pre-washed, as described above, before cell seeding. PPF/HA scaffolds were sterilized in 70 % EtOH and soaked in FBS, and then the cells were seeded onto the scaffold. One million cells per scaffold were seeded for the visualization assays while scaffolds with two different cell densities (0.33 million and 1 million cells per scaffold) were tested for alkaline phosphatase (ALP) expression, mineralization, and quantitative real time polymerase chain reaction (qRT-PCR) experiments (see the experimental groups in Table 10). The OS media was changed every 2 days until day 8.

Groups	PPF Content (wt%)	HA Content (wt%)	Porosity (wt%)	Cell Density (cells/scaffold)
0 High	100%	-	75.83 ± 0.80%	
10 High	90%	10%	76.54 ± 0.35%	1.00×10^6
20 High	80%	20%	76.25 ± 1.10%	
0 Low	100%	-	75.83 ± 0.80%	
10 Low	90%	10%	76.54 ± 0.35%	0.33×10^6
20 Low	80%	20%	76.25 ± 1.10%	

Table 10: Experimental groups for 3D in vitro culture.

5.2.9. Visualization of cells on the 3D scaffolds

Cell viability was assessed up to day 8 following cell seeding on 3D PPF/HA scaffolds by using Calcein AM fluorescent staining. The cell culture media was removed and the cell/scaffold constructs were rinsed twice with PBS. Staining and microscopic procedures were performed as described previously. The cytoskeleton development of rat BMSCs on composite scaffolds was assessed by F-actin staining. After the aspiration of media from each well, each scaffold was washed with PBS, fixed with 500 µl of 4% paraformaldehyde for 30 min, washed three times with PBS, and then incubated in 500µl of 0.2% Triton X-100 in PBS for 2 min. Samples were then washed twice with PBS again, and incubated in 700 µl of phalloidin (Alexa Fluor 488, Invitrogen) for 1 hr at room temperature. Stained cytoskeletons were observed under a fluorescence microscope. Cell morphology on the composite surfaces was also examined by SEM. After cell culture media removal, each scaffold was washed with PBS, fixed with 500 µl of 4% paraformaldehyde for 30 minutes, and washed again with PBS three times. Samples were air-dried over night, coated

using a gold sputter, and observed via SEM. All three assays were performed on day 1 and 8.

5.2.10. Quantitative reverse transcription polymerase chain reaction (qRT-PCR)

Total RNA was isolated from cell/scaffold constructs using Trizol (Sigma-Aldrich) according to the manufacturer's protocol. cDNA was prepared from the isolated RNA using a High Capacity cDNA Archive kit (Applied Biosystems, Foster City, CA). Pre-amplification of cDNA was performed by the manufacturer's protocol. Briefly, the cDNA sample was mixed with 0.2X pooled Taqman Gene Expression assay mixture (Applied Biosystems) of genes of interest, and a PreAmp Master Mix (Applied Biosystems). The genes of interest included three growth factors (bone morphogenetic protein-2 (BMP-2, Taqman Assay ID: Rn00567818_m1), fibroblast growth factors-2 (FGF-2, Rn00570809_m1), and transforming growth factor-β1 (TGF-β1, Rn00572010_m1)), one transcriptional factor of Runx2 (Rn01512296_m1), and one osteoblastic differentiation marker of osteocalcin (OC, Rn00566386_g1). The thermal condition for the pre-amplification reaction was 10 min at 95°C, and 10 cycles of 15 sec at 95°C and 4 min at 60°C. This pre-amplified cDNA sample was diluted with 1x TE buffer (1:5) and then was utilized to investigate the relative gene expression level of target genes. A house-keeping gene, glyceraldehyde-3-phosphate dehydrogenase (GAPDH, Rn99999916_s1) was used as an endogenous control gene. qRT-PCR was conducted on an ABI Prism 7000 sequence detector (Applied Biosystems), using a thermal condition of 2 min at 50°C, 10 min at 95°C, and 50 cycles of 15 sec at 95°C and 1

min at 60°C. The relative gene expression level of the genes of interest was normalized using the GAPDH control gene. The mean of fold changes compared to the calibrator group (0 Low Group at day 1) was analyzed using a ΔΔCt method and its standard deviation is reported (n=3).

5.2.11. Alkaline phosphatase assay

ALP activity was determined using p-nitrophenyl phosphate (pNPP) enzymatic assay (Sigma-Aldrich, St. Louis, MO) based on the hydrolysis of pNPP to para-nitrophenol, where spectroscopic data of the final yellow product indicates ALP activity. The cell/scaffold constructs were washed with PBS and placed in 600 µl of autoclaved distilled water. Protein and DNA were extracted through three cycles of cell-lysis: freeze (30 min at -80°C), thaw (30 min at 37°C), and sonication (30min). The resulting debris was centrifuged at 12,000 g for 10 min and the supernatant was transferred to a new sterile tube. The supernatant was mixed with a pNPP liquid substrate and after 1 hr incubation at 37°C in the dark, 2 M NaOH solution was added to stop the reaction. The absorbance was recorded at 405 nm using a M5 SpectraMax microplate reader (Molecular Devices, Sunnyvale, CA). The DNA amount was also quantified using a PicoGreen assay kit (Invitrogen) and the ALP activity level was normalized to the DNA amount and the mM ALP/µg DNA was reported. Each experimental group was analyzed in triplicate.

5.2.12. Mineralization assay

Calcium mineralization was measured by selective binding of alizarin Red S (ARS, Sigma-Aldrich) to calcium salts. On day 8 and 15, cell/scaffold constructs were washed with PBS, fixed with 4% paraformaldehyde for 30 min at room temperature, and then stained with 40 mM ARS/PBS solution (pH 4.1) on the shaker (150 rpm) for 30 min at room temperature. After washing five times with dH_2O to remove any unbound ARS, 10 v/v% acetic acid was applied to each sample to dissolve the crystals. Optical density was recorded at 405 nm using a microplate reader and the background intensity of a control scaffold (i.e., a scaffold without cells) was subtracted from each sample. The calcium amount was normalized to the DNA amount and mM ARS/μg DNA was reported. Each experimental group was analyzed in triplicate.

5.2.13. Statistical analysis

The data from all studies were analyzed by an analysis of variance (ANOVA) and Turkey's multiple-comparison test. A p value < 0.05 was utilized to demonstrate significant difference between the experimental groups. The means and the standard deviations were reported in each figure.

5.3. Results

5.3.1. 2D surface characterization

The PPF/HA composite material was fabricated through a simple physical mixing technique and a crosslinked PPF network was obtained by UV light photoinitiation. The surface morphology and atomic composition on the composite surface were observed by SEM imaging and EDS analysis. In addition, the surface topography and RMS roughness were assessed by AFM. Increasing the amount of HA nanoparticles incorporated within a PPF polymer network resulted in more particles being exposed on the composites material's surface (Figure 10(A), (C), and (E)). Atomic composition data is correlated with these morphological surface images (Table 11). By adding more HA nanoparticles, more calcium and phosphate are detected onto the composite surface. HA incorporation also resulted in increasing surface roughness (Figure 10(B), (D), and (F)). 3D height images using AFM also qualitatively demonstrated that a rougher surface was obtained by mixing larger amounts of HA particles into the PPF. RMS roughness data in Figure 10(G) shows a significant increase in roughness in the PPF/HA 10% and 20% groups compared to the PPF control group ($p = 2.96\times10^{-6}$). Moreover, these two groups also shows a significant increase in roughness when simply etched by acetone compared with non-etched samples ($p = 4.79\times10^{-4}$ and 3.18×10^{-5}, respectively) implying that some portion of the embedded HA particles in PPF were exposed by acetone washing and resulted in a rougher surface than in either the PPF control or the non-treated PPF/HA samples. Therefore, the PPF/HA composite fabrication techniques by physical mixing,

photocrosslinking reaction, and acetone etching are suitable to create higher surface roughness with a different chemical composition.

5.3.2. 3D scaffold characterization

SEM analysis was also performed on the structure of 3D macroporous PPF/HA scaffolds (Figure 11). Top surface (Figure 11(A)) and cross-section (Figure 11(B)) images demonstrated highly interconnected 3D porous structures. The overall porosity measured by the amount of salt leached (see data in Table 10) is correlated with this SEM observation. All three experimental groups showed over 75 wt% of leaching (n=6), implying that the pores in the scaffold are interconnected which would allow water to flow through the inner structure. For the higher magnification of the surface of 3D PPF/HA scaffolds, the same trends associated with HA particle distribution were observed, as were seen on the 2D disks (Figure 11(C)). This suggests that a simple porogen leaching technique could be applied to fabricate well-interconnected 3D PPF/HA scaffolds with high porosity. The compressive Young's modulus of porous PPF/HA scaffolds showed an increasing trend as the concentration of HA increased (Figure 12(A)). Specifically, the PPF/HA 20% group showed a significantly higher modulus than either the PPF control or the PPF/HA 10% group ($p = 1.05\times10^{-2}$). The offset yield strength in PPF/HA 20% was also higher than in the other groups (Figure 12(B)). In addition, the adsorption of hydrophilic trypan blue dye to the composite scaffolds qualitatively demonstrated the uniform distribution of the HA particles as well as an increasing potential to adsorb dye by increasing the

(A)

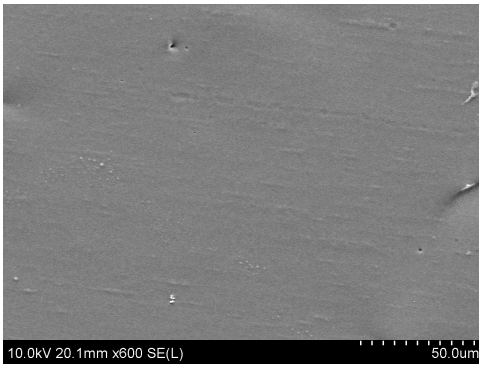
10.0kV 20.1mm x600 SE(L)
50.0um

(B)

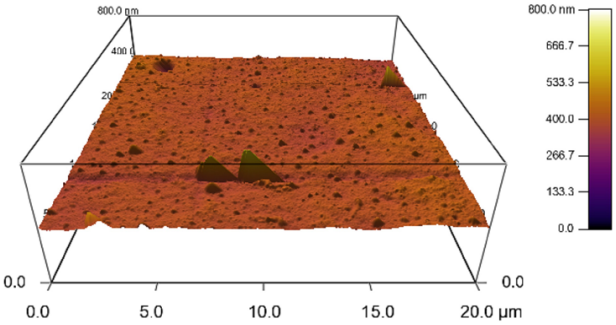
800.0 nm
666.7
533.3
400.0
266.7
133.3
0.0
0.0
0.0
0.0
5.0
10.0
15.0
20.0 µm

(C)

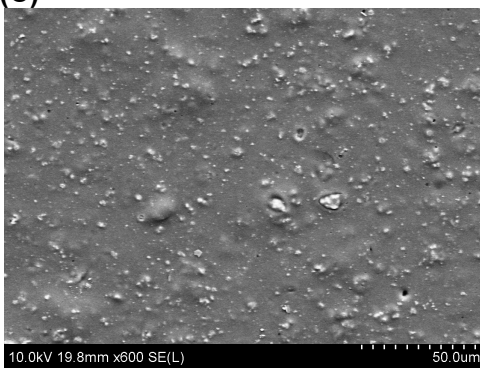
10.0kV 19.8mm x600 SE(L)
50.0um

(D)

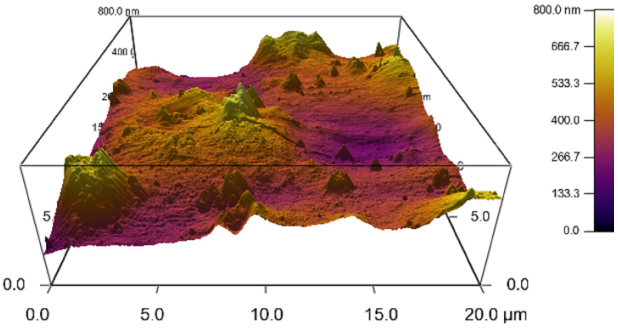
800.0 nm
666.7
533.3
400.0
266.7
133.3
0.0
0.0
0.0
5.0
10.0
15.0
20.0 µm

(E)

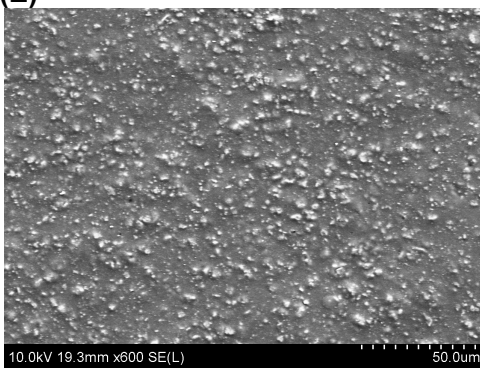
10.0kV 19.3mm x600 SE(L)
50.0um

(F)

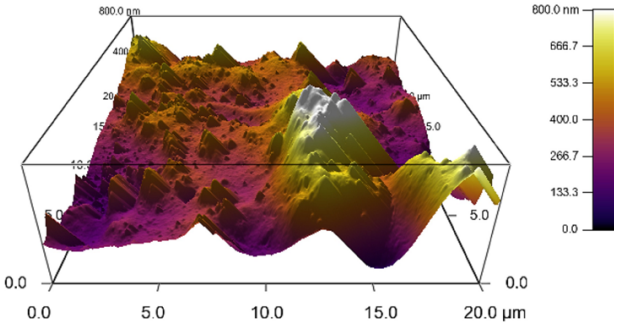
800.0 nm
666.7
533.3
400.0
266.7
133.3
0.0
0.0
0.0
5.0
10.0
15.0
20.0 µm

(G)

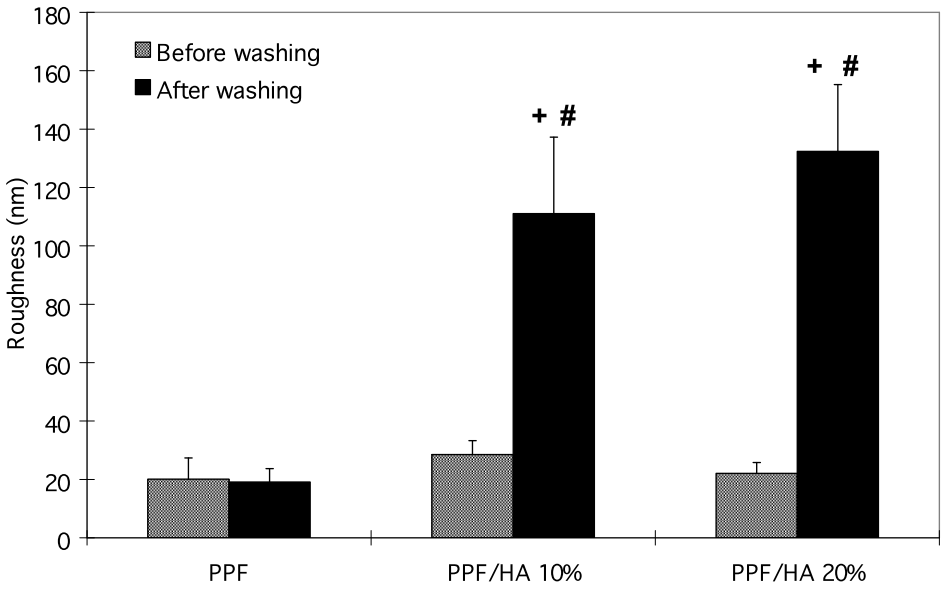

Figure 10: Surface morphology as observed by scanning electron microscopy (SEM) images of 2D disks with PPF (A), PPF/HA10% (C), and PPF/HA20% (E). All images were obtained with 600x magnification and the scale bar represents 50 μm. These qualitative results demonstrate that HA nanoparticles were homogeneously distributed over the surface of the 2D disks and more HA content was observed with increasing HA amount. Topographic images of the surfaces by atomic force microscope (AFM) with PPF (B), PPF/HA10% (D), and PPF/HA20% (F) demonstrated that rougher surface was obtained by increasing the amount of HA. Additionally, the root mean square (RMS) roughness after the acetone washing increased significantly by adding more HA nanoparticles while the values before the acetone washing were independent of HA particle amount. + indicates a significant difference between different HA amount groups after washing ($p<0.05$), and indicates a significant difference between before and after washing in scaffolds with the same composition ($p<0.05$).

	Element Percentages from EDS Spectrum Analysis			
Composition	**Carbon**	**Oxygen**	**Calcium**	**Phosphate**
PPF	56.04 ± 0.31%	43.15 ± 0.13%	0.76 ± 0.21%	0.05 ± 0.01%
PPF/HA 10%	53.74 ± 0.77%	42.21 ± 0.38%	3.10 ± 0.74%	0.95 ± 0.43%
PPF/HA 20%	50.64 ± 0.59%	42.05 ± 0.34%	5.49 ± 0.55%	1.82 ± 0.15%

Table 11: Percentage of elemental carbon (C), oxygen (O), calcium (Ca), and phosphate (P) on the nanocomposite surface as determined by EDS spectrum analysis.

amount of incorporated HA (Figure 13). The hydrophobic PPF control (Figure 13(A)) did not adsorb trypan blue while more dye was adsorbed in the PPF/HA 10% and 20% groups (Figure 13(B) and (C)). Similarly, the amount of protein adsorbed to the surface of the 3D scaffolds increased with the addition of more HA particles (Figure 13(D)). The PPF/HA 20% group showed a significantly higher protein adsorption compared to the PPF control group ($p = 3.76\times10^{-3}$). This result suggests that a higher level of HA incorporation resulted in increasing surface roughness and that a higher concentration of HA exposed on the surface might elevate the hydrophilicity and subsequent protein adsorption level. Along with the improved physical characteristics with increasing the amount of HA, the mechanical properties such as Young's modulus and yield strength of the 3D structures were also increased.

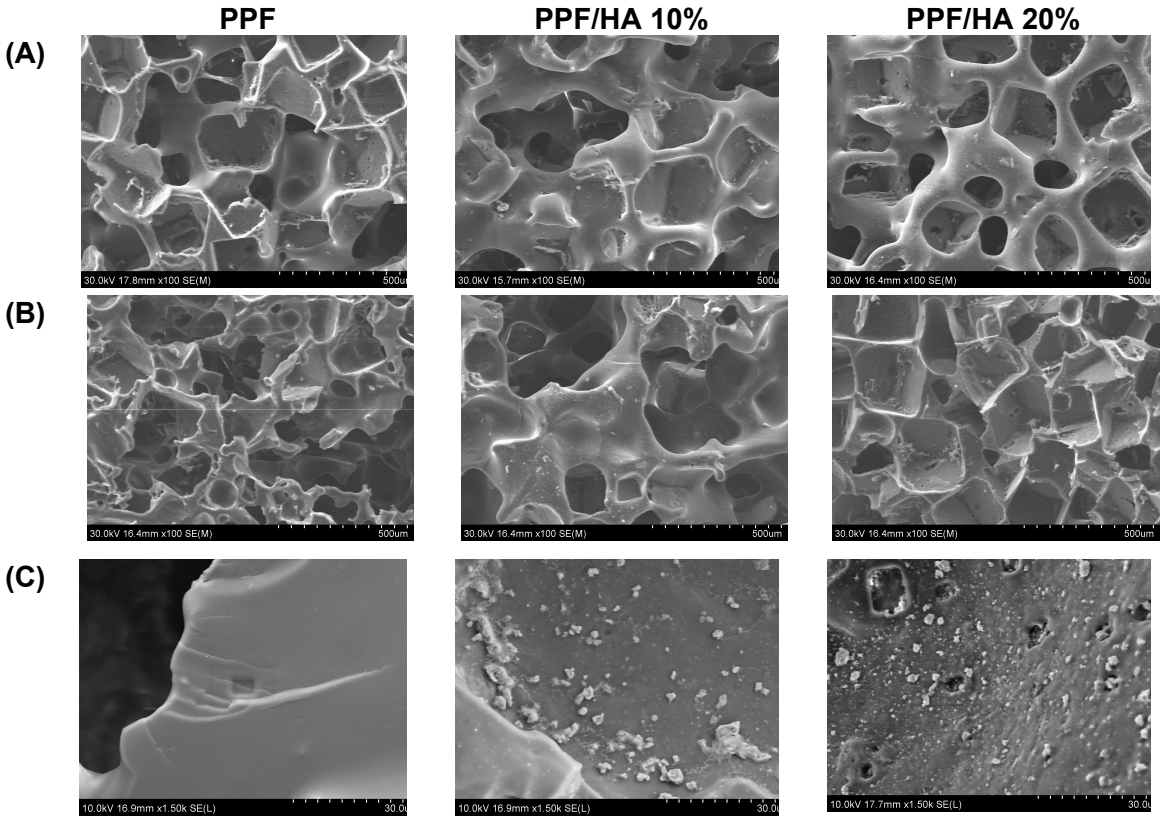

Figure 11: SEM structural images of the top surface (A), cross sections (B), and particle distribution (C) of 3D macroporous PPF and PPF/HA scaffolds by SEM. The scale represents 500 μm in (A) and (B), and 30 μm in (C). This qualitative result demonstrates that 3D macroporous scaffolds fabricated by simple salt leaching technique showed interconnective porous structures and more HA particles were seen on the surface as the HA amount included in fabrication increased.

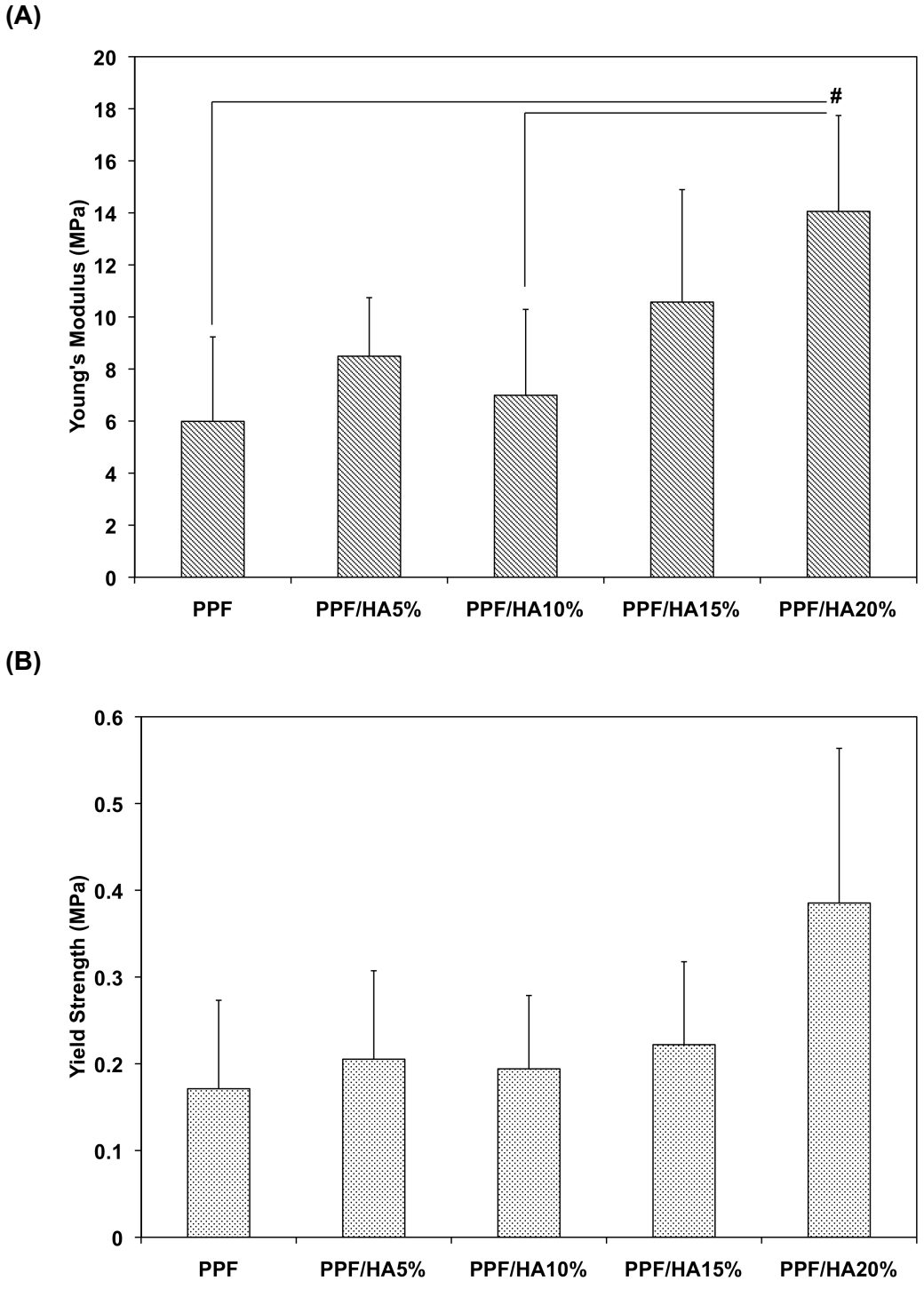

Figure 12: Compressive properties, including Young's modulus (A) and off-set yield strength (B), of 3D macroporous PPF and PPF/HA scaffolds. The result demonstrated that the PPF/HA 20% group showed significantly higher Young's modulus than the PPF control and PPF/HA 10% groups. Off-set yield strength in the PPF/HA 20% group was also higher than in the other groups. # indicates a significant difference between groups ($p<0.05$).

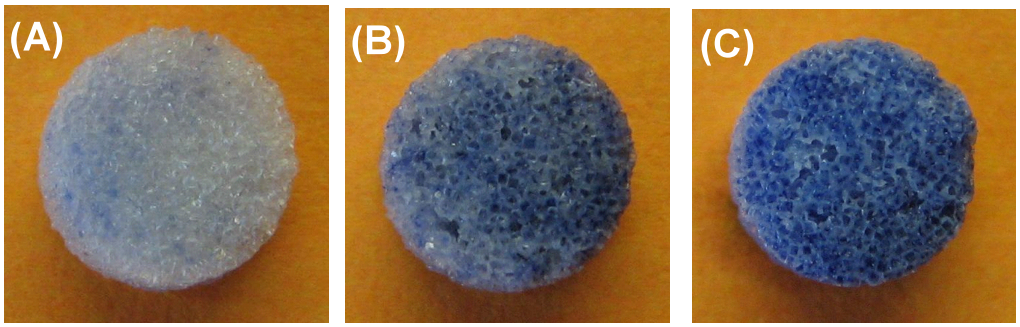

(D)

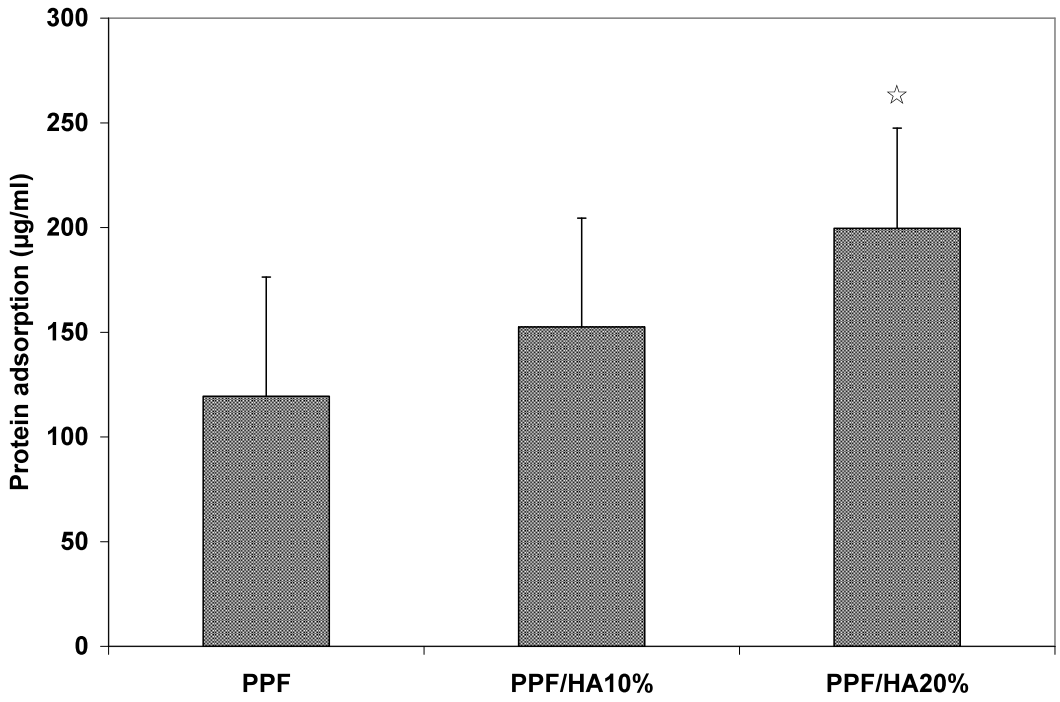

Figure 13: HA particle distribution over the surface of scaffolds was assessed by trypan blue staining with PPF (A), PPF/HA10% (B), and PPF/HA20% (C). Protein adsorption on the PPF/HA composite scaffolds with different concentration of HA nanoparticle is shown in (D). ☆ indicates a significant difference compared to the PPF control group ($p<0.05$).

5.3.3. BMSC characterization by flow cytometry

The mesenchymal stem cell population in a heterogenous bone marrow stromal cell sample can be characterized by cell surface marker staining. In particular, MSCs are thought to be positive for CD29 and CD90, while negative for CD34 and CD45 [282, 283]. Results showed that freshly harvested BMSCs are a heterogeneous cell population including leukocytes, monocytes, and granulocytes. Bone marrow aspirate contained 86.7% of CD45(+) cells, but this percentage fell to 17.0% after three passages (Table 12). The percentage of CD29(+) and CD90(+) cells increased after 3 passages (92.1 to 100 % and 76.4 to 80.1 %, respectively). The percentage of the total mesenchymal stem cell population, defined here as CD29(+), CD90(+), CD34(-), and CD45(-), was only 0.1% for freshly harvested BMSCs, however it was 49.6% for subcultured cells. As shown in Figure 14, it is concluded that a subculture procedure is suitable for expanding rat MSC populations from primary bone marrow stromal cells.

	Cell Population Composition	
Cell Surface Markers	**Fresh Bone Marrow Cells**	**Passage 3 Cells**
CD34	0.4%	1.1%
CD45	86.7%	17.0%
CD29	92.1%	100.0%
CD90	76.4%	80.1%
CD34-/CD45-/CD29+/CD90+	0.1%	49.6%

Table 12: FACS characterization of the mesenchymal stem cell population (as defined by CD29(+)/CD90(+)/CD34(-)/CD45(-)) of fresh bone marrow stromal cells and those cells after three passages.

(A)

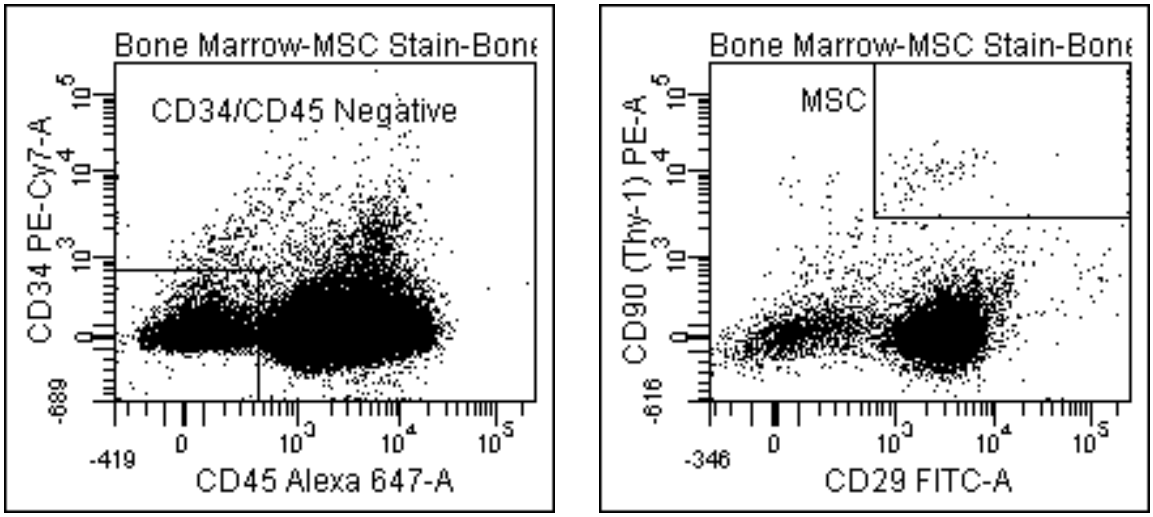

(B)

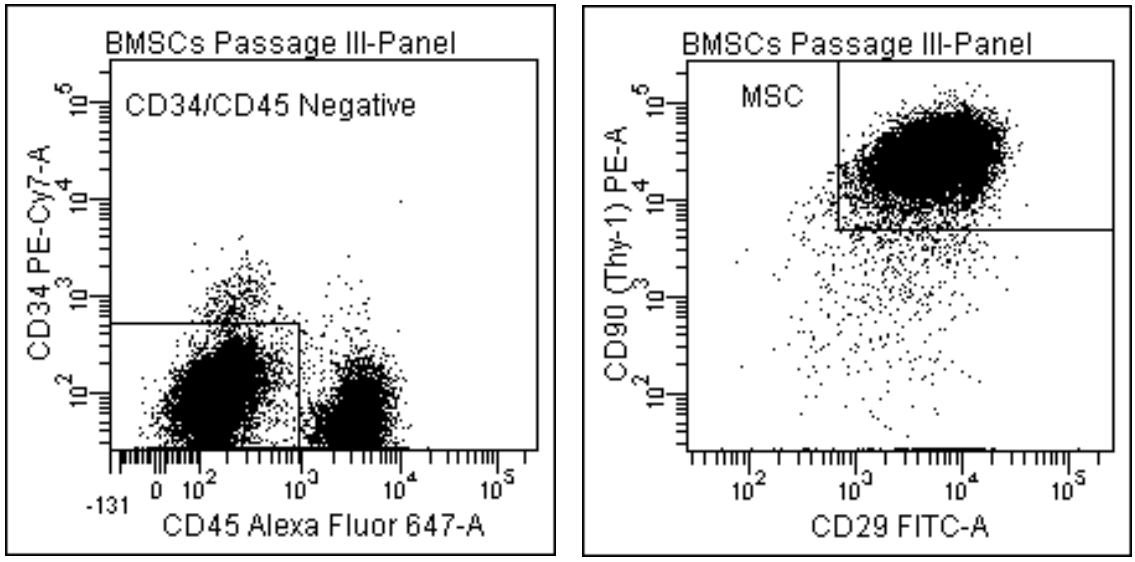

Figure 14: Flow cytometry analysis of freshly derived BMSCs from rats (A) and subcultured cells after three passages (B). Approximately 50% of the BMSCs presented MSC markers (CD29(+)/CD90(+)/CD34(-)/CD45(-)) after three passages.

5.3.4. Cell attachment

As measured by fluorescently stained cell-area, the qualitative images of Calcein AM staining in Figure 15(A) reveals that more cells are attached to the composite scaffolds as HA concentration increases. For quantification (Figure 15(B)), the total cell-attached area in each group was normalized by that of the TCPS control. The percent attachment in the PPF/HA 20% group was significantly higher than the other groups ($p = 2.05\times10^{-4}$). Rat BMSC attachment was increased with increasing surface roughness which in turn depended on HA particle concentration in these composite scaffolds. These results demonstrated that increased HA particle incorporation in PPF scaffolds increased surface roughness, subsequent protein adsorption from the media to the surface of the composite, and resulted in more cells favorably attaching to the composite scaffold surface.

5.3.5. Viability, cytoskeleton development, and cellular morphology

To characterize rat BMSC viability on 3D porous PPF/HA scaffolds, Calcein AM staining was performed (Figure 16(A)). The cytoskeleton development of cells was examined by F-actin staining (Figure 16(B)) while cellular morphology was observed by SEM (Figure 16(C)). Calcein AM staining data demonstrated that the cells in all experimental groups were viable for up to 8 days of in vitro culture in OS-conditioned media. Along with 2D attachment data on day 1 (Figure 15(A)), PPF and PPF/HA composite materials supported a suitable environment for rat BMSCs in the 3D scaffolds. Images of F-actin staining qualitatively demonstrated that more cytoskeleton development occurred in PPF/HA 20% groups than the PPF control

(A)

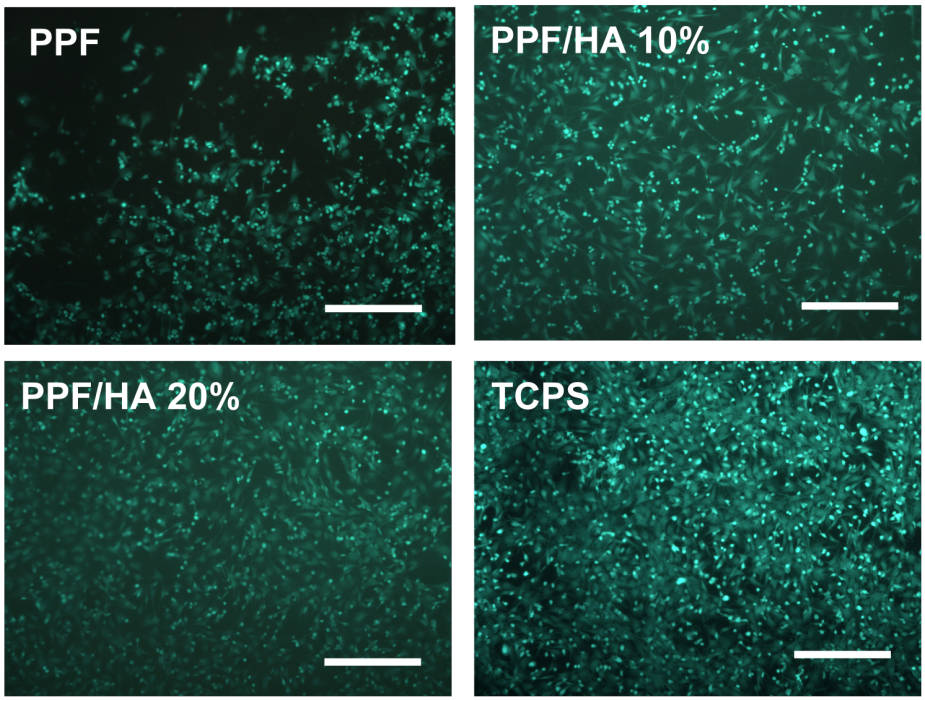

(B)

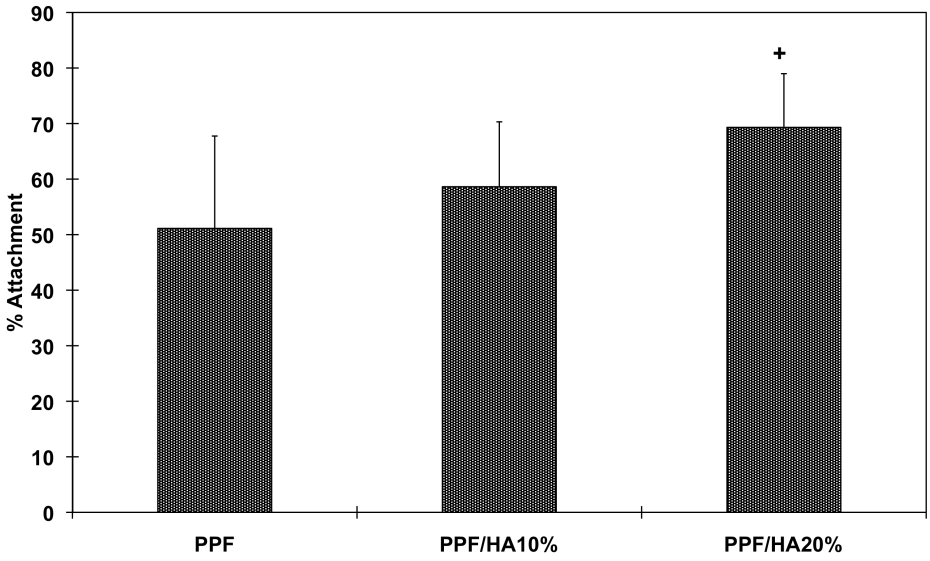

Figure 15: Live/dead fluorescent staining images of initially attached cells on 2D disks (A) and percent attachment pattern compared to a TCPS positive control sample (B). The result in (A) qualitatively demonstrated that more viable rat BMSCs were observed in composite disks with higher amount of HA and the result in (B) verified that the percent attachment in the PPF/HA 20% group was significantly higher than in the other groups. + indicates a significant difference between groups ($p<0.05$).

(A)

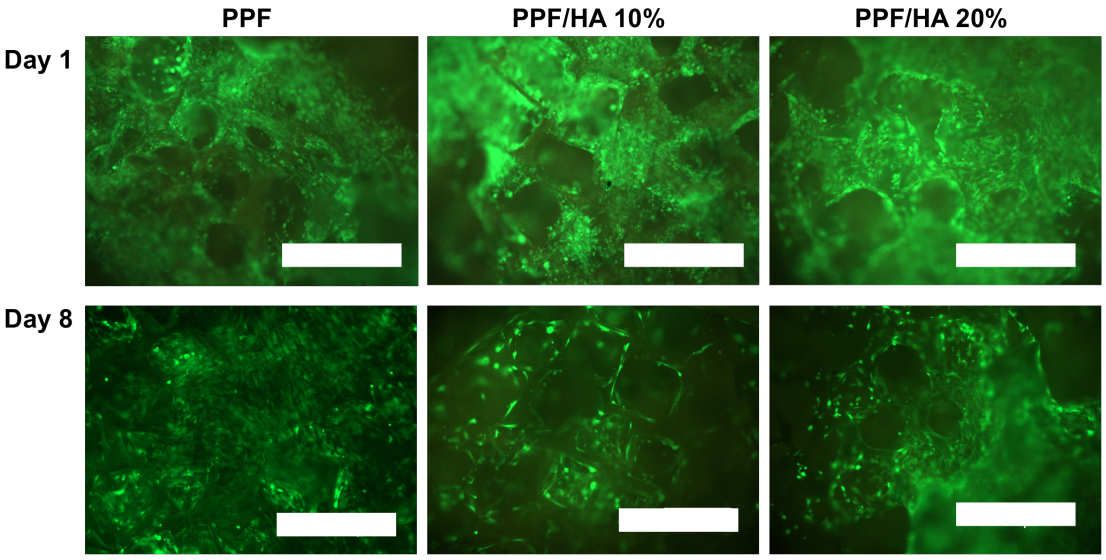
PPF
PPF/HA 10%
PPF/HA 20%
Day 1
Day 8

(B)

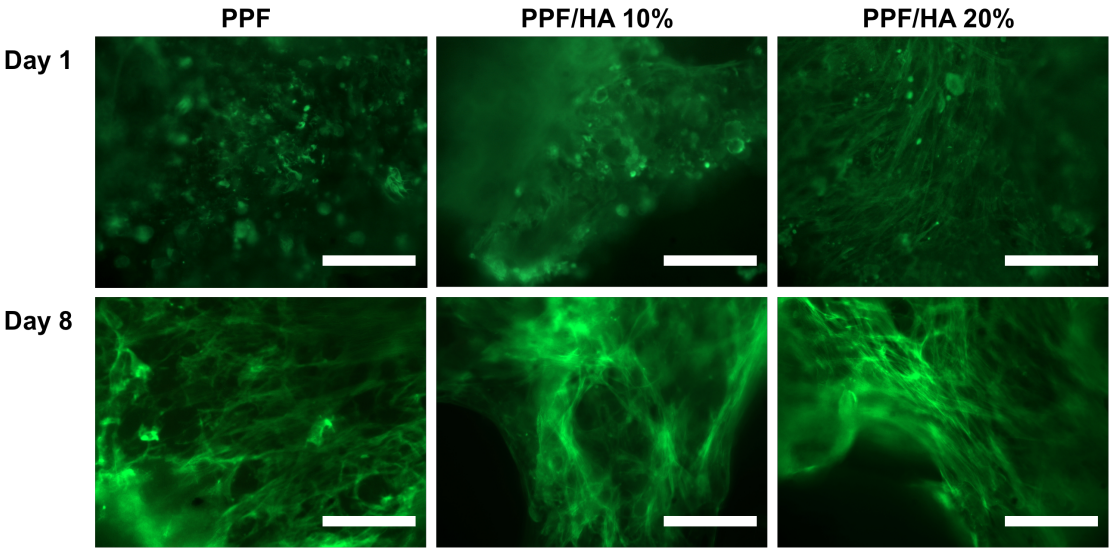
PPF
PPF/HA 10%
PPF/HA 20%
Day 1
Day 8

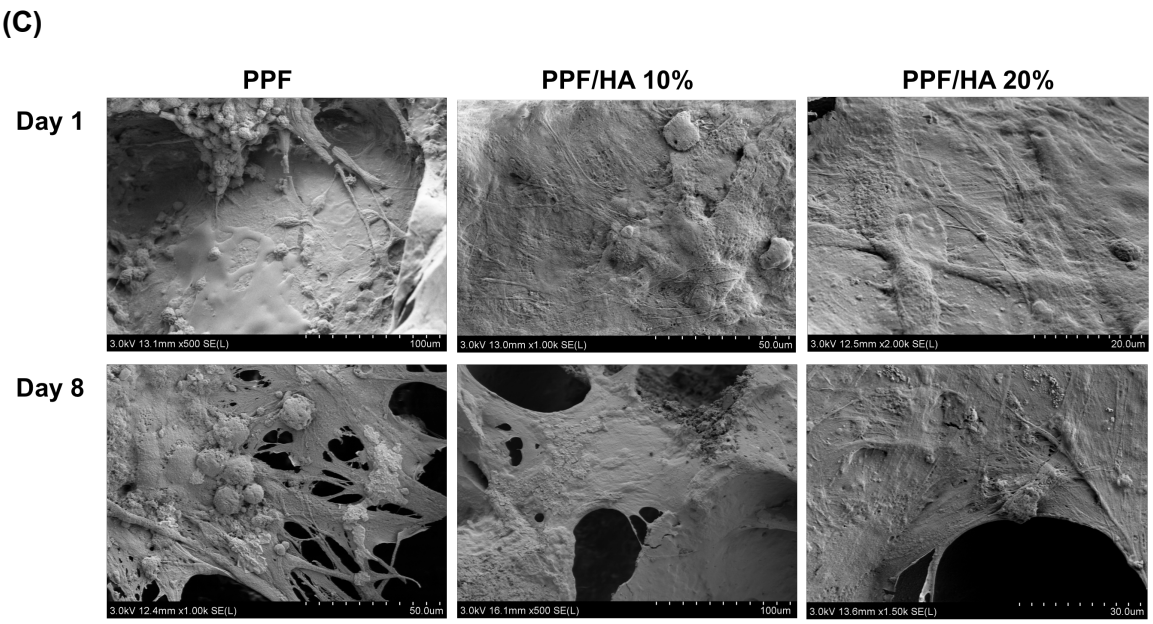

Figure 16: Visualization of viability by Calcein AM fluorescent staining (A), cytoskeleton development (B), and cellular morphology by SEM (C) onto PPF composite scaffolds with different HA nanoparticle amount. The scale bar represents 300 μm in (A) and 100 μm in (B).

group on day 1, however all groups showed similar levels of cytoskeleton development on day 8 (Figure 16(B)). This result is also correlated with the change of cellular morphology observed by SEM on day 1, where observable cell flattening was seen on the surface of the PPF/HA 20% groups, while some of cells on control PPF retained a rounded shape (Figure 16(C)). On day 8, the cells on PPF/HA composite scaffolds were highly flattened and covered the surface of these scaffolds.

5.3.6. Osteogenic signal expression profiles

Quantitative RT-PCR was performed to investigate the effect of HA nanoparticle incorporation with various seeding densities on osteogenic signal expression. For higher seeding density groups, BMP-2 gene expression generally

decreased or was stagnant for all HA amount groups (Figure 17(A)). However, the addition of HA along with high cell seeding density increased BMP-2 expression compared to the PPF control on day 8 ($p = 9.83\times10^{-6}$). This observation was similar to the low cell seeding groups: PPF control group with low cell seeding showed decreasing BMP-2 expression over 8 days while 10 Low and 20 Low groups exhibited significantly higher expression level than PPF control on day 8 ($p = 2.96\times10^{-8}$), and this level was also significantly higher than 10 High and 20 High groups ($p = 4.38\times10^{-5}$ and $p = 1.46\times10^{-5}$, respectively). Increased HA incorporation in the low cell seeding density groups (10 Low and 20 Low) was also observed to be correlated with increased BMP-2 expression after 8 days of culture over the initial expression level on day 1.

FGF-2 expression represents a similar pattern to the TGF-β1 expression profile (Figure 17(B) and 17(C)). Among high cell seeding density groups, 20 High exhibited 3 fold up-regulation of FGF-2 on day 4 and kept this level until day 8 ($p = 3.81\times10^{-4}$). Moreover, 10 High also showed a 2.95 fold up-regulated FGF-2 expression on day 8 and both 10 High and 20 High exhibited significantly higher FGF-2 expression than the PPF control group on day 8 ($p = 6.94\times10^{-3}$). A similar up-regulation pattern was also observed in the low cell seeding density groups on day 8: FGF-2 expressions of both 10 Low and 20 Low were significantly higher than 0 Low on day 8 ($p = 1.03\times10^{-8}$) and this level was also up-regulated over the day 1 expression level. Specifically, 20 Low exhibited more than a 4.7 fold change compared to the calibrator group. A general decreasing trend of TGF-β1 expression

was also observed in the PPF control groups for both cell seeding density groups over 8 days.

(A)

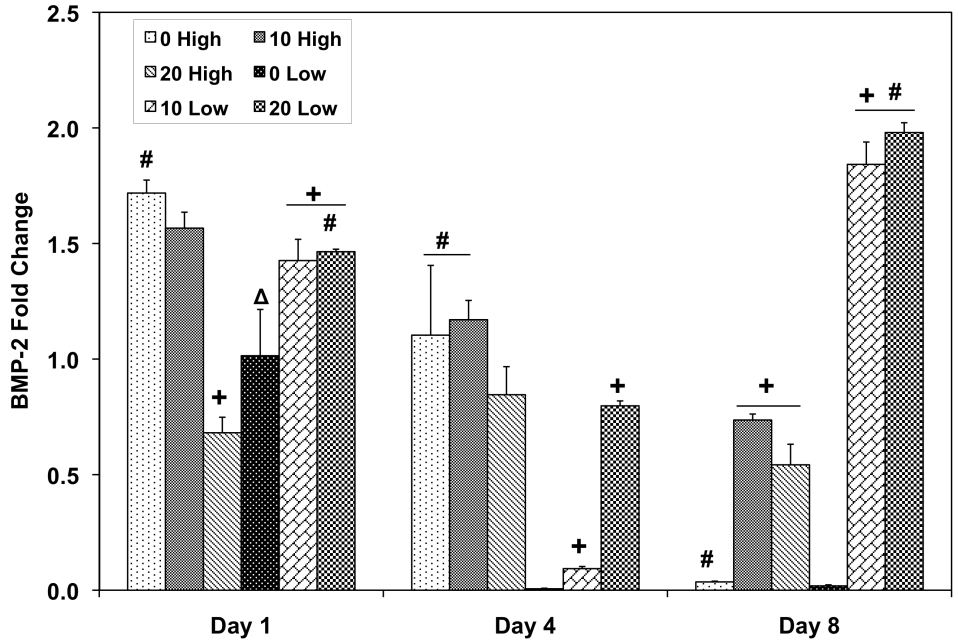

(B)

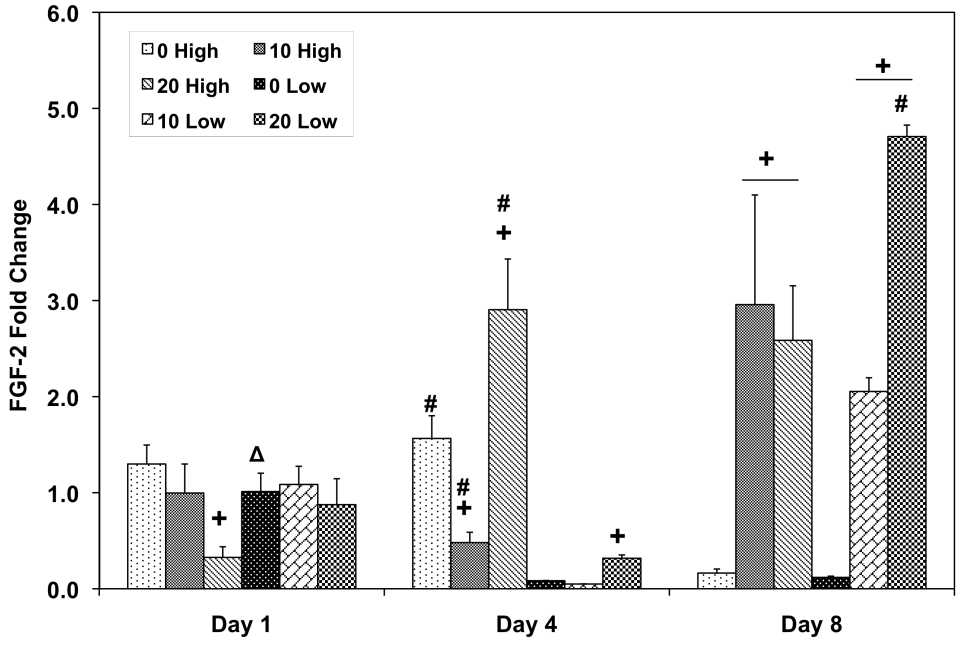

(C)

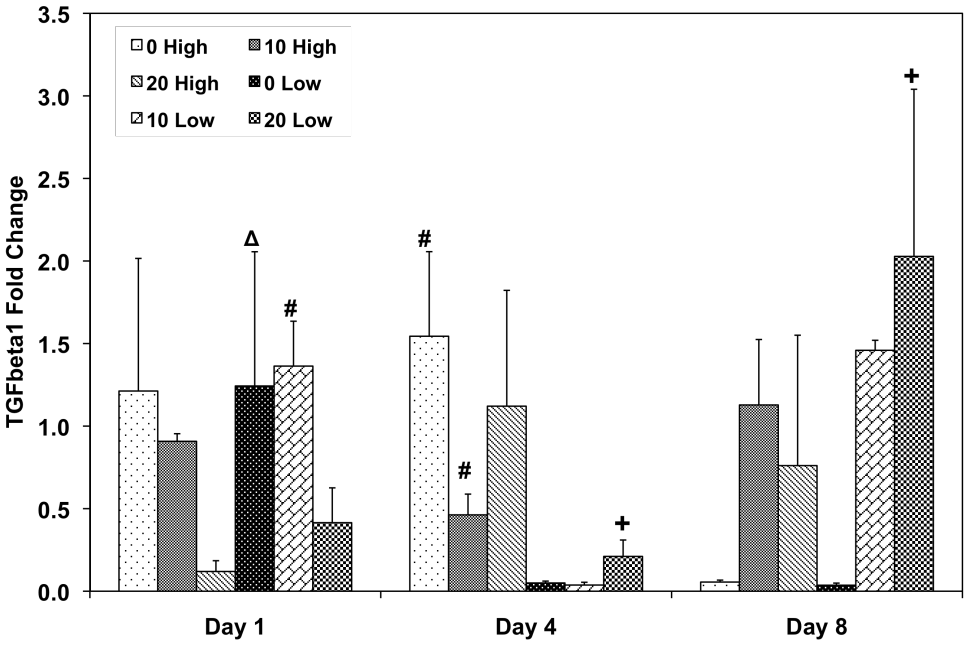

(D)

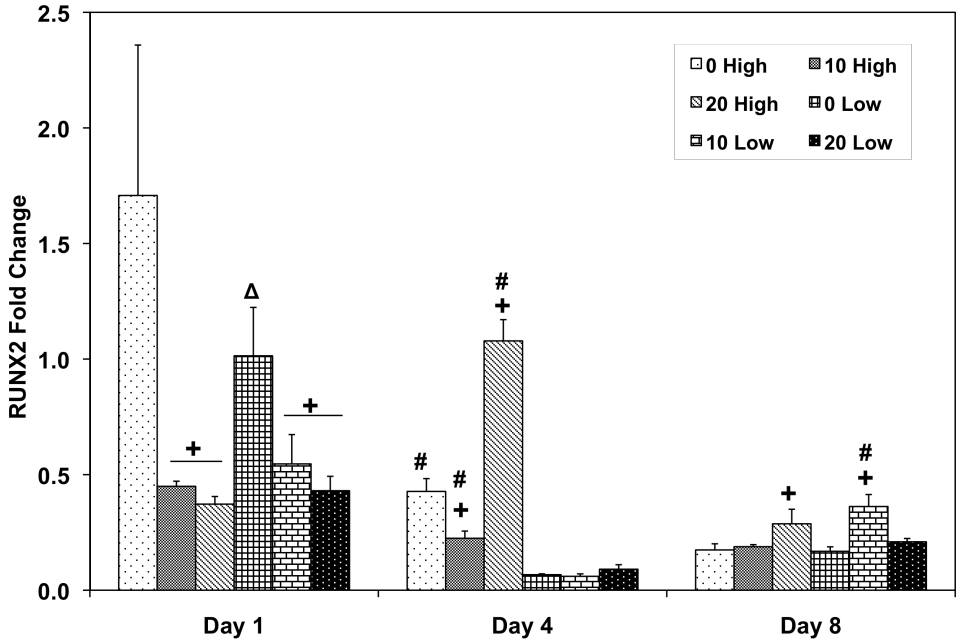

Figure 17: Quantitative RT-PCR analysis of gene expression profiles of growth factors (A: BMP-2, B: FGF-2, C: TFG- β1, and D: Runx2) for 1, 4, and 8 days. The fold changes in gene expression level are reported as average ± standard deviation (n=3) and the calibrator for all experimental groups is indicated by a Δ marker. + indicates a statistical difference in HA amount within the same cell seeding density group as compared to the 0% HA control group while # indicates a statistical difference in cell seeding density groups within the same HA concentration group.

For the higher cell seeding density groups, HA addition induced more TGF-β1 expression than in the PPF control, but this level was below than the expression of the calibrator group on day 1. A significant increase of TGF-β1 was found in 20 Low group on day 8 versus 0 Low and 10 Low groups ($p = 1.48\times10^{-2}$), and this up-regulation was more than a 2 fold increase compared to the calibrator group.

The Runx2 transcription factor expression in the high cell seeding density groups showed a decreasing pattern over 8 days except 20 High group, which showed a peak on day 4 (Figure 17(D)). All groups with low cell seeding density exhibited down-regulation of Runx2 expression on day 4 and an increased expression by day 8.

5.3.7. Osteoblastic differentiation

In order to investigate whether the cell population would differentiate into an osteoblastic lineage by changing the HA amount in the scaffolds, and/or the initial cell seeding density, ALP protein activity was assessed (Figure 18). A correspondence between ALP activity and the HA particle amount was only observed in lower cell seeding density groups on day 1 and a higher cell seeding group (20 High) on day 4, compared to the PPF control group. During the later time points, 0 Low group on day 4 ($p = 8.01\times10^{-4}$) and both 0 Low and 10 Low groups on day 8 ($p = 1.01\times10^{-2}$ and 4.31×10^{-3}, respectively) exhibited significantly higher ALP activity compared to higher cell seeding density groups. Late osteoblastic differentiation was assessed by calcium deposition (Figure 19) and the OC mRNA expression (Figure 20). Increasing HA content in both cell seeding density groups resulted in higher mineralization. On day 8, 20 High group showed significantly higher calcium

deposition than the PPF control group and both 10 and 20 Low groups also showed significantly higher mineral contents ($p = 6.62\times10^{-6}$). On day 15, 20 High group at both cell seeding densities showed significantly increased calcium deposition over the PPF control group ($p = 4.53\times10^{-4}$). Moreover, 10 and 20 Low groups presented a significant increase in mineralization versus the high cell density groups on day 8 while mineralization on day 15 was statistically unchanged when cell seeding density was varied. In Figure 20, it can be seen that the OC mRNA expression in all groups exhibited an increasing trend over 8 days. By day 4, 20 High group exhibited a significantly higher OC expression level than did the other groups. On day 8, the expression level of HA incorporated PPF groups was higher than the PPF control group for both cell seeding densities ($p = 3.08\times10^{-5}$). Although the effect of cell seeding density on OC expression was not observed on day 8, the effect of HA amount on the expression (i.e., increased osteoblastic differentiation with higher HA concentration) was correlated with calcium deposition, as seen in Figure 19.

5.4. Discussion

The main objective of this study was to determine which 3D PPF/HA nanoparticle composite scaffold parameters facilitate osteoblastic differentiation and endogenous osteogenic signal expressions. In order to optimize the construct properties that mimic the native bone healing process, controlling parameters that enhance the expression of signaling molecules such as the physical properties of the scaffold and intercellular signaling distance were characterized. It appears that the

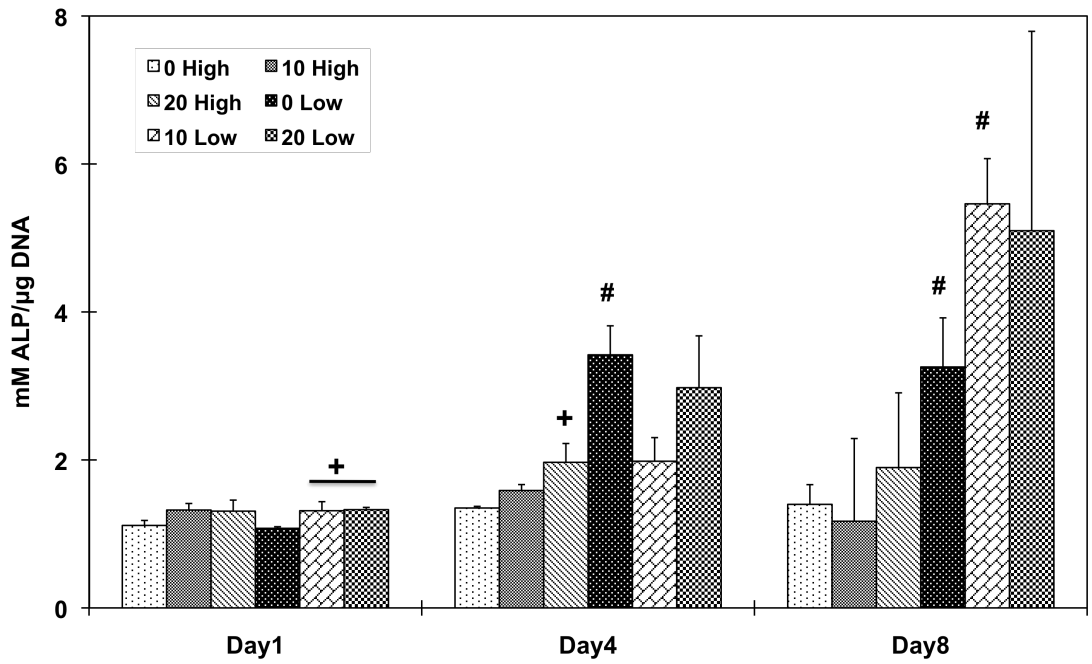

Figure 18: ALP protein activity of rat BMSCs on PPF composite scaffolds with different HA contents and cell seeding densities for 1, 4, and 8 days. ALP protein expression level was normalized by DNA amount and average ± standard deviation (n=3 per group) is reported. + indicates a statistical difference in HA amount within the same cell seeding density group while # indicates a statistical difference in cell seeding density groups with the same HA concentration group ($p<0.05$).

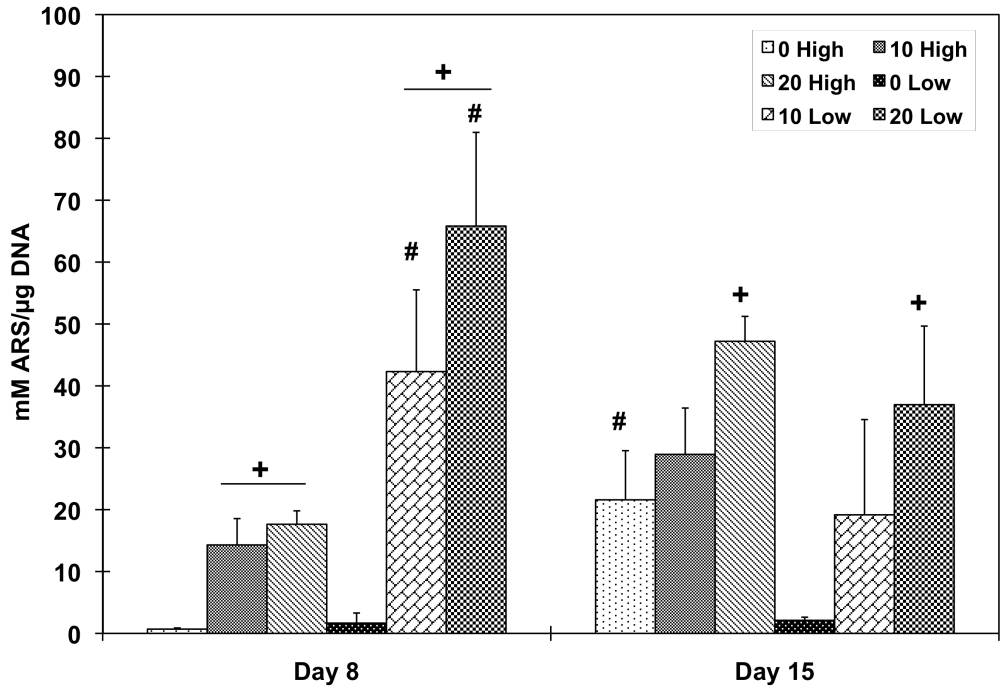

Figure 19: Quantitative mineralization assay by alizarin red S staining on day 8 and 15. Calcium deposition level was normalized by DNA amount and average ± standard deviation (n=3 per group) is reported. + indicates a statistical difference in HA amount within same cell seeding density group while # indicates a statistical difference in cell seeding density groups with the same HA concentration group ($p<0.05$).

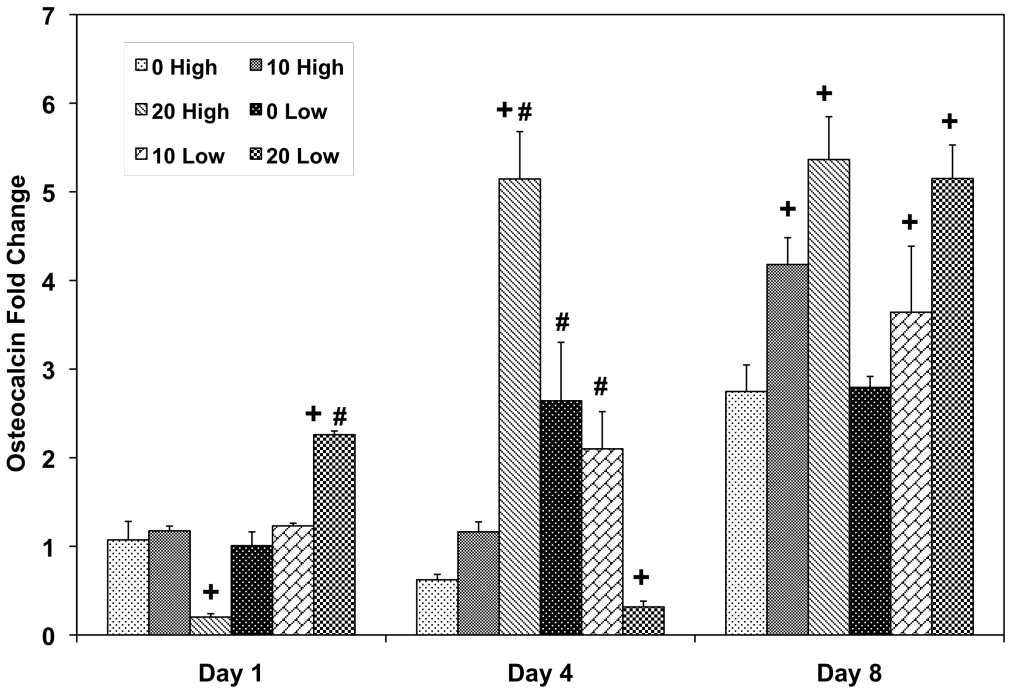

Figure 20: Quantitative RT-PCR analysis of gene expression profiles of OC osteogenic differentiation markers for 1, 4, and 8 days. The fold changes in gene expression level are reported as average ± standard deviation (n=3) and the calibrator for all experimental groups is indicated by a Δ marker. + indicates a statistical difference in HA amount within the same cell seeding density group as compared to the 0% HA control group while # indicates a statistical difference in cell seeding density groups within the same HA concentration group ($p<0.05$).

incorporation of HA nanoparticles into PPF resulted in an alteration of surface properties of these composite materials including topography, roughness, calcium and phosphate atomic ratio, and ability to adsorb proteins. In addition, changing initial cell seeding density altered cell-cell paracrine signaling distance among the transplanted cell population. Therefore, it is of importance to characterize the proper conditions of those parameters that control or at least facilitate the stimulation of specific osteogenic growth factor expression. To this end, we aim to investigate both the effect of the amount of HA incorporated in PPF scaffolds and the initial cell seeding density on endogenous osteogenic growth factor gene expression profiles and osteoblastic differentiation.

We fabricated well-interconnected 3D macroporous PPF/HA scaffolds via simple techniques using porogen leaching and photocrosslinking. The characterization data in Figure 10 demonstrates that HA nanoparticle incorporation resulted in uniform distribution of HA and higher level of calcium and phosphate on the surface of composites. Moreover, HA incorporated composite scaffolds exhibited rougher surface topography as confirmed by RMS roughness data. Subsequently, surface properties modified by HA nanoparticle incorporation also resulted in higher levels of passive protein adsorption onto the scaffold surface and higher hydrophilicity (i.e., wettability) of scaffolds (Figure 13). Both of these factors may improve initial cell attachment since higher roughness provides more surface area with more complex geometry for cells to attach to, and increasing hydrophilicity is directly related with the adsorption of proteins existing in the aqueous media [268]. This present study also verified this relation by showing that higher rat BMSC

attachment was observed in PPF/HA 20% composite than in control PPF samples in a 2D environment (Figure 15). In addition, qualitative visualization of cells on 3D PPF/HA composite scaffolds also demonstrated more cytoskeleton development on PPF/HA 20% scaffolds than on PPF control scaffolds on day 1 as assessed by F-actin staining (Figure 16(B)). The SEM images also qualitatively demonstrated morphological changes in cell flattening with more cell flattening observed as HA incorporation in composite scaffolds was increased (Figure 16(C)). This result may be explained by HA nanoparticles potentially playing a functional role in the integrin-mediated cell adhesion. Generally, initial cell adhesion to extracellular matrix (ECM) is mediated by an integrin transmembrane receptor [284]. Integrin binding to ECM proteins physically connects the cell's cytoskeleton and the surrounding ECM. This initiates the intracellular signaling pathway to nucleate the signaling proteins such as focal adhesion kinase. For example, controlled HA deposition has been observed to induce MC3T3-E1 cell adhesion, integrin presentation and clustering, and focal adhesion complex mediation[285]. Since the integrin binding and initial cell attachment play a critical role in downstream signaling cascades such as the interaction of cytoskeleton protein/cellular membrane protein/ECM proteins, induction of signal transduction, stimulation of transcription factors, and consequent gene expression [286, 287], HA nanoparticle incorporation may stimulate not only initial cell adhesion but also osteogenic growth factor gene expressions during osteoblastic differentiation.

The compressive Young's modulus and off-set yield strength of PPF/HA composite scaffolds were determined in order to investigate scaffold's load-bearing

capacity and its potential as a bone substitute (Figure 12). The compressive modulus of the 3D PPF/HA composite scaffolds exhibited similar levels to that of native human cancellous bone (i.e., 2 to 10 MPa) [288]. The PPF/HA 20% group exhibited significantly higher Young's modulus than the PPF control and PPF/HA 10% groups. Composite scaffolds presented a trend of increasing Young's modulus relative to HA nanoparticle reinforcement, and this has been observed in other studies. For example, polycarbonate/HA nanoparticle composite scaffolds exhibited an increase of Young's modulus from 0.6 GPa to 4.5 GPa when the amount of HA was increased from 10% to 30% [289]. Similarly, PLG/HA composite also showed an increase in Young's modulus when the ratio of PLG:HA was increased up to 1:5 [281]. One possible explanation of observed mechanical enhancement could be the intrinsic contribution of HA as well as an increase in surface to volume ratio with HA nanoparticle addition, which also found in PCL/HA composites [290]. Therefore, the mechanical properties of photocrosslinked porous PPF/HA nanocomposite scaffolds observed in this study demonstrated that these properties can be controlled during fabrication, a possibly useful fact for manufacturing bone tissue engineering scaffolds.

The effect of HA amount on endogenous osteogenic gene expression in composite scaffolds with varying cell seeding density was investigated. There have been many studies about the effect of exogenous growth factors on osteoblastic differentiation; however, the present research has shown for the first time the effect of HA presence on endogenous osteogenic gene expression including BMP-2, FGF-2, TGF-β1, and Runx2. BMP-2 is known to participate in the regulation of cell growth and differentiation along with the induction of osteogenic progenitor cells in bone

defect sites during the healing process. Although there have been many studies on exogenous BMP-2 administration to culture media as well as delivery of this growth factor to the healing defect site, the present study demonstrated that endogenous osteogenic signal expressions could be facilitated by altering scaffold construction properties of cell/scaffold integration through the incorporation of HA nanoparticles and changing the initial cell seeding density. Despite of the fact that BMP-2 gene expression level was decreased or was unchanging for PPF control scaffolds, the HA incorporated composite scaffolds induced significantly higher BMP-2 expression than the control on day 8 ($p = 9.83\times10^{-6}$ in high cell seeding and 2.96×10^{-8} in low cell seeding). This HA-induced BMP-2 upregulation was observed for both cell seeding densities (Figure 17(A)). The upregulated level of BMP-2 expression was higher in the lower cell seeding density on day 8. Therefore, it seems that PPF/HA composite scaffolds may stimulate higher endogenous BMP-2 expression and its expression level may be also be responsive to the initial cell seeding density.

We have previously speculated on the interaction of endogenous signal expression with other signaling factors of rat BMSCs cultured on 2D PPF disks previously [273]. BMP-2 signaling is dependent on the expression of Runx2 transcription factor through the Smad and MAPK intracellular signaling pathways [16, 291], and our comparison with BMP-2 and Runx2 expression profiles in this study might confirm this interaction. Early decline of BMP-2 in all groups except the 20 High group in a 3D scaffold by day 4 was also associated with Runx2 deactivation as seen in Figure 17(D). Specifically, an increase in BMP-2 expression in the 20 High group by day 4 might be related to increasing Runx2 expression by day 4. For

later time points, from day 4 to 8, the high cell seeding density groups exhibited a general decline of BMP-2 expression although HA incorporation resulted in different levels of expression on day 8 and Runx2 expression profile in high cell seeding groups showed the same decreasing pattern by day 8. During this period, low cell seeding groups exhibited increasing BMP-2 expression that might be also related to an increase in Runx2 expression in all HA incorporated groups. Moreover, Runx2-mediated growth factor gene expression was also observed in FGF-2 expression (Figure 17(B)), which is also associated with Runx2 induction via the MAPK pathway [292]. For the low cell seeding density groups, the decreasing trend of FGF-2 expression from day 4 to 8 is correlated with a decrease in the Runx2 expression pattern. However, a discrepancy in the high cell seeding density groups was observed, which is that up-regulation of FGF-2 expression in 10 and 20 High groups during the later time points was not related to the down-regulation of Runx2 in the same groups. This might be explained by the possibility that Runx2 stimulation was more affected by BMP-2 stimulation via both the Smad and MAPK pathways, rather than FGF-2 expression through the MAPK pathway. Therefore, the decline of BMP-2 in high cell seeding groups on day 8 might correlate with Runx2 down-regulation, even in the presence of FGF-2 up-regulation.

FGF-2 is associated with the stimulation of osteoblast through the Cbfa-1/Runx2 transcription factor activation [18] as well as angiogenic development [293]. Therefore it is imperative to investigate its signaling profiles to promote the integration of implanted scaffolds with surrounding host tissues for bone tissue regeneration. In the FGF-2 expression profile in Figure 17(B), it was observed that

its expression increased at a later time point of day 8 and that the HA addition in composite scaffolds may have facilitated statistically higher FGF-2 expression that was not observed in the PPF control group. The PPF/HA 10% and 20% groups exhibited higher FGF-2 expression level than did the PPF control on day 8 for both cell seeding densities. In particular, 20% HA nanoparticle addition to composite with 0.33 million cell seeding showed up to a 5 fold change by day 8. This observation of upregulated osteogenic signal expression with HA nanoparticle incorporation was correlated with BMP-2 expression and could be evidence of an effect on osteogenic signal expression by altering scaffold construction properties. The results in Figure 17(D) also demonstrated that HA incorporation into composite scaffolds at both cell seeding densities enhanced the TGF-β1 expression on day 8 from both cell seeding densities, as was the case with FGF-2 expression. Our previous study demonstrated that the existence of optimal cell seeding density of transplanted rat BMSC populations on 2D PPF disks appeared to facilitate BMP-2, FGF-2, and TGF-β1expression [273]. This present study using 3D PPF/HA porous scaffolds also demonstrated that the optimum condition to induce more osteogenic signal expression was the PPF/HA 20% group with 0.33 million cells.

The effect of HA nanoparticle contents on the osteoblastic differentiation of rat BMSCs was investigated with two different cell seeding densities. ALP protein expression was examined as a transient early osteoblastic differentiation marker, while calcium deposition and OC mRNA expression was assessed as an indicator of a later stage of differentiation. The ALP expression level depended on the amount of HA nanoparticles incorporated into the scaffolds. This was a statistically significant

parameter in lower cell seeding density groups on day 8 (Figure 18). In addition, the results also demonstrated that mineralization and OC mRNA expression also depended on HA addition to the scaffolds (Figure 19 and 20). Both HA incorporated composite scaffolds exhibited significantly higher calcium deposition with both cell seeding densities on day 8 ($p = 6.50\times10^{-4}$ in high cell seeding and 1.48×10^{-3} in low cell seeding) and the effect of HA amount on mineralization was greater in the lower cell seeding density groups. The PPF/HA 20% groups showed higher levels of mineralization for both cell seeding densities on day 15. Similarly, the OC mRNA expression data also showed the dependence of late osteoblastic differentiation of BMSCs on the amount of HA present. Significantly higher OC expression was observed when HA concentration increased on day 8 even though an effect of cell seeding densities was not observed. The potential dependence of osteoblastic differentiation on incorporated HA amount is in agreement with several other studies. One of these recent studies showed that the incorporation of 50 ng of HA nanoparticles into cyclic acetal hydrogels stimulated more endogenous ALP mRNA expression of encapsulated rat BMSCs than 5 ng and control hydrogel groups on day 8. In the same study, OC mRNA expression in 5 and 50 ng of HA groups was significantly higher than the control on day 1, 4, and 8 [271]. OC and osteopontin (OP) mRNA expression of rabbit BMSCs in a 2D monolayer has also been observed to be dependent on HA nanoparticle concentration [294]. Moreover, osteoblastic differentiation with HA dependence has also been observed in human MCSCs on PLG/HA composite scaffolds and both ALP and OP protein expression levels were higher by increasing the HA:PLG ratio for up to 28 days [281]. Therefore, our

PPF/HA composite scaffold may also facilitate osteoblastic differentiation of transplanted rat BMSCs by increasing the amount of incorporated HA amount and by varying the initial cell seeding density.

5.5. Conclusions

This investigation of scaffold construction properties for 3D macroporous PPF/HA scaffolds appears to have found parameters that facilitate osteoblastic differentiation of transplanted cell populations and evidence of associated osteogenic signal gene expression that suggests these conditions might induce further bone regeneration as well as facilitate integration of scaffolds with the surrounding host tissues. This study revealed that altering both the level of HA nanoparticle incorporation and the initial cell seeding density can effect osteoblastic differentiation and growth factor gene expression. Our results demonstrated that (1) HA addition improved surface properties of composite scaffolds by showing increased roughness, hydrophilicity, protein adsorption, and initial cell attachment, (2) up-regulation of osteogenic signal expression was also controlled by both HA amount and initial cell seeding density, and (3) subsequent osteoblastic differentiation of rat BMSCs on 3D scaffolds was facilitated by the incorporation of HA and lower cell seeding density.

Chapter 6: Optimization of Scaffold Design Parameters to Induce Osteogenic Signal Expressions in 3D Poly(Propylene Fumarate)/Diethyl Fumarate Composite Scaffolds

6.1. Introduction

Scaffold design parameters are considered important in order to achieve a functional complex of cell/scaffold constructs, including pore size, porosity, interconnectivity, surface properties, mechanical strength, the amounts and types of filler material, cell seeding density, and exogenous growth factors [295]. In general, transplanted cell population could recognize the differences in these physical and mechanical cues and the subsequent cellular functions might be changed. Modulation in the physical properties as well as changes in scaffold design parameters may influence the various cellular functions, and both stiffness (mechanical cues) and pore geometry (structural cue) among these parameters are of importance to induce the endogenous osteogenic signal expressions.

It is known that the stiffness of scaffold influences adhesion [296], motility [22, 297], morphology [72, 298, 299], proliferation [22, 300, 301], and osteoblastic differentiation [16, 70, 88, 300-302] of cells. Since cells can recognize the modulated mechanical cues (or the changes in stiffness) of the scaffold and the secondary signal transduction occurs through cell-matrix interaction [69]. Recent study reveals that specific lineage of stem cell differentiation cascades can be directed by matrix elasticity [69, 302]. In particular, it has been shown that ECM mechanical properties may regulate the osteogenic signaling mechanisms of cell-extracellular matrix (ECM)

through the sequential activation of FAK, RhoA/ROCK, the extracellular signal regulated kinase/mitogen-activated protein, and Runx2 [16, 22, 70]. Moreover, another study demonstrated that a combination of other stimuli such as ligand presentations on ECM with mechanical cues may enhance the mechano-transduction [72].

In addition to mechanical stimuli, architectural cues for a 3D porous scaffold including porosity, pore size, interconnectivity, and channel orientation of scaffolds are also important scaffold design parameters to affect cellular behaviors [43, 295]. A study with human mesenchymal stem cells on coralline hydroxyapatite scaffolds has shown that pore size could be a controlling factor to vary the BMP-2 mRNA expression level and osteoblastic differentiation determined by alkaline phosphatase (ALP) and osteocalcin (OC) expression. Another in vitro study also demonstrated the effect of porous architecture of 3D silk fibroin scaffolds on ALP and OC expression of BMSCs [303]. An in vivo study using implanted ß-TCP scaffolds in skin folds of mice showed that significantly higher osteoblastic differentiation was observed in higher porosity groups (over 65 %) than lower porosity groups [21]. Moreover, continuous channeled geometry fabricated by solid free form technique has shown a significantly higher cell ingrowth depth compared to a scaffold with random porous structure [304].

In order to investigate the effect of mechanical and architectural cues on the stimulation of osteogenic signal expression, a composite material of poly(propylene fumarate) (PPF) and diethyl fumarate (DEF) was used in the study. This composite has shown unique photo-crosslinking characteristics [77]. By changing the molecular

weight of PPF, the amount of photoinitiator (bis(2,4,6,-trimethylbenzoyl) phenylphosphine oxide, BAPO) and the ratio of PPF and DEF, its crosslinking density and mechanical properties could be modulated. Due to this controllability, the mechanical stiffness of PPF/DEF composite scaffold can easily modulated during fabrication process. Besides of the controllable stiffness, another significant importance of PPF/DEF material is the feasibility as a resin material for stereolithography (SLA). DEF incorporation with PPF reduces the viscosity of PPF and this liquidic polymeric mixture can be utilized for SLA as a resin. SLA uses a laser to initiate photocrosslinking reaction and fabricate a 3D scaffold by vertical layering. Hence, the simultaneous fabrication of desired shape of scaffolds is one of the advantage of SLA compared to other solid free form fabrication techniques, which usually require the secondary step such as a removal of molding.
Another advantage of SLA technique is the capability of controlling scaffold design parameters such as inner pore architecture and mechanical stiffness by the principle of photocrosslinking reaction, then the optimized scaffold properties may stimulate osteogenic signal expression and differentiation. Moreover, SLA fabrication have shown the feasibility of patient- and defect-specific external shape design of bone implants based on a patient's 3D CT scan and transferred computer aided design (CAD) files [91, 92].

The global hypothesis in this study is that the modification in design parameters of 3D PPF/DEF composite scaffolds may facilitate osteogenic signal expression and the enhanced level of signal expressions may be associated with the downstream osteoblastic differentiation of implanted cell population. Therefore, this

study investigated the effect of crosslinking density (i.e., stiffness) and pore size on the endogenous osteogenic signal expression and downstream osteoblastic differentiation of seeded BMSCs on 3D PPF/DEF scaffolds. The specific objective of this study is (1) to characterize the physical properties of 3D macroporous PPF/DEF composite scaffolds, (2) to investigate the effect of DEF content (subsequent changes in stiffness as a mechanical cue) and pore size (structural cue) on osteogenic signal expression profiles and downstream osteoblastic differentiation of rat BMSCs.

6.2. Materials and Methods

6.2.1. Materials

For PPF synthesis, diethyl fumarate, propylene glycol, zinc chloride, and hydroquinone were obtained from Sigma-Aldrich (St. Louis, MO) and analytical reagent grade methylene chloride was purchased from Fisher Scientific (Pittsburgh, PA). Polystyrene standards fro GPC analysis was received from Polymer Laboratories (Amherst, MA). Photoinitiator bis(2,4,6-trimethylbenzoyl) phenylphosphine oxide (BAPO) was obtained from Ciba Specialty Chemicals (Tarrytown, NY). For cell culture reagents, ascorbic acid and β-mercaptoethanol were purchased from Sigma-Aldrich (St. Louis, MO) and alpha-minimum essential medium (α-MEM), penicillin/streptomycin antibiotics, fetal bovine serum (FBS), and trypsin/EDTA were purchased from Invitrogen (Carlsbad, CA). BCA protein assay kit was received from Pierce (Rockford, IL). MTT assay kit was obtained from Sigma-Aldrich. PicoGreen assay kit for the measurement of DNA was obtained from

Molecular Probes. Trisol for RNA extraction was purchased from Sigma-Aldrich. For real time quantitative polymerase chain reaction (qRT-PCR), High Capacity cDNA Archive kit, Universal PCR Master mix (2x), and Taqman® Gene Expression Assays were purchased from Applied Biosystems (Foster City, CA).

6.2.2. PPF synthesis and scaffolds fabrication

PPF was synthesized according to previously reported methods [38]. Briefly, diethyl fumarate and propylene glycol were reacted with zinc chloride as a catalyst and hydroquinone as a crosslinking inhibitor to form intermediate. Then, transesterification was occurred to create final PPF under vacuum condition. After a series of purification, number average molecular weight (Mn) and poly diversity was determined by gel permeation chromatography. For PPF/DEF composite scaffold fabrication, PPF was mixed with DEF with a various weight ratio (Table 13), and 75 wt% of salt porogen crystals (>500 μm for large pore size and 180 - 300 μm for small pore size) as well as 0.5 wt% of photoinitiator bis(2,4,6-trimethylbenzoyl) phenylphosphine oxide compared to polymer mixture amount were homogeneously mixed together. Resulting paste was packed into the glass cylinder mold, and photocrosslinked under UV light for 2 hrs. Crosslinked polymer networks with salt porogens was cut into disks (6.3 mm in diameter and 3 mm in thickness) and placed in water for 3 days to leach out salt. Resulting macroporous PPF/DEF scaffolds were first air-dried for 24 hrs and dried again in vacuum oven for 24 hrs. All experimental groups are listed in Table 13.

Experimental Groups	PPF	DEF	Pore Size (μm)	Porosity (wt %)
L1	100	-	> 500	77.41 ± 0.48
L2	90	10		79.51 ± 1.14
L3	75	25		78.43 ± 0.55
L4	66	33		81.67 ± 0.58
S1	100	-	180 - 300	75.36 ± 0.24
S2	90	10		77.37 ± 0.52
S3	75	25		79.77 ± 0.58
S4	66	33		77.48 ±0.37

Table 13: Experimental groups

6.2.3. Characterization of physical properties of composite scaffolds

6.2.3.1. SEM imaging

Top surface of scaffolds were visualized using scanning electron microscope (SEM) (SU-70, Hitachi, Tokyo, Japan). Samples were coated by a gold sputter, and images were obtained at 3 kV accelerating voltage.

6.2.3.2. Sol fraction test

To assess the crosslinking density of PPF/DEF scaffolds, sol fraction test was performed by previous method [77]. Each photocrosslinked scaffold was placed in 20 ml of methylene chloride solvent in a glass vial. Weight of initial sample before the incubation in solvent (*Wi*) was measured, and samples were incubated on a shaker with 75 rpm for 160 hrs at room temperature. Then, samples with solvent were

transferred onto a weighed filter paper (*Wp*). These were completely dried in an oven at 70℃ for 2 hrs, and weighed again (*Wp+s*). The sol fraction was calculated from the formula below and five independent samples were assessed (n=5).

$$\text{Sol fraction} = \frac{W_i - (W_{p+s} - W_p)}{W_i}$$

6.2.3.3. Mechanical properties

According to the American Society of Testing Materials (ASTM) Standard D695-2a, compressive mechanical testing was performed using the Instron mechanical tester (Instron 5565, Norwood, MA) to measure the compressive modulus and offset yield strength. Each cylindrical porous scaffold with 6 mm in diameter and 12 mm in length was compressed along its vertical axis. Compression was applied at a speed of 1.3 mm/min until the compressive strain reached 0.5 mm/mm. The compressive modulus and yield strength at 1% offset were calculated using Bluehill 2.16 software (Instron). Six replicates in each experimental group were tested (n=6).

6.2.3.4. Permeability

The water permeability of scaffolds was measured by the methods described previously based on Darcey's law [305, 306]. An apparatus was constructed using a 2-liter open container functioning as a water reservoir large enough to keep the pressure across the scaffold near constant (by keeping the height of the water in the apparatus near constant). Attached to the bottom of this reservoir was a short tube in which the scaffold, first wrapped in parafilm to create an air-tight seal along the side

wall, was held. One liter of water was added to the reservoir, and the water penetrated through the scaffold vertically was collected. After 120 seconds, the mass of water collected was recorded and the mass flow rate was calculated. This mass flow rate was converted to volumetric flow rate by using the density of water. This procedure was repeated with 5 independent samples (n=5). The permeability (K) was then calculated using the equation below:

$$K = \frac{\Delta Q \times L \times \mu_{H_2O}}{\Delta P \times A_{cs}}$$

where ΔQ is a volumetric flow rate, L is the length of a scaffold, μ_{H_2O} is the viscosity of water (8.90 x 10^{-4} Pa s at 25°C), ΔP is a hydrostatic pressure difference between top and bottom of water column, and A_{CS} is the cross-sectional area of a scaffold.

6.2.3.5. Surface hydrophilicity

The hydrophilicity of the surface of the composite material was determined by a static contact angle measurement. Composite disks were fabricated by placing the PPF/DEF/BAPO mixture into rectangular mold on glass plates and crosslinked under UV light for 2 hrs [38]. 5 μl droplet of water was dropped onto the disk surface and a picture was then taken after 15 sec. Image J software was used to analyze the angles at both sides of each water droplet and the average of both values was utilized for the further statistical analysis. Three measurements were performed for each sample and independent triplicate samples were tested.

6.2.3.6. Protein adsorption test

The level of adsorbed protein onto the scaffold surface was measured by the method previously described [172]. Briefly, scaffolds were first completely wetted by a series of pre-socking: 1hr in ethanol, 30 min in PBS (twice), and overnight incubation in PBS again. Samples were then placed in culture media with 10% FBS for 4 hrs at 37℃ on the shaker (25 RPM). After incubation, samples were washed with PBS 3 times, and adsorbed proteins were extracted by 1 hr incubation in 250 µl of 1% sodium dodecyl sulfate (SDS) solution (repeated 2 times). BCA protein assay kit was used to determine the protein concentration. This test was completed with triplicate samples and three measurements (n=3).

6.2.4. Rat Bone Marrow Stromal Cell Isolation and Culture

Rat BMSCs were isolated from Wistar Hanover rats (male, 101-125g, Taconic) following a University of Maryland approved IACUC animal protocol according to the method previously described [38]. Briefly, femur and tibia were dissected from a rat euthanized by carbon dioxide gas and incubated in α-MEM culture media containing 10 (v/v)% of penicillin/streptomycin for 10 min. This incubation step was repeated three times. Then, both sides of explanted bones were clipped off and whole bone marrow inside was flushed out with 10 ml of fresh culture media using a syringe. Collected bone marrow was first suspended, filtered through a cell strainer with 70 µm pores. Filtered bone marrow was centrifuged, resuspended with culture media containing 10 % of FBS, and plated in a T-25 cell culture flask. Media was changed every 2-3 days, and cells were passaged up to 3 times. All

samples were incubated under standard cell culture conditions of 37 and 5 % of CO_2 level.

6.2.5. Initial metabolic activity of rat BMSCs

MTT assay was used to determine metabolic activity of implanted BMSC population influenced by (1) dissolved DEF in aqueous cell culture media and (2) the PPF:DEF ratio in composite scaffolds. In order to demonstrate the cytotoxic effect of dissolved DEF amount in cell culture media on monolayer cell, 0.1 million cells were seeded in each well of a 24 well plate and allowed to attach for 24 hrs. 0, 5, 10, and 20 mM of DEF in 10% FBS cell culture media was applied in a well and the plate was incubated for 1, 2, and 4 hrs in a incubator. 50 (v/v)% of methanol in same culture media was used as a negative control. To determine the effect of PPF:DEF ratio in 3D composite scaffolds on metabolic activity of seeded BMSC population, 0.3 million cells were seeded onto a sterilized scaffold with 100:0, 90:10, 75:25, and 66:33 of PPF:DEF ratio. After 4 hrs of incubation to allow cells to attach to the surface of scaffolds, cell/scaffold constructs were washed with PBS. Then, 200 µl of 5 mg/ml of reconstituted MTT was added with 2 ml of 10% FBS media to each well for both assays, and incubated 2.5 hrs to allow the formation of MTT formazan crystals. Resulting crystals were dissolved with 200 µl of solublization solution and 200 µl of supernatant was transferred to 96 well plate to record the optical density at 570 nm using M5 SpectraMax microplate reader (Molecular Devices, Sunnyvale, CA).

6.2.6. Osteogenic signal expressions

Total RNA was isolated from cell/scaffold construct with Trisol following the protocol provided by the manufacturer. Isolated RNA was reverse transcribed using the High Capacity cDNA Archive kit. For the pre-amplification, cDNA sample was first mixed with the same volume of pooled 20x Taqman Gene Expression assay including four osteogenic growth factor genes including bone morphogenic protein-2 (BMP-2), fibroblast growth factors-2 (FGF-2), transforming growth factor-β1 (TGF-β1), and vascular endothelial growth factor (VEGF), two osteogenic marker genes including ALP and OC, and a transcriptional factor of Runx2 as listed in Table 14. This mixture was then incorporated with two volume of PreAmp master mix. Thermal condition for the PCR pre-amplification reaction was 10 min at 95℃ and 10 cycles of 15 sec at 95℃, and 4 min at 60℃. The pre-amplified cDNA sample was diluted with 1x TE buffer (1:5) and utilized to investigate the relative gene expression level profiles of target genes. A house-keeping gene, glyceraldehyde-3-phosphate dehydrogenase (GAPDH) was used as an endogenous control gene. qRT-PCR was conducted on the ABI Prism 7000 sequence detector (Applied Biosystems), using thermal condition of 2 min at 50℃, 10 min at 95℃, and 50 cycles of 15 s at 95℃ and 1 min at 60℃. Relative gene expression level of genes of interest was normalized GAPDH control gene. Mean of fold changes compared to the calibrator group was analyzed using ΔΔCt method and its standard deviations are reported (n=3).

Osteogenic merkers and signals	Taqman ID
ALP	Rn00564931_m1
OC	Rn00566386_g1
BMP-2	Rn00567818_m1
FGF-2	Rn00570809_m1
TGF-beta1	Rn00572010_m1
VEGF	Rn00582935_m1
RUNX2	Rn01512296_m1
GAPDH	Rn99999916_s1

Table 14: Taqman ID list of osteogenic markers and signals

6.2.7. Osteogenic differentiation of implanted cell population

Early osteogenic differentiation of rat BMSCs was first determined by ALP protein activity. ALP activity was determined by para-nitrophenol production using p-nitrophenyl phosphate (pNPP) assay (Sigma-Aldrich). Cell lysate was obtained from cell/scaffold constructs as described previously [38]. Briefly, samples in 1 ml of distilled water in a small tube were lysated through three cycles of freeze (30 min at -80℃), thaw (30 min at 37℃), and sonication in the bath sonicator (30 min). The supernatant containing protein and DNA was mixed with pNPP liquid substrate, incubated for 1 hr at 37℃. After stopping the reaction using 2 M NaOH, the absorbance was recorded at 405 nm using a microplate. ALP activity was normalized by DNA amount from the same supernatant, which was measured using the

PicoGreen assay kit. mM ALP/μg DNA was reported and each experimental group was analyzed with triplicate.

6.2.8. Statistical analysis

The data from all studies were analyzed by one-way analysis of variance (ANOVA) and Turkey's multiple-comparison test. $p<0.05$ was considered to show significant difference between experimental groups. The means and the standard deviations were reported in each figure.

6.3. Results

6.3.1. Characterization of 3D PPF/DEF scaffolds

3D macroporous composite PPF:DEF scaffolds with high interconnectivity were fabricated by a simple salt porogen leaching method. Top surface images by SEM showed the porous structure of the scaffolds with two different pore sizes (Fig 21A and 21B). The physical properties of PPF/DEF scaffolds were modified by varying the scaffold design parameters including the PPF:DEF ratio and the pore size. In order to investigate the photo-crosslinking characteristics of these composite scaffolds, sol fraction was first determined (Fig 22). After 120 hrs of incubation in organic solvent, DEF incorporated scaffold groups exhibited significantly lower sol fraction in both pore sizes compared to the PPF control group ($p = 2.38\times10^{-8}$ for large pore groups and 2.36×10^{-5} for small pore groups). Moreover, 75 and 66% of PPF groups with small pore size (S3 and S4) showed significantly higher sol fraction ($p = 2.81\times10^{-2}$ and 4.80×10^{-2}, respectively). Decreasing sol fraction by increasing DEF

contents is related with an increase in a crosslinking density of the composite scaffolds and this relationship is also confirmed by the mechanical testing (Fig 23).

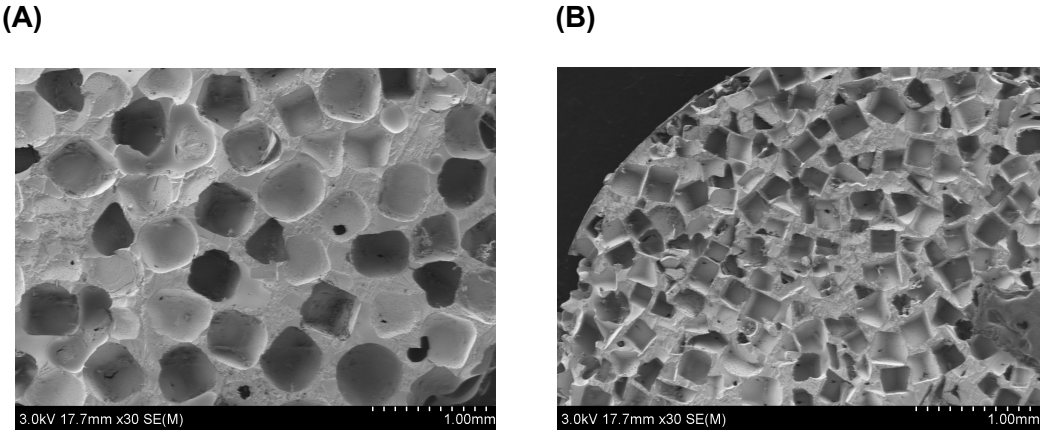

Figure 21: Top surface of scaffolds of 66:33 ratio of PPF/DEF. (A) Large pore size scaffold and (B) small pore size scaffold.

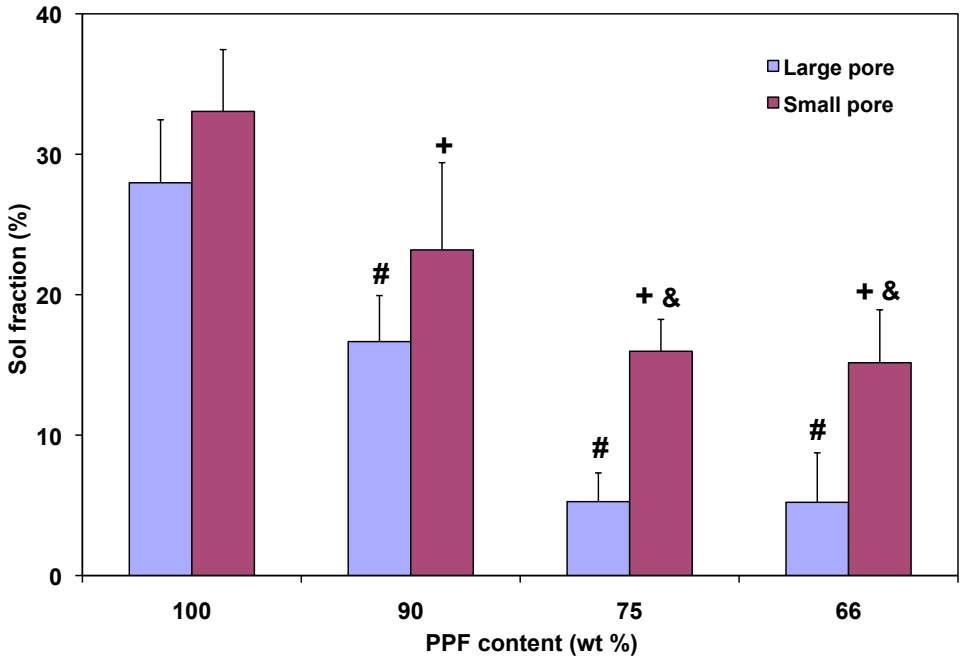

Figure 22: Sol fraction test. # indicates a significant differences between different PFP contents within a large pore size groups while + indicates a significant differences within a small pore size groups ($p<0.05$). & indicates a significant difference between two pore size groups in the same PPF:DEF ratio ($p<0.05$).

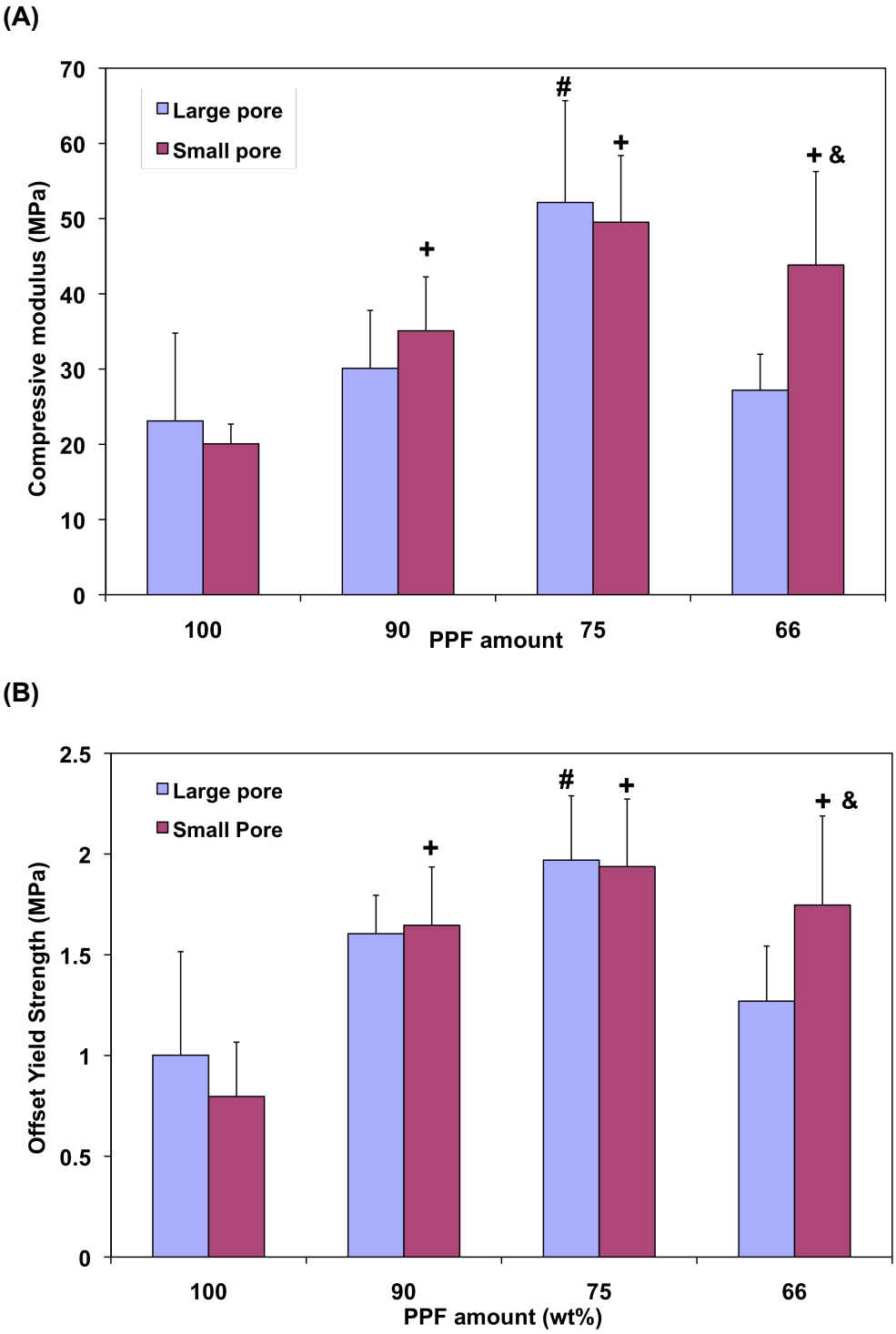

Figure 23: Mechanical testing. (A) compressive modulus and (B) off-set yield strength. # indicates a significant differences between different PFP contents within a large pore size groups while + indicates a significant differences within a small pore size groups ($p<0.05$). & indicates a significant difference between two pore size groups in the same PPF:DEF ratio ($p<0.05$).

Compressive modulus data in Fig 23A demonstrated that increasing DEF content up to 25% resulted in increasing scaffold modulus. 75% of PPF group showed the highest mechanical property in both pore size groups and all DEF incorporated groups with small pores exhibited significantly higher modulus compared to the PPF control ($p = 4.67\times10^{-5}$). In addition, Increasing mechanical strength of PPF:DEF composite scaffold by increasing amount of DEF was also found in offset yield strength data (Fig 23B) and these observations in 3D macroporous scaffolds was also seen in nonporous photo-crosslinked composites [77].

Water permeability from the top to the bottom of porous scaffolds was assessed (Fig 24). Due to the hydrophobicity of PPF polymer, 100 and 90% of PPF groups showed a low level of water permeability, however 75 and 66% PPF groups exhibited increased permeability. 75% of PPF and 25% of DEF incorporation resulted in significantly higher water permeability in both pore size groups ($p = 1.73\times10^{-3}$ for L3 and 2.23×10^{-2} for S3). In these PPF:DEF ratios, as expected, large pore groups showed higher permeability but without any significance between pore sizes. Then, hydrophilicity of the PPF/DEF composite was evaluated by the contact angle measurement (Fig 25). Decreasing contact angle by increasing DEF content indicated increasing hydrophilicity and both 75 and 66 % of PPF groups showed significantly higher hydrophilicity (lower hydrophobicity) than both 100 and 90 % of PPF groups ($p = 1.15\times10^{-12}$). Passive protein adsorption to PPF:DEF composite surfaces was also determined (Fig 26). In small pore groups, DEF incorporated groups showed significantly higher protein adsorption compared to the PPF control groups ($p = 1.92\times10^{-4}$) although the levels of adsorption in large pore groups were not

significantly different. DEF incorporated groups with small pores exhibited significantly higher protein adsorption.

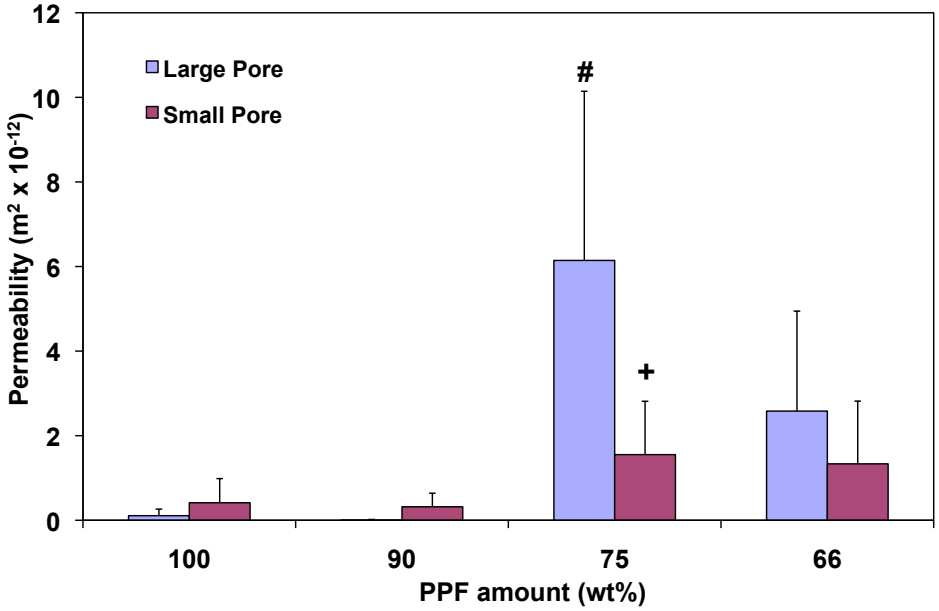

Figure 24: Permeability. # indicates a significant differences between different PFP contents within a large pore size groups while + indicates a significant differences within a small pore size groups ($p<0.05$).

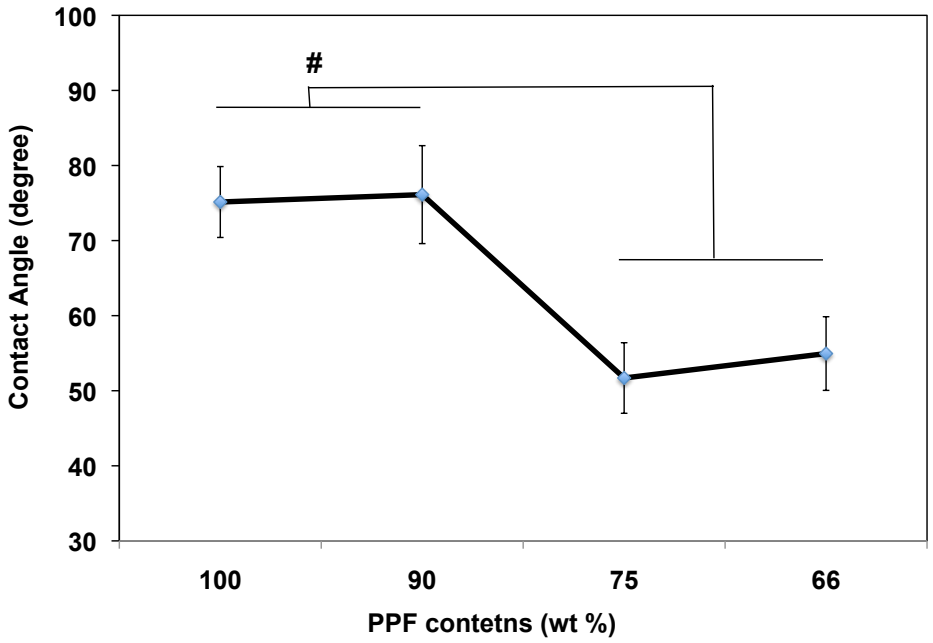

Figure 25: Contact angle measurement. # indicates a significant differences between groups ($p<0.05$).

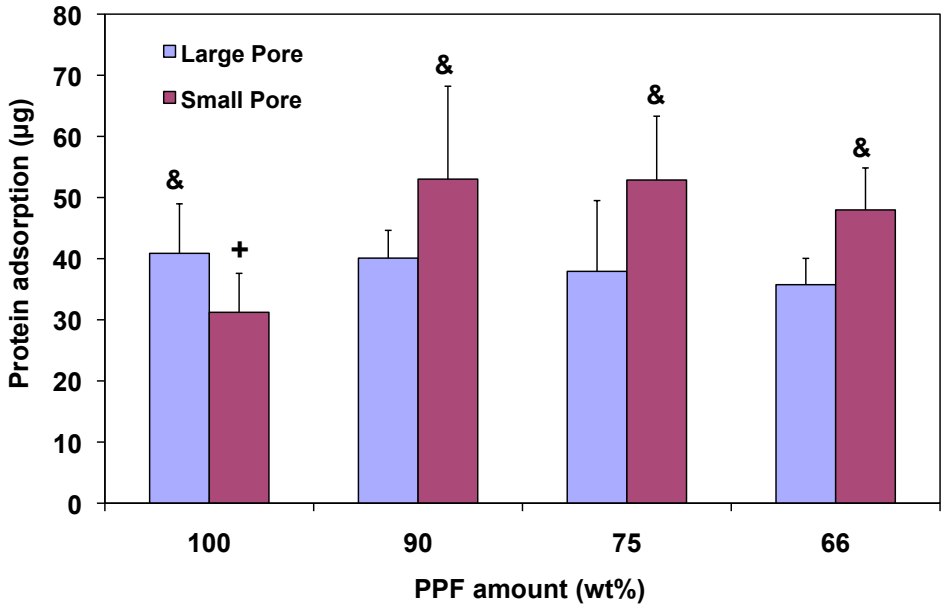

Figure 26: Protein adsorption. + indicates a significant differences within a small pore size groups ($p<0.05$). & indicates a significant difference between two pore size groups in the same PPF:DEF ratio ($p<0.05$).

6.3.2. Initial metabolic activity of BMSCs onto 3D PPF/DEF scaffolds

The effect of free DEF molecules in aqueous cell culture media on the metabolic activity of monolayer cell was investigated (Fig 27A). By using MTT assay, increasing DEF content in the media resulted in a decrease in initial metabolic activity of cells in tissue culture well plates for up to 4 hrs. 20 mM of DEF showed similar level of the metabolic activity to the negative control (50% methanol group) and all DEF added groups from 5 to 20 mM exhibited the same level as the negative control after 4 hr of incubation. Then, the effect of DEF incorporation on the transplanted BMSCs onto photocrosslinked PPF/DEF composite scaffolds was also assessed. In Fig 27B, all DEF incorporated groups showed the same level of cellular metabolic activity to the PPF control up to 24 hrs incubation. Therefore, once the DEF molecules were participated in photo-crosslinking reactions with PPF polymer chains, the negative effect on cellular metabolic activity by increasing DEF amounts was not observed in 3D scaffold systems.

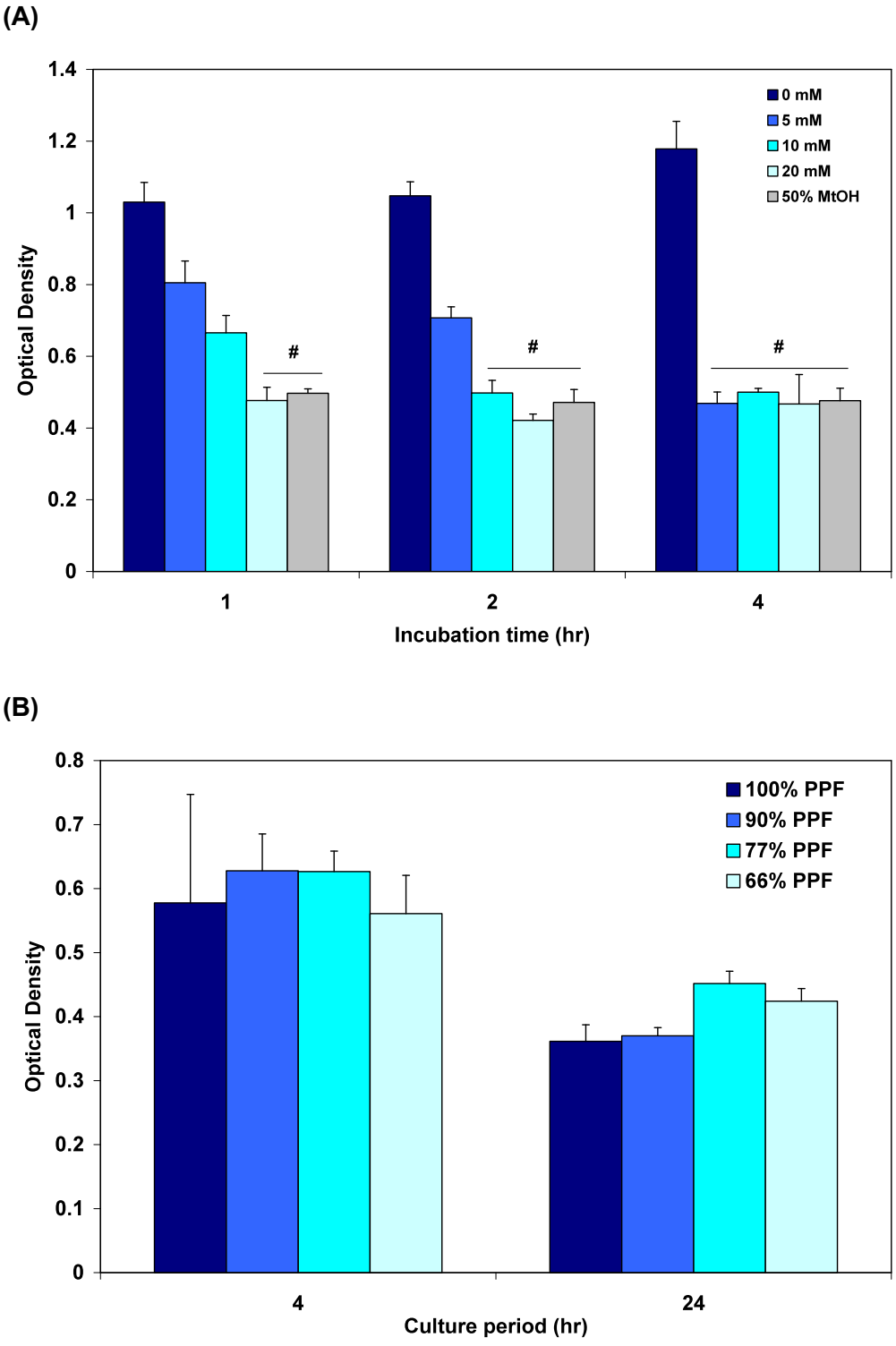

Figure 27: Initial metabolic activity of rat BMSCs exposed to DEF molecules in aqueous culture media (A) and seeded onto photo-crosslinked PPF/DEF scaffolds (B). # indicates a significant differences between groups ($p<0.05$).

6.3.3. Osteogenic signal expression profiles of rat BMSCs cultured in 3D PPF/DEF scaffolds

The effect of DEF incorporation and pore size of scaffolds on osteogenic signal expression was investigated by using quantitative RT-PCR on day 8 (Fig 28). For BMP-2 (Fig 28A), DEF incorporated groups with a large pore exhibited significantly higher expression level compared to the PPF control ($p = 2.74\times10^{-6}$) and 75% PPF group showed more than 4.4 fold changes. These DEF incorporated groups also showed significantly higher BMP-2 expression than small pore groups although PPF control with small pore group showed higher expression than any experimental groups.

Other osteogenic signals including FGF-2 and TGF-β1, and angiogenic factor VEGF showed similar expression profiles. For FGF-2 (Fig 28B), a clear trend of increasing expression was observed in large pore groups by increasing DEF amount. 66% of PPF and 33% of DEF scaffolds with large pore (group L4) have shown about 4 fold increase compared to the PPF control as a calibrator group (group L1). Significantly higher FGF-2 expression was observed in DEF incorporated groups with large pores compared to the PPF control ($p = 6.62\times10^{-6}$) and these groups with large pore showed significantly higher expression level than those with small pores. In small pore groups, DEF incorporated scaffolds did not show higher expression than the PPF control. This observation indicating the relationship between increasing DEF amount and increasing mRNA expression was also found in TGF-β1 (Fig 28C) and VEGF (Fig 28D). For both osteogenic signals, a similar trend of increasing expression with increasing DEF amount was observed in large pore groups. 66% of

PPF and 33% of DEF scaffolds with large pore (group L4) exhibited about 4.4 fold increase in TGF-β1 expression and 5.4 fold increase in VEGF expression compared to the PPF control. Groups with two higher DEF amount with large pores (group L3 and L4) showed significantly higher TGF-β1 expression ($p = 1.07\times10^{-5}$) and all DEF incorporated groups with large pores showed significantly higher VEGF expression ($p = 4.74\times10^{-8}$) than the PPF control. The pattern of higher expression in large pore groups than in small pore groups was also found in both osteogenic signal expression profiles.

In Fig 28E, Runx2 transcription factor expression in large pore groups showed the same clear trend of significantly increasing profile by increasing the DEF incorporation level ($p = 2.01\times10^{-5}$) while small pore groups did not exhibit any significant difference between groups with different PPF:DEF ratio. In large pores, 66% PPF group (L4) showed more than 3 fold increase than the calibrator group (L1) and both 75:25 and 66:33 of PPF:DEF ratio with large pore (L3 and L4) showed significantly higher Runx2 expression levels compared to those with small pores (S3 and S4) ($p = 9.55\times10^{-3}$ and 7.33×10^{-4}, respectively).

(A)

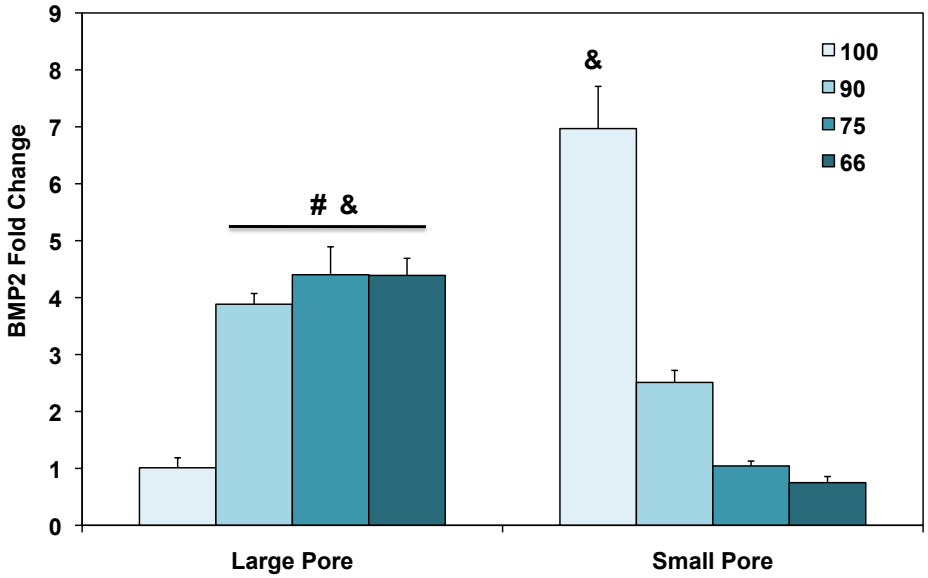
BMP2 Fold Change
9
8
7
6
5
4
3
2
1
0
&
&
100
90
75
66
Large Pore
Small Pore

(B)

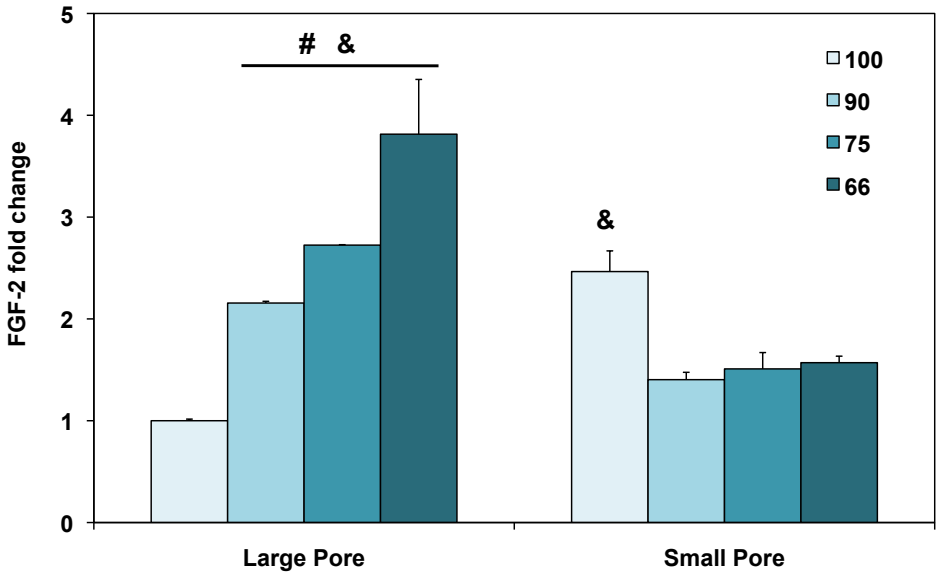
FGF-2 fold change
5
4
3
2
1
0
&
&
100
90
75
66
Large Pore
Small Pore

(C)

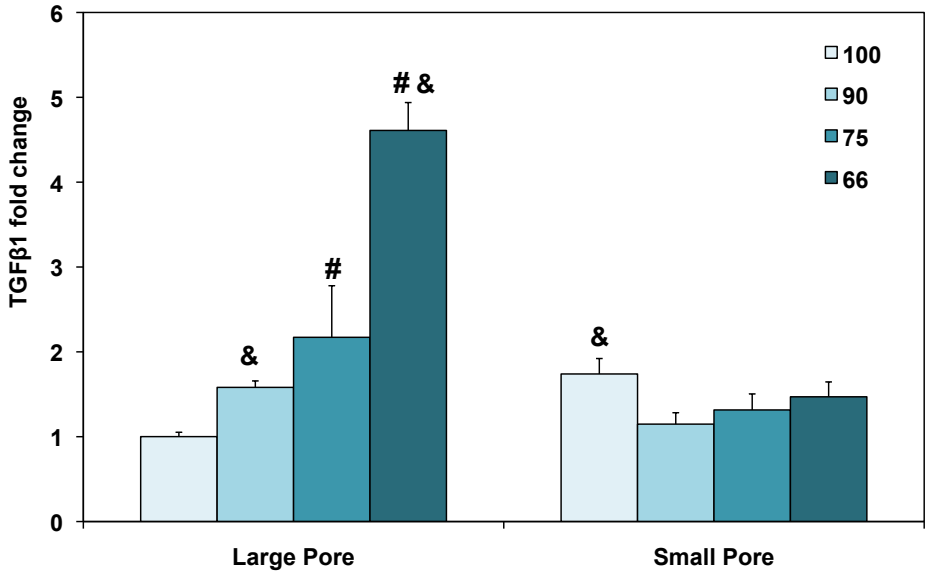
TGFβ1 fold change
6
5
4
3
2
1
0
100
90
75
66
&
#
&
&
Large Pore
Small Pore

(D)

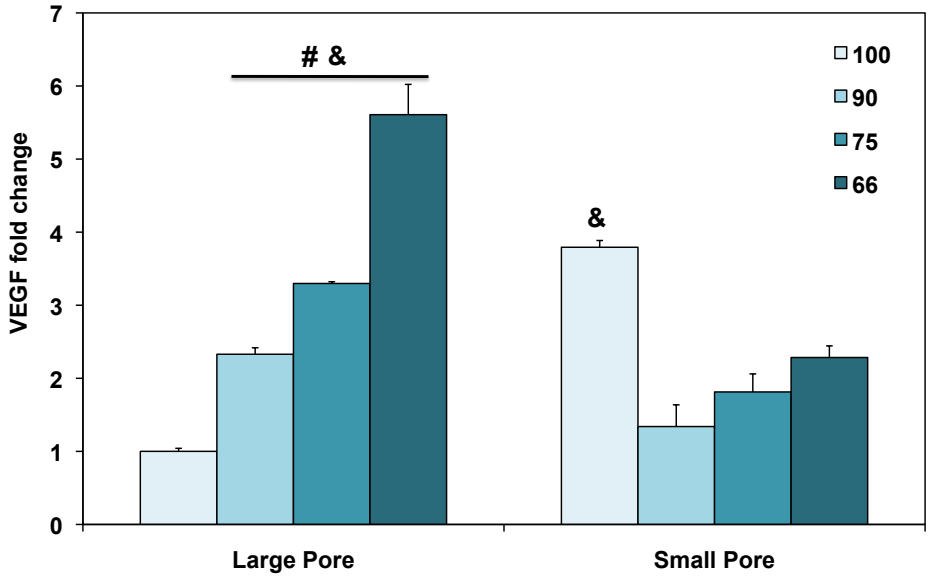
VEGF fold change
7
6
5
4
3
2
1
0
100
90
75
66
&
&
Large Pore
Small Pore

(E)

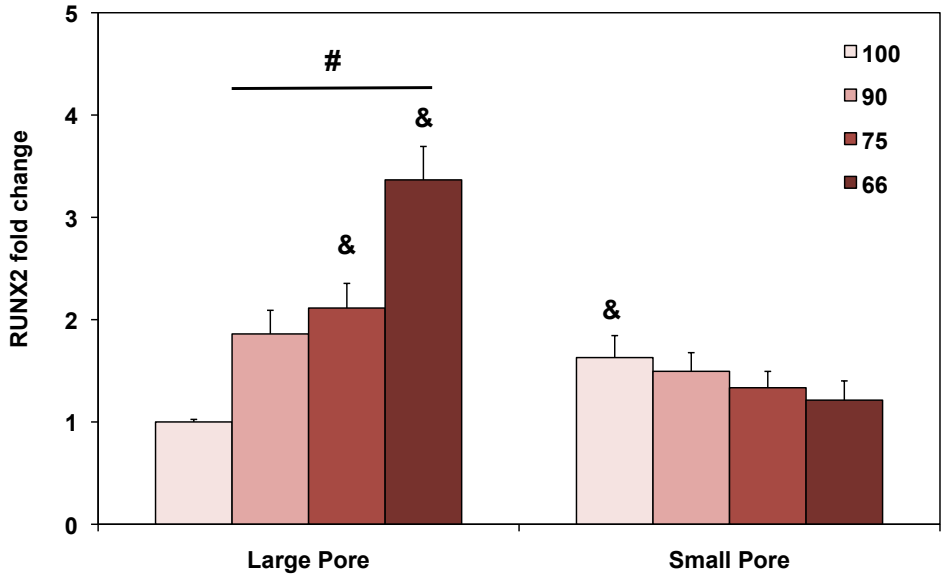

Figure 28: Osteogenic signal expression profiles of tranplanted rat BMSCs population on day 8 including BMP-2 (A), FGF-2 (B), TGF-β1 (C), VEGF (D), and Runx2 (E). # indicates a significant differences between different PFP contents within a large pore size groups while + indicates a significant differences within a small pore size groups ($p<0.05$). & indicates a significant difference between two pore size groups in the same PPF:DEF ratio ($p<0.05$).

6.3.4. Osteoblastic differentiation

ALP and OC mRNA expressions were assessed by using RT-PCR (Fig 29A an 29B) to determine the relation between stimulated osteogenic signal expressions by changing scaffold parameters and downstream osteoblastic differentiation of transplanted BMSCs in 3D PPF/DEF scaffolds. As an early osteoblastic differentiation marker, ALP mRNA expression on day 8 also showed a correlated trend of increasing expression by incorporating more DEF in composite scaffolds with large pores (Fig 29A). DEF incorporated groups with large pores showed significantly higher ALP expression compared to the PPF control (group L1) (p =

3.42×10^{-7}) and these groups also exhibited significantly higher expression than small pore groups. In small pore groups, upper limit of DEF incorporation (group S4) showed significantly higher expression than the PPF control (group S1) ($p = 2.02\times10^{-8}$). In addition, as a late osteoblastic differentiation marker, it is indicated that DEF incorporation would enhance the OC expression in both pore sizes compared to PPF control ($p = 9.73\times10^{-6}$ in large pores and 8.81×10^{-7} in small pores) (Fig 29B). To confirm the influence of enhanced expression of osteogenic signals into osteoblastic differentiation, ALP protein activity was also measured over the 8 days of culture periods (Fig 30). The result demonstrated that all experimental groups showed generally increasing intracellular ALP production (normalized by DNA level) up to day 8. In large pore scaffolds, group L4 (66% of PPF and 33% of DEF) showed significantly higher ALP protein level compared to the PPF control (group L1) at each time point ($p = 7.62\times10^{-9}$, 1.14×10^{-2} and 2.40×10^{-3}, respectively).

6.4. Discussion

The main objective of this study was to determine which 3D PPF/DEF composite scaffold parameters facilitate endogenous osteogenic signal expressions and downstream osteoblastic differentiation. Two main scaffold design parameters on the first study are the DEF content and the pore size of PPF/DEF porous scaffolds. It has been shown that DEF incorporation in PPF polymer increased crosslinking density decreased the sol fraction of cylindrical composite material, and therefore the mechanical properties including compressive modulus and fracture strength were increased by incorporating DEF with PPF, up to 25 % [77]. Based on these

(A)

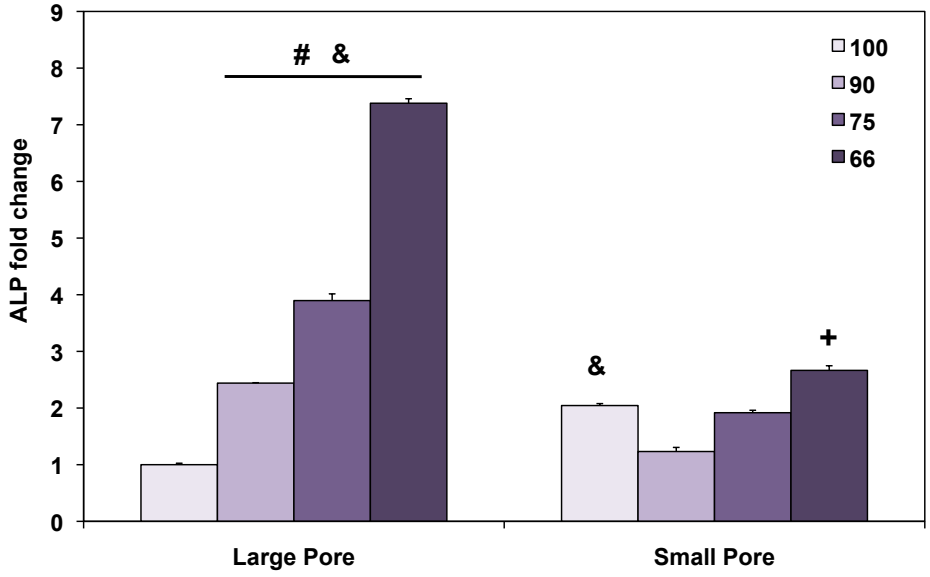

(B)

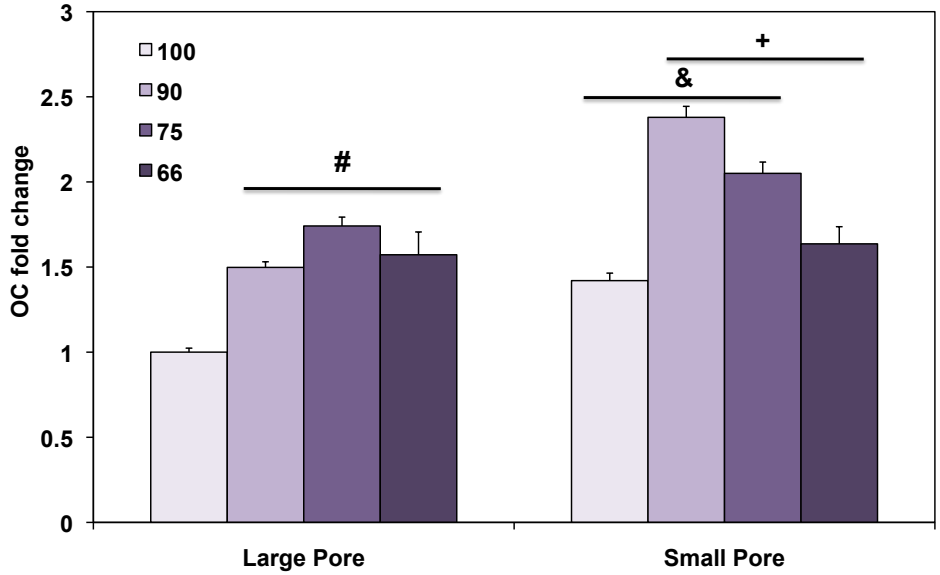

Figure 29: Osteogenic differentiation was determined by ALP and OC mRNA expression on day 8. # indicates a significant differences between different PFP contents within a large pore size groups while + indicates a significant differences within a small pore size groups ($p<0.05$). & indicates a significant difference between two pore size groups in the same PPF:DEF ratio ($p<0.05$).

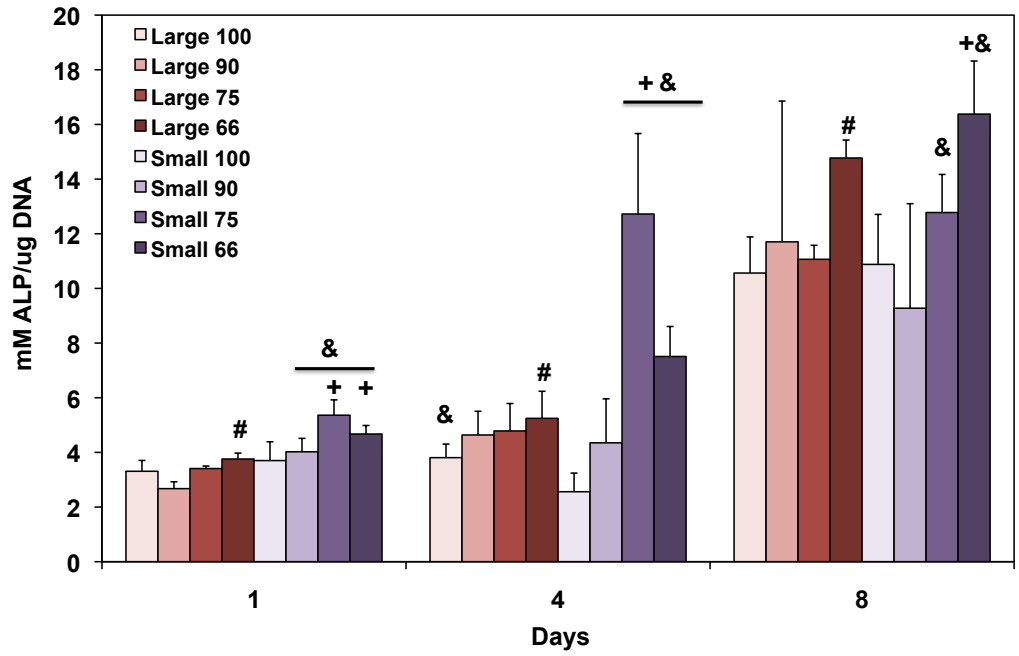

Figure 30: Normalized ALP protein expression over 8 days of culture. # indicates a significant differences between different PFP contents within a large pore size groups while + indicates a significant differences within a small pore size groups ($p<0.05$). & indicates a significant difference between two pore size groups in the same PPF:DEF ratio ($p<0.05$).

characteristics, the photocrosslinking properties of 3D macroporous PPF/DEF scaffolds were first examined in this study. By a simple salt porogen leaching method, interconnected porous structure of PPF/DEF scaffold was obtained while the pore size was controlled with the size of porogen salt crystals (Fig 21). Sol fraction (Fig 22) and mechanical properties (Fig 23) of 3D macroporous PPF/DEF scaffolds have exhibited the similar trend to the non-porous PPF/DEF constructs in the previous study [77]. Lower sol fraction levels in DEF incorporated groups in both pore size groups indicated higher crosslinked fraction in PPF/DEF composites and 66 and 75% of PPF groups exhibited the highest level of crosslinked fractions, indicated by the lowest sol fraction level. Significantly higher sol fraction in S3 and S4

compared to L3 and L4 might be related to an easier transport of solvent and subsequent contact with scaffold surfaces, rather than the actual increase in crosslinking density in scaffolds with a small pore. The penetration of methylene chloride solvent into inner region of scaffolds is more efficient in large pore scaffolds, and the solvent then dissolved more polymers in the scaffold surface. This could be associated with lowering the sol fraction level. The mechanical testing data of macroporous PPF/DEF scaffolds in Figure 23 indicated that 25 % of DEF is an optimal level to achieve the highest compressive modulus and offset yield stength. This result also indicated that the compressive modulus and yield strength of PPF/DEF composite scaffolds are within a range of those of native human cancellous bone (10-900 MPa of compressive modulus and 0.2-14 MPa of yield strength) [307-309].

75:25 of PPF:DEF incorporation also showed the highest water permeability in both pore sizes (Fig 24) and the result indicated that DEF incorporation might change the hydrophilicity of scaffold surface and the permeability might be related to the modified hydrophilicity. In addition, changing DEF contents in PPF/DEF scaffolds and subsequent surface properties might be more effective in order to increase water permeability than changing pore sizes. As a structural cue, permeability could be one of the stimuli to enhance the signal expression of progenitor cells. It has been demonstrated that increasing permeability induced chondrogenic differentiation of BMSCs on 3D poly(ε-caprolactone) scaffolds since diffusion, oxygen tension, and nutrient exchange would be affected by the level of permeability [310]. A scaffold with 860 μm of pore size showed higher permeability

as well as increased expression ratio of collagen type 2 to collagen type 1, which was not shown in scaffolds with low permeability. The contact angle measurement (Fig 25) confirmed this relationship. DEF incorporation increased the hydrophlicity as shown in decreased contact angles, and increasing surface hydrophilicity might be related to increasing permeability of 3D scaffolds.

Although the free DEF molecules in aqueous media showed the negative effect on the monolayer cells (Fig 27A), crosslinked PPF/DEF scaffolds did not show any decrease in the metabolic activity of transplanted BMSCs up to 24 hrs (Fig 27B). This result demonstrated that the crosslinking reaction with the aid of photoinitiator and UV light is suitable to allow DEF molecules participate in the formation of polymeric network. Moreover, the crosslinked PPF/DEF scaffolds could be a proper platform for bone tissue engineering in terms of both mechanical strength (Fig 23) and biocompatibility (Fig 27).

In order to investigate the optimized scaffold design parameters on the osteogenic signal expression, quantitative RT-PCR was performed on day 8 (Fig 28). It is demonstrated that DEF incorporated groups with a large pore size might facilitate the osteogenic signal expressions including BMP-2, FGF-2 and TGF-β1 as well as the expression of both angiogenic signal VEGF a transcriptional factor Runx2. Within large pore groups, these signal expressions were dependent on the DEF contents and the subsequent changes in crosslinking density or stiffness of composite scaffolds. General increasing expression of these signals in large pore groups might be explained by the Runx2 mediated intracellular signaling transduction. The binding and stimulation of BMP-2 and TGF-β1 might be associated with Runx2 transcription

factor expression via Smad and MAPK pathway [5, 18, 311, 312] while FGF-2/MAPK/Runx2 pathway might promote the osteoblast maturation [18, 19, 292]. Hence, the increasing Runx2 expression pattern by increasing DEF content in large pore groups (Fig 28E) might be associated with enhanced level of BMP-2, TGF-β1, and FGF-2 expression. It might be speculated that modulation of PPF/DEF properties could upregulate of these growth factor genes and enhanced expression might increase the possible binding of these proteins to the cells. Finally, the bindings might stimulate the downstream signal pathway to induce the Runx2 expression [18] and further osteoblastic differentiation marker expression such as ALP and OC [6, 313]. This correlated expression pattern of osteogenic signals demonstrated that altering the scaffold design parameters, especially varying DEF content within large pore geometry in this study, influenced the stimulation of endogenous signal expression through the intracellular signaling mechanisms. In addition, upregulated VEGF expression is also related with increasing DEF amount (Fig 28D). Proper osteointegration of implant materials and bone tissue regeneration must be closely related with neovascularization and angiogenesis, it is of importance to investigate the VEGF expression profile along with other osteogenic signal expressions. FGF is involved both osteogenesis and angiogenesis [314-316], and its angiogenic exertion is in the direct way [315] and through VEGF [317]. VEGF expression is also implicated in aspect of the stimulation of osteoblastic differentiation and the regulation of bone remodeling [318, 319]. In addition, FGF-2 may regulate VEGF expression [320] and VEGF release from osteoblasts was stimulated by FGF-2 through Rho-kinase involved SAPK/JNK and MAPK mechanism [321-324].

Therefore, similar expression profiles of FGF-2 and VEGF in Figure 28B and 28D could confirm the relationship between those signal expressions during osteoblastic differentiation. Upregulated expression pattern by increasing incorporated DEF amount in composite scaffolds shows 4 fold increase in FGF-2 and 5.3 fold increase in VEGF in L4 group compared to L1 calibrator group. From this observation, it might be speculated that the modulation of PPF/DEF scaffold's mechanical properties by varying the DEF content could stimulate the Runx2 mediated osteogenic signal expressions and VEGF mRNA expression.

However, this close relation between the DEF incorporation and the stimulated signal expression was not observed in small pore groups. Although increasing signal expression by increasing DEF content in group S2, S3, and S4 was seen, however the fold changes in these groups were lower than the control S1 group in small pore scaffolds (Fig 28). This might indicate the possible existence of other controlling factor, and the pore size of scaffolds could influence the signal expression profiles. We speculated that the large pore geometry is more advantageous for transport of nutrient and waste removal in aqueous in vitro environment, and water permeability data in Figure 4 confirms that large pore groups allow higher level of transport than small pore groups. Another studies also suggested that large pore sizes (325 μm) would help cell migration toward the center of the scaffold and reduce the formation of cell aggregation that might inhibit the diffusion [325] while in vivo bone ingrowth was increased as the pore size increased from 350 to 800 μm at 4 weeks post-implantation [326]. Therefore, in the present study, it is suggested that a large pore size (> 500 μm) could assist the enhancement of signal expression that was

influenced by the stiffness of PPF/DEF scaffolds. Moreover, the expression levels in DEF incorporated scaffolds with large pores (group L2, L3, and L4) are higher than that of DEF incorporated scaffolds with small pores (group S2, S3, and S4) for FGF-2, TGF-β1, VEGF, and Runx2. Therefore, we speculated that both scaffold design parameters in the present study including DEF incorporation and pore size could influence the upregulation of signal expression. DEF content and subsequent changes in stiffness are not the only factor to induce the signal expressions, and the combined effect with pore geometry design could affect the signal expressions of implanted BMSC population.

To validate if the enhanced signal expression is related to downstream osteoblastic differentiation, both ALP and OC mRNA expression on day 8 (Fig 29) and ALP protein activity over 8 days (Fig 30) were determined. The highest expression of ALP in L4 group was more than 7 fold change compared to L1 calibrator (Fig 29A), and the enhanced level of ALP expression in this group might indicate the synergetic effect of DEF incorporation and pore size design. In addition, it might be anticipated that upregulated signal expressions could be associate with osteoblastic differentiation of BMSCs. Upregulated endogenous expression of BMP-2, TGF-β1, and FGF-2 might stimulate the activation of Runx2 expression, and activated Runx2 could express the downstream ALP expression through the Smad pathway [311, 327, 328]. Fig 29B also indicated the combined effect of DEF incorporation and pore size on the OC expression as the late osteoblastic differentiation marker although the expression level was higher in small pore groups. The ALP gene expression was confirmed by ALP protein activity (Fig 30), and it has

been determined that L4 and S4 groups showed statistically higher ALP activity on day 8.

6.5. Conclusions

This investigation to optimize the scaffold design parameters including PPF/DEF ratio and pore size in 3D macroporous PPF/DEF composite scaffolds demonstrated that the enhancement of osteogenic signal expression of rat BMSCs cultured on the scaffolds could be modulated by changing the parameters. Transplanted BMSC population could recognize the changes in the stiffness and surface properties of PPF/DEF scaffolds. In addition, varying pore sizes might also influence the endogenous signal expression profiles by helping the media transport. The result revealed that (1) the modulation of PPF/DEF ratio and pore size changed the physical properties including mechanical stiffness, permeability, and hydrophilicity, (2) osteogenic signal expressions could be stimulated by the modulation of scaffold design parameters, and (3) downstream osteoblastic differentiation might be enhanced by the DEF incorporation in large pore size of scaffolds.

Chapter 7: Summary

The goal of this project was to investigate how scaffold design parameters including physical, mechanical, and biological factors stimulate the endogenous osteogenic signal expression and enhance the subsequent osteoblastic differentiation of transplanted BMSC population in PPF and PPF composite scaffolds. Optimizing the scaffold construct parameters would enhance the gene expression level of osteogenic growth factors and the stimulated osteogenic signal expression could enhance the osteoblastic differentiation of progenitor cells.

The first objective of this work was to investigate the effect of initial cell seeding density of rat BMSCs on 2D PPF disks on the osteogenic signal expression. The optimum level of progenitor cell seeding density could be one of the controlling scaffold design parameters to affect the osteoblastic differentiation of recruited cell population after implantation and successful bone regeneration. It is demonstrated that the temporal gene expression profiles of endogenous osteogenic signals can be upregulated by initial cell seeding density and there could exist the optimal level of progenitor cell seeding density to enhance the expression level.

Then, it was investigated if scaffold construction properties for 3D macroporous PPF/HA scaffolds would facilitate osteoblastic differentiation of transplanted cell populations and evidence of associated osteogenic signal gene expression. This study revealed that altering both the level of HA nanoparticle incorporation and the initial cell seeding density could affect osteoblastic differentiation and growth factor gene expression. The results demonstrated that the

incorporation of HA particles in PPF improved surface properties of composite scaffolds by showing increased roughness, hydrophilicity, protein adsorption, and initial cell attachment. Furthermore, increasing HA amount with lower cell seeding density in 3D PPF/HA scaffolds enhanced osteogenic signal expression and subsequent osteoblastic differentiation of rat BMSCs was facilitated.

Last, we investigated the effect of mechanical as well as structural cues on transplanted cell responses on PPF/DEF composite scaffolds. This study demonstrated that mechanical and structural properties of 3D macroporous PPF/DEF composite scaffolds could be modulated by PPF/DEF incorporation ratio and pore size of the scaffolds. The enhancement of osteogenic signal expression of rat BMSCs cultured on the PPF/DEF scaffolds could be modulated by optimizing these scaffold design parameters since transplanted BMSC population could recognize the changes in the stiffness and surface properties of PPF/DEF scaffolds. The result revealed that the modulation of PPF/DEF incorporation ratio and pore size altered the physical properties including mechanical stiffness, permeability, and hydrophilicity, and osteogenic signal expressions as well as downstream osteoblastic differentiation could be stimulated by the increased DEF incorporation in large pore size of scaffolds.

In order to expand this project to the practical fabrication of clinically available patient specific and defect site specific bone implants, it is necessary to investigate the feasible stereolithographical fabrication of tissue engineered scaffolds as well as the interaction between the transplanted cell population and the sterolithographically fabricated bone grafts. For instance, the effect of inner pore geometry of controlled architecture on stimulated osteogenic signal expression and

enhanced osteoblastic differentiation could be investigated. It could be hypothesized that an increased level of nutrient and oxygen transport as well as waste removal from the inner pore region of the scaffold in the continuous channel geometry obtained by SLA fabrication techniques, would promote endogenous expression of osteogenic signals compared to random pore architecture fabricated by conventional porogen leaching method. In addition, in vivo study could be performed to investigate the optimized scaffold design parameters from the in vitro study could also functionally induce the bone regeneration and tissue integration for the clinical implantation of the cell/scaffold constructs.

Bibliography

1. Tare, R.S., et al., *Skeletal stem cells: phenotype, biology and environmental niches informing tissue regeneration.* Mol Cell Endocrinol, 2008. **288**(1-2): p. 11-21.
2. Bessa, P.C., M. Casal, and R.L. Reis, *Bone morphogenetic proteins in tissue engineering: the road from laboratory to clinic, part II (BMP delivery).* J Tissue Eng Regen Med, 2008. **2**(2-3): p. 81-96.
3. Bessa, P.C., M. Casal, and R.L. Reis, *Bone morphogenetic proteins in tissue engineering: the road from the laboratory to the clinic, part I (basic concepts).* J Tissue Eng Regen Med, 2008. **2**(1): p. 1-13.
4. Ryoo, H.M., M.H. Lee, and Y.J. Kim, *Critical molecular switches involved in BMP-2-induced osteogenic differentiation of mesenchymal cells.* Gene, 2006. **366**(1): p. 51-7.
5. Senta, H., et al., *Cell responses to bone morphogenetic proteins and peptides derived from them: biomedical applications and limitations.* Cytokine Growth Factor Rev, 2009. **20**(3): p. 213-22.
6. Maegawa, N., et al., *Enhancement of osteoblastic differentiation of mesenchymal stromal cells cultured by selective combination of bone morphogenetic protein-2 (BMP-2) and fibroblast growth factor-2 (FGF-2).* J Tissue Eng Regen Med, 2007. **1**(4): p. 306-13.
7. Ng, F., et al., *PDGF, TGF-beta, and FGF signaling is important for differentiation and growth of mesenchymal stem cells (MSCs): transcriptional profiling can identify markers and signaling pathways important in differentiation of MSCs into adipogenic, chondrogenic, and osteogenic lineages.* Blood, 2008. **112**(2): p. 295-307.
8. Dean, D., et al., *Effect of transforming growth factor beta 2 on marrow-infused foam poly(propylene fumarate) tissue-engineered constructs for the repair of critical-size cranial defects in rabbits.* Tissue Eng, 2005. **11**(5-6): p. 923-39.
9. Iwata, J., et al., *Transforming growth factor-beta regulates basal transcriptional regulatory machinery to control cell proliferation and differentiation in cranial neural crest-derived osteoprogenitor cells.* J Biol Chem, 2010. **285**(7): p. 4975-82.
10. Kanczler, J.M., et al., *The effect of mesenchymal populations and vascular endothelial growth factor delivered from biodegradable polymer scaffolds on bone formation.* Biomaterials, 2008. **29**(12): p. 1892-900.
11. Kanczler, J.M., et al., *The effect of the delivery of vascular endothelial growth factor and bone morphogenic protein-2 to osteoprogenitor cell populations on bone formation.* Biomaterials, 2010. **31**(6): p. 1242-50.
12. Karner, E., et al., *Dynamics of gene expression during bone matrix formation in osteogenic cultures derived from human embryonic stem cells in vitro.* Biochim Biophys Acta, 2009. **1790**(2): p. 110-8.

13. Hollinger, J.O., et al., *Recombinant human platelet-derived growth factor: biology and clinical applications.* J Bone Joint Surg Am, 2008. **90 Suppl 1**: p. 48-54.
14. Patel, M., et al., *Cyclic acetal hydroxyapatite composites and endogenous osteogenic gene expression of rat marrow stromal cells.* J Tissue Eng Regen Med, 2010.
15. Salgado, A.J., O.P. Coutinho, and R.L. Reis, *Bone tissue engineering: state of the art and future trends.* Macromol Biosci, 2004. **4**(8): p. 743-65.
16. Khatiwala, C.B., et al., *ECM compliance regulates osteogenesis by influencing MAPK signaling downstream of RhoA and ROCK.* J Bone Miner Res, 2009. **24**(5): p. 886-98.
17. Ling, L., V. Nurcombe, and S.M. Cool, *Wnt signaling controls the fate of mesenchymal stem cells.* Gene, 2009. **433**(1-2): p. 1-7.
18. Franceschi, R.T. and G. Xiao, *Regulation of the osteoblast-specific transcription factor, Runx2: responsiveness to multiple signal transduction pathways.* J Cell Biochem, 2003. **88**(3): p. 446-54.
19. Teplyuk, N.M., et al., *The osteogenic transcription factor Runx2 regulates components of the fibroblast growth factor/proteoglycan signaling axis in osteoblasts.* J Cell Biochem, 2009. **107**(1): p. 144-54.
20. Robling, A.G., A.B. Castillo, and C.H. Turner, *Biomechanical and molecular regulation of bone remodeling.* Annu Rev Biomed Eng, 2006. **8**: p. 455-98.
21. Kasten, P., et al., *Porosity and pore size of beta-tricalcium phosphate scaffold can influence protein production and osteogenic differentiation of human mesenchymal stem cells: An in vitro and in vivo study.* Acta Biomaterialia, 2008. **4**(6): p. 1904-1915.
22. Khatiwala, C.B., S.R. Peyton, and A.J. Putnam, *Intrinsic mechanical properties of the extracellular matrix affect the behavior of pre-osteoblastic MC3T3-E1 cells.* Am J Physiol Cell Physiol, 2006. **290**(6): p. C1640-50.
23. Mygind, T., et al., *Mesenchymal stem cell ingrowth and differentiation on coralline hydroxyapatite scaffolds.* Biomaterials, 2007. **28**(6): p. 1036-1047.
24. Roy, T.D., et al., *Performance of hydroxyapatite bone repair scaffolds created via three-dimensional fabrication techniques.* Journal of Biomedical Materials Research Part A, 2003. **67A**(4): p. 1228-1237.
25. Chu, T.M., et al., *Mechanical and in vivo performance of hydroxyapatite implants with controlled architectures.* Biomaterials, 2002. **23**(5): p. 1283-93.
26. Gauthier, O., et al., *Macroporous biphasic calcium phosphate ceramics: influence of macropore diameter and macroporosity percentage on bone ingrowth.* Biomaterials, 1998. **19**(1-3): p. 133-139.
27. Oh, S.H., et al., *In vitro and in vivo characteristics of PCL scaffolds with pore size gradient fabricated by a centrifugation method.* Biomaterials, 2007. **28**(9): p. 1664-1671.
28. Roy, T.D., et al., *Performance of degradable composite bone repair products made via three-dimensional fabrication techniques.* Journal of Biomedical Materials Research Part A, 2003. **66A**(2): p. 283-291.
29. Hollister, S.J., *Porous scaffold design for tissue engineering.* Nat Mater, 2005. **4**(7): p. 518-24.

30. Leong, K.F., C.M. Cheah, and C.K. Chua, *Solid freeform fabrication of three-dimensional scaffolds for engineering replacement tissues and organs.* Biomaterials, 2003. **24**(13): p. 2363-78.
31. Yeatts, A.B. and J.P. Fisher, *Biological Implications of Polymeric Scaffolds for Bone Tissue Engineering Developed via Solid Freeform Fabrication*, in *Handbook of Intelligent Scaffolds for Regenerative Medicine*, G. Khang, Editor. In Press, Pan Stanford Publishing.
32. Bartolo, P.J., et al., *Advanced Processes to Fabricate Scaffolds for Tissue Engineering*, in *Virtual Prototyping and Bio Manufacturing in Medical Applications*, B. Bidanda and P.J. Bartolo, Editors. 2008, Springer. p. 149-170.
33. Hutmacher, D.W., M. Sittinger, and M.V. Risbud, *Scaffold-based tissue engineering: rationale for computer-aided design and solid free-form fabrication systems.* Trends Biotechnol, 2004. **22**(7): p. 354-62.
34. Pham, D.T. and R.S. Gault, *A comparison of rapid prototyping technologies.* International Journal of Machine Tools & Manufacture, 1998. **38**(10-11): p. 1257-1287.
35. Karageorgiou, V. and D. Kaplan, *Porosity of 3D biomaterial scaffolds and osteogenesis.* Biomaterials, 2005. **26**(27): p. 5474-5491.
36. Mistry, A.S. and A.G. Mikos, *Tissue engineering strategies for bone regeneration.* Adv Biochem Eng Biotechnol, 2005. **94**: p. 1-22.
37. Murphy, C.M., M.G. Haugh, and F.J. O'Brien, *The effect of mean pore size on cell attachment, proliferation and migration in collagen-glycosaminoglycan scaffolds for bone tissue engineering.* Biomaterials. **31**(3): p. 461-6.
38. Kim, K., et al., *Effect of Initial Cell Seeding Density on Early Osteogenic Signal Expression of Rat Bone Marrow Stromal Cells Cultured on Cross-Linked Poly(propylene fumarate) Disks.* Biomacromolecules, 2009. **10**: p. 1810-1817.
39. Hollister, S.J., R.D. Maddox, and J.M. Taboas, *Optimal design and fabrication of scaffolds to mimic tissue properties and satisfy biological constraints.* Biomaterials, 2002. **23**(20): p. 4095-4103.
40. Klenke, F.M., et al., *Impact of pore size on the vascularization and osseointegration of ceramic bone substitutes in vivo.* J Biomed Mater Res A, 2008. **85**(3): p. 777-86.
41. Byrne, E.M., et al., *Gene expression by marrow stromal cells in a porous collagen-glycosaminoglycan scaffold is affected by pore size and mechanical stimulation.* J Mater Sci Mater Med, 2008. **19**(11): p. 3455-63.
42. Kasten, P., et al., *Porosity and pore size of beta-tricalcium phosphate scaffold can influence protein production and osteogenic differentiation of human mesenchymal stem cells: an in vitro and in vivo study.* Acta Biomater, 2008. **4**(6): p. 1904-15.
43. Karageorgiou, V. and D. Kaplan, *Porosity of 3D biornaterial scaffolds and osteogenesis.* Biomaterials, 2005. **26**(27): p. 5474-5491.
44. Sundelacruz, S. and D.L. Kaplan, *Stem cell- and scaffold-based tissue engineering approaches to osteochondral regenerative medicine.* Semin Cell Dev Biol, 2009. **20**(6): p. 646-55.

45. Betz, M.W., et al., *Macroporous Hydrogels Upregulate Osteogenic Signal Expression and Promote Bone Regeneration.* Biomacromolecules, 2010. **In Press**.
46. Alsberg, E., E.E. Hill, and D.J. Mooney, *Craniofacial tissue engineering.* Crit Rev Oral Biol Med, 2001. **12**(1): p. 64-75.
47. Yang, S.F., et al., *The design of scaffolds for use in tissue engineering. Part 1. Traditional factors.* Tissue Engineering, 2001. **7**(6): p. 679-689.
48. Klawitter, J.J. and S.F. Hulbert, *APPLICATION OF POROUS CERAMICS FOR THE ATTACHMENT OF LOAD BEARING INTERNAL ORTHOPEDIC APPLICATIONS.* Journal of Biomedical Materials Research Biomedical Materials Symposium
, 1972. **2**: p. 161-229.
49. Aronin, C.E.P., et al., *Comparative effects of scaffold pore size, pore volume, and total void volume on cranial bone healing patterns using microsphere-based scaffolds.* Journal of Biomedical Materials Research Part A, 2009. **89A**(3): p. 632-641.
50. Roosa, S.M.M., et al., *The pore size of polycaprolactone scaffolds has limited influence on bone regeneration in an in vivo model.* Journal of Biomedical Materials Research Part A, 2010. **92A**(1): p. 359-368.
51. Volkmer, E., et al., *Hypoxia in static and dynamic 3D culture systems for tissue engineering of bone.* Tissue Engineering Part A, 2008. **14**(8): p. 1331-1340.
52. Jin, Q.M., et al., *Effects of geometry of hydroxyapatite as a cell substratum in BMP-induced ectopic bone formation.* Journal of Biomedical Materials Research, 2000. **51**(3): p. 491-499.
53. Kuboki, Y., Q.M. Jin, and H. Takita, *Geometry of carriers controlling phenotypic expression in BMP-induced osteogenesis and chondrogenesis.* Journal of Bone and Joint Surgery-American Volume, 2001. **83A**: p. S105-S115.
54. Murphy, C.M., M.G. Haugh, and F.J. O'Brien, *The effect of mean pore size on cell attachment, proliferation and migration in collagen-glycosaminoglycan scaffolds for bone tissue engineering.* Biomaterials, 2003. **31**(3): p. 461-6.
55. Uebersax, L., et al., *Effect of scaffold design on bone morphology in vitro.* Tissue Eng, 2006. **12**(12): p. 3417-29.
56. Rose, F.R., et al., *In vitro assessment of cell penetration into porous hydroxyapatite scaffolds with a central aligned channel.* Biomaterials, 2004. **25**(24): p. 5507-14.
57. Shor, L., et al., *Fabrication of three-dimensional polycaprolactone/hydroxyapatite tissue scaffolds and osteoblast-scaffold interactions in vitro.* Biomaterials, 2007. **28**(35): p. 5291-7.
58. Pamula, E., et al., *Resorbable polymeric scaffolds for bone tissue engineering: the influence of their microstructure on the growth of human osteoblast-like MG 63 cells.* J Biomed Mater Res A, 2009. **89**(2): p. 432-43.
59. Zhou, H., et al., *A study of effective diffusivity in porous scaffold by Brownian dynamics simulation.* Journal of Colloid and Interface Science, 2010. **342**(2): p. 620-628.

60. Lu, J.X., et al., *Role of interconnections in porous bioceramics on bone recolonization in vitro and in vivo.* J Mater Sci Mater Med, 1999. **10**(2): p. 111-20.
61. Jones, A.C., et al., *The correlation of pore morphology, interconnectivity and physical properties of 3D ceramic scaffolds with bone ingrowth.* Biomaterials, 2009. **30**(7): p. 1440-51.
62. Jones, A.C., et al., *Assessment of bone ingrowth into porous biomaterials using MICRO-CT.* Biomaterials, 2007. **28**(15): p. 2491-504.
63. Otsuki, B., et al., *Pore throat size and connectivity determine bone and tissue ingrowth into porous implants: three-dimensional micro-CT based structural analyses of porous bioactive titanium implants.* Biomaterials, 2006. **27**(35): p. 5892-900.
64. Chu, T.M.G., et al., *Mechanical and in vivo performance of hydroxyapatite implants with controlled architectures.* Biomaterials, 2002. **23**(5): p. 1283-1293.
65. Breuls, R.G., T.U. Jiya, and T.H. Smit, *Scaffold stiffness influences cell behavior: opportunities for skeletal tissue engineering.* Open Orthop J, 2008. **2**: p. 103-9.
66. Norman, L.L., K. Stroka, and H. Aranda-Espinoza, *Guiding axons in the central nervous system: a tissue engineering approach.* Tissue Eng Part B Rev, 2009. **15**(3): p. 291-305.
67. Schlunck, G., et al., *Substrate rigidity modulates cell matrix interactions and protein expression in human trabecular meshwork cells.* Invest Ophthalmol Vis Sci, 2008. **49**(1): p. 262-9.
68. Guo, W.H., et al., *Substrate rigidity regulates the formation and maintenance of tissues.* Biophys J, 2006. **90**(6): p. 2213-20.
69. Engler, A.J., et al., *Matrix elasticity directs stem cell lineage specification.* Cell, 2006. **126**(4): p. 677-89.
70. Khatiwala, C.B., et al., *The regulation of osteogenesis by ECM rigidity in MC3T3-E1 cells requires MAPK activation.* J Cell Physiol, 2007. **211**(3): p. 661-72.
71. Evans, N.D., et al., *Substrate stiffness affects early differentiation events in embryonic stem cells.* Eur Cell Mater, 2009. **18**: p. 1-13; discussion 13-4.
72. Rowlands, A.S., P.A. George, and J.J. Cooper-White, *Directing osteogenic and myogenic differentiation of MSCs: interplay of stiffness and adhesive ligand presentation.* Am J Physiol Cell Physiol, 2008. **295**(4): p. C1037-44.
73. Kundu, A.K., C.B. Khatiwala, and A.J. Putnam, *Extracellular matrix remodeling, integrin expression, and downstream signaling pathways influence the osteogenic differentiation of mesenchymal stem cells on poly(lactide-co-glycolide) substrates.* Tissue Eng Part A, 2009. **15**(2): p. 273-83.
74. Peyton, S.R., et al., *The effects of matrix stiffness and RhoA on the phenotypic plasticity of smooth muscle cells in a 3-D biosynthetic hydrogel system.* Biomaterials, 2008. **29**(17): p. 2597-607.
75. McBeath, R., et al., *Cell shape, cytoskeletal tension, and RhoA regulate stem cell lineage commitment.* Dev Cell, 2004. **6**(4): p. 483-95.

76. Declercq, H.A., et al., *Osteoblast behaviour on in situ photopolymerizable three-dimensional scaffolds based on D, L-lactide, epsilon-caprolactone and trimethylene carbonate.* J Mater Sci Mater Med, 2006. **17**(2): p. 113-22.
77. Fisher, J.P., D. Dean, and A.G. Mikos, *Photocrosslinking characteristics and mechanical properties of diethyl fumarate/poly(propylene fumarate) biomaterials.* Biomaterials, 2002. **23**(22): p. 4333-43.
78. Takahashi, Y., M. Yamamoto, and Y. Tabata, *Osteogenic differentiation of mesenchymal stem cells in biodegradable sponges composed of gelatin and beta-tricalcium phosphate.* Biomaterials, 2005. **26**(17): p. 3587-96.
79. Kuo, Y.C., C.F. Yeh, and J.T. Yang, *Differentiation of bone marrow stromal cells in poly(lactide-co-glycolide)/chitosan scaffolds.* Biomaterials, 2009. **30**(34): p. 6604-13.
80. Norman, J.J., et al., *Microstructures in 3D biological gels affect cell proliferation.* Tissue Eng Part A, 2008. **14**(3): p. 379-90.
81. Collins, J.M., et al., *Three-Dimensional Culture with Stiff Microstructures Increases Proliferation and Slows Osteogenic Differentiation of Human Mesenchymal Stem Cells.* Small, 2009.
82. dos Santos, E.A., et al., *Chemical and topographical influence of hydroxyapatite and beta-tricalcium phosphate surfaces on human osteoblastic cell behavior.* J Biomed Mater Res A, 2009. **89**(2): p. 510-20.
83. Neel, E.A., et al., *Chemical, modulus and cell attachment studies of reactive calcium phosphate filler-containing fast photo-curing, surface-degrading, polymeric bone adhesives.* Acta Biomater, 2010. **(In Press)**.
84. McCullen, S.D., et al., *Electrospun composite poly(L-lactic acid)/tricalcium phosphate scaffolds induce proliferation and osteogenic differentiation of human adipose-derived stem cells.* Biomed Mater, 2009. **4**(3): p. 35002.
85. Dean, D., et al., *Poly(propylene fumarate) and poly(DL-lactic-co-glycolic acid) as scaffold materials for solid and foam-coated composite tissue-engineered constructs for cranial reconstruction.* Tissue Eng, 2003. **9**(3): p. 495-504.
86. Dawson, J.I., et al., *Development of specific collagen scaffolds to support the osteogenic and chondrogenic differentiation of human bone marrow stromal cells.* Biomaterials, 2008. **29**(21): p. 3105-16.
87. Fernandes, H., et al., *The role of collagen crosslinking in differentiation of human mesenchymal stem cells and MC3T3-E1 cells.* Tissue Eng Part A, 2009. **15**(12): p. 3857-67.
88. Buxton, P.G., et al., *Dense collagen matrix accelerates osteogenic differentiation and rescues the apoptotic response to MMP inhibition.* Bone, 2008. **43**(2): p. 377-85.
89. Tierney, C.M., et al., *The effects of collagen concentration and crosslink density on the biological, structural and mechanical properties of collagen-GAG scaffolds for bone tissue engineering.* J Mech Behav Biomed Mater, 2009. **2**(2): p. 202-9.
90. Anderson, E.J. and M.L. Knothe Tate, *Design of tissue engineering scaffolds as delivery devices for mechanical and mechanically modulated signals.* Tissue Eng, 2007. **13**(10): p. 2525-38.

91. Dean, D., K.J. Min, and A. Bond, *Computer aided design of large-format prefabricated cranial plates.* J Craniofac Surg, 2003. **14**(6): p. 819-32.
92. Min, K. and D. Dean. *Highly Accurate CAD Tools for Cranial Implants*. in *Medical Image Computing and Computer Assisted Intervention*. 2003. Heidelberg: Springer Verlag.
93. Sachlos, E. and J.T. Czernuszka, *Making tissue engineering scaffolds work. Review: the application of solid freeform fabrication technology to the production of tissue engineering scaffolds.* Eur Cell Mater, 2003. **5**: p. 29-39; discussion 39-40.
94. Koegler, W.S. and L.G. Griffith, *Osteoblast response to PLGA tissue engineering scaffolds with PEO modified surface chemistries and demonstration of patterned cell response.* Biomaterials, 2004. **25**(14): p. 2819-30.
95. Hutmacher, D.W., et al., *Mechanical properties and cell cultural response of polycaprolactone scaffolds designed and fabricated via fused deposition modeling.* J Biomed Mater Res, 2001. **55**(2): p. 203-16.
96. Landers, R. and R. Mulhaupt, *Desktop manufacturing of complex objects, prototypes and biomedical scaffolds by means of computer-assisted design combined with computer-guided 3D plotting of polymers and reactive oligomers.* Macromolecular Materials and Engineering, 2000. **282**(9): p. 17-21.
97. Williams, J.M., et al., *Bone tissue engineering using polycaprolactone scaffolds fabricated via selective laser sintering.* Biomaterials, 2005. **26**(23): p. 4817-27.
98. Lin, C.Y., et al., *Structural and mechanical evaluations of a topology optimized titanium interbody fusion cage fabricated by selective laser melting process.* J Biomed Mater Res A, 2007. **83**(2): p. 272-9.
99. Wilson, C.E., et al., *Design and fabrication of standardized hydroxyapatite scaffolds with a defined macro-architecture by rapid prototyping for bone-tissue-engineering research.* J Biomed Mater Res A, 2004. **68**(1): p. 123-32.
100. Fernandez, J.G., et al., *Micro- and nanostructuring of freestanding, biodegradable, thin sheets of chitosan via soft lithography.* J Biomed Mater Res A, 2008. **85**(1): p. 242-7.
101. Bhattarai, N., et al., *Electrospun chitosan-based nanofibers and their cellular compatibility.* Biomaterials, 2005. **26**(31): p. 6176-84.
102. Cooke, M.N., et al., *Use of stereolithography to manufacture critical-sized 3D biodegradable scaffolds for bone ingrowth.* J Biomed Mater Res B Appl Biomater, 2003. **64**(2): p. 65-9.
103. Lan, P.X., et al., *Development of 3D PPF/DEF scaffolds using micro-stereolithography and surface modification.* J Mater Sci Mater Med, 2009. **20**(1): p. 271-9.
104. Lee, J.W., et al., *Fabrication and characteristic analysis of a poly(propylene fumarate) scaffold using micro-stereolithography technology.* J Biomed Mater Res B Appl Biomater, 2008. **87**(1): p. 1-9.

105. Lee, K.W., et al., *Poly(propylene fumarate) bone tissue engineering scaffold fabrication using stereolithography: effects of resin formulations and laser parameters.* Biomacromolecules, 2007. **8**(4): p. 1077-84.
106. Lee, K.W., et al., *Fabrication and characterization of poly(propylene fumarate) scaffolds with controlled pore structures using 3-dimensional printing and injection molding.* Tissue Eng, 2006. **12**(10): p. 2801-11.
107. D Dean, J.W., K Kim, AG Mikos, and JP Fisher, *Stereolithographic Rendering of Low Molecular Weight Polymer Scaffolds for Bone Tissue Engineering. In: Innovative Developments in Design and Manufacturing*, in *Advanced Research in Virtual and Rapid Prototyping*, Taylor & Francis, London. In Press.
108. Dean, D., et al. *Stereolithographic Rendering of Low Molecular Weight Polymer Scaffolds for Bone Tissue Engineering. In: Innovative Developments in Design and Manufacturing*. in *Innovative Developments in Design and Manufacturing: Advanced research in virtual and rapid prototyping*. 2010. Boca Raton, FL: CRC Press (Taylor & Francis).
109. Jansen, J., et al., *Fumaric acid monoethyl ester-functionalized poly(D,L-lactide)/N-vinyl-2-pyrrolidone resins for the preparation of tissue engineering scaffolds by stereolithography.* Biomacromolecules, 2009. **10**(2): p. 214-20.
110. Melchels, F.P., J. Feijen, and D.W. Grijpma, *A poly(D,L-lactide) resin for the preparation of tissue engineering scaffolds by stereolithography.* Biomaterials, 2009. **30**(23-24): p. 3801-9.
111. Chen, V.J., L.A. Smith, and P.X. Ma, *Bone regeneration on computer-designed nano-fibrous scaffolds.* Biomaterials, 2006. **27**(21): p. 3973-9.
112. Geffre, C.P., et al., *A novel biomimetic polymer scaffold design enhances bone ingrowth.* J Biomed Mater Res A, 2009. **91**(3): p. 795-805.
113. Ciocca, L., et al., *CAD/CAM and rapid prototyped scaffold construction for bone regenerative medicine and surgical transfer of virtual planning: a pilot study.* Comput Med Imaging Graph, 2009. **33**(1): p. 58-62.
114. Suri, S. and C.E. Schmidt, *Photopatterned collagen-hyaluronic acid interpenetrating polymer network hydrogels.* Acta Biomater, 2009. **5**(7): p. 2385-97.
115. Dhariwala, B., E. Hunt, and T. Boland, *Rapid prototyping of tissue-engineering constructs, using photopolymerizable hydrogels and stereolithography.* Tissue Eng, 2004. **10**(9-10): p. 1316-22.
116. Williams, C.G., et al., *In vitro chondrogenesis of bone marrow-derived mesenchymal stem cells in a photopolymerizing hydrogel.* Tissue Eng, 2003. **9**(4): p. 679-88.
117. Arcaute, K., B.K. Mann, and R.B. Wicker, *Stereolithography of three-dimensional bioactive poly(ethylene glycol) constructs with encapsulated cells.* Ann Biomed Eng, 2006. **34**(9): p. 1429-41.
118. Arcaute, K., B. Mann, and R. Wicker, *Stereolithography of spatially controlled multi-material bioactive poly(ethylene glycol) scaffolds.* Acta Biomater, 2009.

119. Mapili, G., et al., *Laser-layered microfabrication of spatially patterned functionalized tissue-engineering scaffolds.* J Biomed Mater Res B Appl Biomater, 2005. **75**(2): p. 414-24.
120. Kim, K. and J.P. Fisher, *Nanoparticle technology in bone tissue engineering.* J Drug Target, 2007. **15**(4): p. 241-52.
121. Chu, T.M., et al., *Hydroxyapatite implants with designed internal architecture.* J Mater Sci Mater Med, 2001. **12**(6): p. 471-8.
122. Barry, J.J., et al., *In vitro study of hydroxyapatite-based photocurable polymer composites prepared by laser stereolithography and supercritical fluid extraction.* Acta Biomater, 2008. **4**(6): p. 1603-10.
123. Popov, V.K., et al., *Laser stereolithography and supercritical fluid processing for custom-designed implant fabrication.* J Mater Sci Mater Med, 2004. **15**(2): p. 123-8.
124. Padilla, S., S. Sanchez-Salcedo, and M. Vallet-Regi, *Bioactive glass as precursor of designed-architecture scaffolds for tissue engineering.* J Biomed Mater Res A, 2007. **81**(1): p. 224-32.
125. Padilla, S., S. Sanchez-Salcedo, and M. Vallet-Regi, *Bioactive and biocompatible pieces of HA/sol-gel glass mixtures obtained by the gel-casting method.* J Biomed Mater Res A, 2005. **75**(1): p. 63-72.
126. Gough, J.E., J.R. Jones, and L.L. Hench, *Nodule formation and mineralisation of human primary osteoblasts cultured on a porous bioactive glass scaffold.* Biomaterials, 2004. **25**(11): p. 2039-46.
127. Jones, J.R., et al., *Extracellular matrix formation and mineralization on a phosphate-free porous bioactive glass scaffold using primary human osteoblast (HOB) cells.* Biomaterials, 2007. **28**(9): p. 1653-63.
128. Meseguer-Olmo, L., et al., *In vitro behaviour of adult mesenchymal stem cells seeded on a bioactive glass ceramic in the SiO(2)-CaO-P(2)O(5) system.* Acta Biomater, 2008. **4**(4): p. 1104-13.
129. Robiony, M., et al., *Virtual reality surgical planning for maxillofacial distraction osteogenesis: the role of reverse engineering rapid prototyping and cooperative work.* J Oral Maxillofac Surg, 2007. **65**(6): p. 1198-208.
130. D'Urso, P.S., O.D. Williamson, and R.G. Thompson, *Biomodeling as an aid to spinal instrumentation.* Spine (Phila Pa 1976), 2005. **30**(24): p. 2841-5.
131. Juergens, P., et al., *Computer simulation and rapid prototyping for the reconstruction of the mandible.* J Oral Maxillofac Surg, 2009. **67**(10): p. 2167-70.
132. Kluess, D., et al., *A convenient approach for finite-element-analyses of orthopaedic implants in bone contact: modeling and experimental validation.* Comput Methods Programs Biomed, 2009. **95**(1): p. 23-30.
133. Sagbo, S., et al., *New orthopaedic implant management tool for computer-assisted planning, navigation, and simulation: from implant CAD files to a standardized XML-based implant database.* Comput Aided Surg, 2005. **10**(5-6): p. 311-9.
134. Lal, K., et al., *Use of stereolithographic templates for surgical and prosthodontic implant planning and placement. Part I. The concept.* J Prosthodont, 2006. **15**(1): p. 51-8.

135. D'Urso, P.S., et al., *Custom cranioplasty using stereolithography and acrylic.* Br J Plast Surg, 2000. **53**(3): p. 200-4.
136. Winder, J. and R. Bibb, *Medical rapid prototyping technologies: state of the art and current limitations for application in oral and maxillofacial surgery.* J Oral Maxillofac Surg, 2005. **63**(7): p. 1006-15.
137. Min, K. and D. Dean. *Surface smoothing and template partitioning for cranial implant CAD*. in *Medical Imaging 2005: Visualization, Image-Guided Procedures, and Display*. 2005. Bellingham, WA: SPIE-The International Society for Optical Enginnering.
138. Cohen, A., et al., *Mandibular reconstruction using stereolithographic 3-dimensional printing modeling technology.* Oral Surg Oral Med Oral Pathol Oral Radiol Endod, 2009. **108**(5): p. 661-6.
139. Holck, D.E., et al., *Benefits of stereolithography in orbital reconstruction.* Ophthalmology, 1999. **106**(6): p. 1214-8.
140. Wagner, J.D., et al., *Rapid 3-dimensional prototyping for surgical repair of maxillofacial fractures: a technical note.* J Oral Maxillofac Surg, 2004. **62**(7): p. 898-901.
141. Carr, J.C., W.R. Fright, and R.K. Beatson, *Surface interpolation with radial basis functions for medical imaging.* Ieee Transactions on Medical Imaging, 1997. **16**(1): p. 96-107.
142. Eufinger, H., et al., *Reconstruction of Craniofacial Bone Defects with Individual Alloplastic Implants Based on Cad/Cam-Manipulated Ct-Data.* Journal of Cranio-Maxillo-Facial Surgery, 1995. **23**(3): p. 175-181.
143. Scholz, M., et al., *Reconstruction of the temporal contour for traumatic tissue loss using a CAD/CAM-prefabricated titanium implant-case report.* Journal of Cranio-Maxillofacial Surgery, 2007. **35**(8): p. 388-392.
144. Lee, S.C., et al., *Cranioplasty using polymethyl methacrylate prostheses.* Journal of Clinical Neuroscience, 2009. **16**(1): p. 56-63.
145. Nassiri, N., D.R. Cleary, and B.A. Ueeck, *Is Cranial Reconstruction With a Hard-Tissue Replacement Patient-Matched Implant as Safe as Previously Reported? A 3-Year Experience and Review of the Literature.* Journal of Oral and Maxillofacial Surgery, 2009. **67**(2): p. 323-327.
146. Harrysson, O.L., Y.A. Hosni, and J.F. Nayfeh, *Custom-designed orthopedic implants evaluated using finite element analysis of patient-specific computed tomography data: femoral-component case study.* BMC Musculoskelet Disord, 2007. **8**: p. 91.
147. Koulouvaris, P., et al., *Custom-design implants for severe distorted proximal anatomy of the femur in young adults followed for 4-8 years.* Acta Orthop, 2008. **79**(2): p. 203-10.
148. Gotze, C., et al., *Is there a need of custom-made prostheses for total hip arthroplasty? Gait analysis, clinical and radiographic analysis of customized femoral components.* Arch Orthop Trauma Surg, 2009. **129**(2): p. 267-74.
149. Chim, H. and J.T. Schantz, *New frontiers in calvarial reconstruction: integrating computer-assisted design and tissue engineering in cranioplasty.* Plast Reconstr Surg, 2005. **116**(6): p. 1726-41.

150. Sisto, D.J. and V.K. Sarin, *Patellofemoral arthroplasty with a customized trochlear prosthesis.* Orthop Clin North Am, 2008. **39**(3): p. 355-62, vi-vii.
151. Ryken, T.C., et al., *Engineering patient-specific drill templates and bioabsorbable posterior cervical plates: a feasibility study.* J Neurosurg Spine, 2009. **10**(2): p. 129-32.
152. Ryken, T.C., et al., *Image-based drill templates for cervical pedicle screw placement.* J Neurosurg Spine, 2009. **10**(1): p. 21-6.
153. Lee, M.H., et al., *Considerations for tissue-engineered and regenerative medicine product development prior to clinical trials in the United States.* Tissue Eng Part B Rev, 2010. **16**(1): p. 41-54.
154. Sato, M. and T.J. Webster, *Nanobiotechnology: implications for the future of nanotechnology in orthopedic applications.* Expert Rev Med Devices, 2004. **1**(1): p. 105-14.
155. Liu, Q., J.R. de Wijn, and C.A. van Blitterswijk, *Composite biomaterials with chemical bonding between hydroxyapatite filler particles and PEG/PBT copolymer matrix.* J Biomed Mater Res, 1998. **40**(3): p. 490-7.
156. Wei, G. and P.X. Ma, *Structure and properties of nano-hydroxyapatite/polymer composite scaffolds for bone tissue engineering.* Biomaterials, 2004. **25**(19): p. 4749-57.
157. Kim, S.S., et al., *Poly(lactide-co-glycolide)/hydroxyapatite composite scaffolds for bone tissue engineering.* Biomaterials, 2006. **27**(8): p. 1399-409.
158. Kim, S.S., et al., *A poly(lactide-co-glycolide)/hydroxyapatite composite scaffold with enhanced osteoconductivity.* J Biomed Mater Res A, 2007. **80**(1): p. 206-15.
159. Shi, X., et al., *Injectable nanocomposites of single-walled carbon nanotubes and biodegradable polymers for bone tissue engineering.* Biomacromolecules, 2006. **7**(7): p. 2237-42.
160. Yoo, J.J. and S.H. Rhee, *Evaluations of bioactivity and mechanical properties of poly (epsilon-caprolactone)/silica nanocomposite following heat treatment.* J Biomed Mater Res A, 2004. **68**(3): p. 401-10.
161. Xu, H.H., D.T. Smith, and C.G. Simon, *Strong and bioactive composites containing nano-silica-fused whiskers for bone repair.* Biomaterials, 2004. **25**(19): p. 4615-26.
162. Xu, H.H., *Dental composite resins containing silica-fused ceramic single-crystalline whiskers with various filler levels.* J Dent Res, 1999. **78**(7): p. 1304-11.
163. Horch, R.A., et al., *Nanoreinforcement of poly(propylene fumarate)-based networks with surface modified alumoxane nanoparticles for bone tissue engineering.* Biomacromolecules, 2004. **5**(5): p. 1990-8.
164. Goto, K., et al., *Bioactive bone cements containing nano-sized titania particles for use as bone substitutes.* Biomaterials, 2005. **26**(33): p. 6496-505.
165. Kay, S., et al., *Nanostructured polymer/nanophase ceramic composites enhance osteoblast and chondrocyte adhesion.* Tissue Eng, 2002. **8**(5): p. 753-61.

166. Liu, H., E.B. Slamovich, and T.J. Webster, *Increased osteoblast functions on nanophase titania dispersed in poly-lactic-co-glycolic acid composites.* Nanotechnology, 2005. **16** (7): p. S601-S608.
167. Liu, H., E.B. Slamovich, and T.J. Webster, *Increased osteoblast functions among nanophase titania/poly(lactide-co-glycolide) composites of the highest nanometer surface roughness.* J Biomed Mater Res A, 2006. **78**(4): p. 798-807.
168. Webster, T.J., R.W. Siegel, and R. Bizios, *Osteoblast adhesion on nanophase ceramics.* Biomaterials, 1999. **20**(13): p. 1221-7.
169. Webster, T.J. and T.A. Smith, *Increased osteoblast function on PLGA composites containing nanophase titania.* J Biomed Mater Res A, 2005. **74**(4): p. 677-86.
170. Smith, L.A. and P.X. Ma, *Nano-fibrous scaffolds for tissue engineering.* Colloids Surf B Biointerfaces, 2004. **39**(3): p. 125-31.
171. Chen, J., B. Chu, and B.S. Hsiao, *Mineralization of hydroxyapatite in electrospun nanofibrous poly(L-lactic acid) scaffolds.* J Biomed Mater Res A, 2006. **79**(2): p. 307-17.
172. Woo, K.M., V.J. Chen, and P.X. Ma, *Nano-fibrous scaffolding architecture selectively enhances protein adsorption contributing to cell attachment.* J Biomed Mater Res A, 2003. **67**(2): p. 531-7.
173. Woo, K.M., et al., *Nano-fibrous scaffolding promotes osteoblast differentiation and biomineralization.* Biomaterials, 2007. **28**(2): p. 335-43.
174. Li, W.J., et al., *Multilineage differentiation of human mesenchymal stem cells in a three-dimensional nanofibrous scaffold.* Biomaterials, 2005. **26**(25): p. 5158-66.
175. Li, W.J., et al., *A three-dimensional nanofibrous scaffold for cartilage tissue engineering using human mesenchymal stem cells.* Biomaterials, 2005. **26**(6): p. 599-609.
176. Shin, M., H. Yoshimoto, and J.P. Vacanti, *In vivo bone tissue engineering using mesenchymal stem cells on a novel electrospun nanofibrous scaffold.* Tissue Eng, 2004. **10**(1-2): p. 33-41.
177. Tuzlakoglu, K., et al., *Nano- and micro-fiber combined scaffolds: a new architecture for bone tissue engineering.* J Mater Sci Mater Med, 2005. **16**(12): p. 1099-104.
178. Yoshimoto, H., et al., *A biodegradable nanofiber scaffold by electrospinning and its potential for bone tissue engineering.* Biomaterials, 2003. **24**(12): p. 2077-82.
179. Li, W.J., et al., *Electrospun nanofibrous structure: a novel scaffold for tissue engineering.* J Biomed Mater Res, 2002. **60**(4): p. 613-21.
180. Xin, X., M. Hussain, and J.J. Mao, *Continuing differentiation of human mesenchymal stem cells and induced chondrogenic and osteogenic lineages in electrospun PLGA nanofiber scaffold.* Biomaterials, 2007. **28**(2): p. 316-25.
181. Bhattarai, S.R., et al., *Novel biodegradable electrospun membrane: scaffold for tissue engineering.* Biomaterials, 2004. **25**(13): p. 2595-602.
182. Rose, F.R. and R.O. Oreffo, *Bone tissue engineering: hope vs hype.* Biochem Biophys Res Commun, 2002. **292**(1): p. 1-7.

183. Babensee, J.E., L.V. McIntire, and A.G. Mikos, *Growth factor delivery for tissue engineering.* Pharm Res, 2000. **17**(5): p. 497-504.
184. Orban, J.M., K.G. Marra, and J.O. Hollinger, *Composition options for tissue-engineered bone.* Tissue Eng, 2002. **8**(4): p. 529-39.
185. Rose, F.R., Q. Hou, and R.O. Oreffo, *Delivery systems for bone growth factors - the new players in skeletal regeneration.* J Pharm Pharmacol, 2004. **56**(4): p. 415-27.
186. Southwood, L.L., et al., *Delivery of growth factors using gene therapy to enhance bone healing.* Vet Surg, 2004. **33**(6): p. 565-78.
187. Tabata, Y., *Nanomaterials of drug delivery systems for tissue regeneration.* Methods Mol Biol, 2005. **300**: p. 81-100.
188. Lu, L., M.J. Yaszemski, and A.G. Mikos, *TGF-beta1 release from biodegradable polymer microparticles: its effects on marrow stromal osteoblast function.* J Bone Joint Surg Am, 2001. **83-A Suppl 1**(Pt 2): p. S82-91.
189. Meinel, L., et al., *Stabilizing insulin-like growth factor-I in poly(D,L-lactide-co-glycolide) microspheres.* J Control Release, 2001. **70**(1-2): p. 193-202.
190. Oldham, J.B., et al., *Biological activity of rhBMP-2 released from PLGA microspheres.* J Biomech Eng, 2000. **122**(3): p. 289-92.
191. Dang, J.M. and K.W. Leong, *Natural polymers for gene delivery and tissue engineering.* Adv Drug Deliv Rev, 2006. **58**(4): p. 487-99.
192. Kirker-Head, C.A., *Potential applications and delivery strategies for bone morphogenetic proteins.* Adv Drug Deliv Rev, 2000. **43**(1): p. 65-92.
193. Kofron, M.D. and C.T. Laurencin, *Bone tissue engineering by gene delivery.* Adv Drug Deliv Rev, 2006. **58**(4): p. 555-76.
194. Li, R.H. and J.M. Wozney, *Delivering on the promise of bone morphogenetic proteins.* Trends Biotechnol, 2001. **19**(7): p. 255-65.
195. Mansouri, S., et al., *Chitosan-DNA nanoparticles as non-viral vectors in gene therapy: strategies to improve transfection efficacy.* Eur J Pharm Biopharm, 2004. **57**(1): p. 1-8.
196. Panyam, J. and V. Labhasetwar, *Biodegradable nanoparticles for drug and gene delivery to cells and tissue.* Adv Drug Deliv Rev, 2003. **55**(3): p. 329-47.
197. Yamamoto, M. and Y. Tabata, *Tissue engineering by modulated gene delivery.* Adv Drug Deliv Rev, 2006. **58**(4): p. 535-54.
198. Cohen, H., et al., *Sustained delivery and expression of DNA encapsulated in polymeric nanoparticles.* Gene Ther, 2000. **7**(22): p. 1896-905.
199. McAllister, K., et al., *Polymeric nanogels produced via inverse microemulsion polymerization as potential gene and antisense delivery agents.* J Am Chem Soc, 2002. **124**(51): p. 15198-207.
200. Choi, S.W., W.S. Kim, and J.H. Kim, *Surface-functionalized nanoparticles for controlled drug delivery.* Methods Mol Biol, 2005. **303**: p. 121-31.
201. Prabha, S., et al., *Size-dependency of nanoparticle-mediated gene transfection: studies with fractionated nanoparticles.* Int J Pharm, 2002. **244**(1-2): p. 105-15.

202. Yi, F., H. Wu, and G.L. Jia, *Formulation and characterization of poly (D,L-lactide-co-glycolide) nanoparticle containing vascular endothelial growth factor for gene delivery.* J Clin Pharm Ther, 2006. **31**(1): p. 43-8.
203. Li, Y., et al., *PEGylated PLGA nanoparticles as protein carriers: synthesis, preparation and biodistribution in rats.* J Control Release, 2001. **71**(2): p. 203-11.
204. Jang, J.S., et al., *Poly(ethylene glycol)/poly(epsilon-caprolactone) diblock copolymeric nanoparticles for non-viral gene delivery: the role of charge group and molecular weight in particle formation, cytotoxicity and transfection.* J Control Release, 2006. **113**(2): p. 173-82.
205. Kushibiki, T. and Y. Tabata, *Preparation of poly(ethylene glycol)-introduced cationized gelatin as a non-viral gene carrier.* J Biomater Sci Polym Ed, 2005. **16**(11): p. 1447-61.
206. Hosseinkhani, H. and Y. Tabata, *Self assembly of DNA nanoparticles with polycations for the delivery of genetic materials into cells.* J Nanosci Nanotechnol, 2006. **6**(8): p. 2320-8.
207. Murakami, Y., et al., *A novel synthetic tissue-adhesive hydrogel using a crosslinkable polymeric micelle.* J Biomed Mater Res A, 2007. **80**(2): p. 421-7.
208. Kanayama, N., et al., *A PEG-based biocompatible block catiomer with high buffering capacity for the construction of polyplex micelles showing efficient gene transfer toward primary cells.* ChemMedChem, 2006. **1**(4): p. 439-44.
209. Ono, I., et al., *Combination of porous hydroxyapatite and cationic liposomes as a vector for BMP-2 gene therapy.* Biomaterials, 2004. **25**(19): p. 4709-18.
210. Park, J., et al., *Bone regeneration in critical size defects by cell-mediated BMP-2 gene transfer: a comparison of adenoviral vectors and liposomes.* Gene Ther, 2003. **10**(13): p. 1089-98.
211. Matsuo, T., et al., *Injectable magnetic liposomes as a novel carrier of recombinant human BMP-2 for bone formation in a rat bone-defect model.* J Biomed Mater Res A, 2003. **66**(4): p. 747-54.
212. Chandrasekar, D., et al., *The development of folate-PAMAM dendrimer conjugates for targeted delivery of anti-arthritic drugs and their pharmacokinetics and biodistribution in arthritic rats.* Biomaterials, 2007. **28**(3): p. 504-12.
213. Ohashi, S., et al., *Cationic polymer-mediated genetic transduction into cultured human chondrosarcoma-derived HCS-2/8 cells.* J Orthop Sci, 2001. **6**(1): p. 75-81.
214. Choi, J.S., et al., *Dexamethasone conjugated poly(amidoamine) dendrimer as a gene carrier for efficient nuclear translocation.* Int J Pharm, 2006. **320**(1-2): p. 171-8.
215. Erbacher, P., et al., *Chitosan-based vector/DNA complexes for gene delivery: biophysical characteristics and transfection ability.* Pharm Res, 1998. **15**(9): p. 1332-9.
216. Mansouri, S., et al., *Characterization of folate-chitosan-DNA nanoparticles for gene therapy.* Biomaterials, 2006. **27**(9): p. 2060-5.

217. Shen, H., J. Tan, and W.M. Saltzman, *Surface-mediated gene transfer from nanocomposites of controlled texture.* Nat Mater, 2004. **3**(8): p. 569-74.
218. Putnam, D., *Polymers for gene delivery across length scales.* Nat Mater, 2006. **5**(6): p. 439-51.
219. Duncan, R., *Polymer conjugates as anticancer nanomedicines.* Nat Rev Cancer, 2006. **6**(9): p. 688-701.
220. Moghimi, S.M., A.C. Hunter, and J.C. Murray, *Nanomedicine: current status and future prospects.* FASEB J, 2005. **19**(3): p. 311-30.
221. Nishiyama, N. and K. Kataoka, *Current state, achievements, and future prospects of polymeric micelles as nanocarriers for drug and gene delivery.* Pharmacol Ther, 2006. **112**(3): p. 630-48.
222. Nishiyama, N. and K. Kataoka, *Nanostructured Devices Based on Block Copolymer Assemblies for Drug Delivery: Designing Structures for Enhanced Drug Function* in *Advances in Polymer Science*. 2006, Springer Berlin / Heidelberg. p. 67-101.
223. Emerich, D.F. and C.G. Thanos, *Nanomeicine.* Current Nanoscience, 2005. **1**: p. 177-188.
224. Svenson, S. and D.A. Tomalia, *Dendrimers in biomedical applications--reflections on the field.* Adv Drug Deliv Rev, 2005. **57**(15): p. 2106-29.
225. Karmali, P.P. and A. Chaudhuri, *Cationic liposomes as non-viral carriers of gene medicines: resolved issues, open questions, and future promises.* Med Res Rev, 2007. **27**(5): p. 696-722.
226. Corsi, K., et al., *Mesenchymal stem cells, MG63 and HEK293 transfection using chitosan-DNA nanoparticles.* Biomaterials, 2003. **24**(7): p. 1255-64.
227. Baksh, D., L. Song, and R.S. Tuan, *Adult mesenchymal stem cells: characterization, differentiation, and application in cell and gene therapy.* J Cell Mol Med, 2004. **8**(3): p. 301-16.
228. Jaiswal, N., et al., *Osteogenic differentiation of purified, culture-expanded human mesenchymal stem cells in vitro.* J Cell Biochem, 1997. **64**(2): p. 295-312.
229. Peter, S.J., et al., *Osteoblastic phenotype of rat marrow stromal cells cultured in the presence of dexamethasone, beta-glycerolphosphate, and L-ascorbic acid.* J Cell Biochem, 1998. **71**(1): p. 55-62.
230. Derubeis, A.R. and R. Cancedda, *Bone marrow stromal cells (BMSCs) in bone engineering: limitations and recent advances.* Ann Biomed Eng, 2004. **32**(1): p. 160-5.
231. Shanti, R.M., et al., *Adult mesenchymal stem cells: biological properties, characteristics, and applications in maxillofacial surgery.* J Oral Maxillofac Surg, 2007. **65**(8): p. 1640-7.
232. Shung, A.K., et al., *Kinetics of poly(propylene fumarate) synthesis by step polymerization of diethyl fumarate and propylene glycol using zinc chloride as a catalyst.* Journal of Biomaterials Science-Polymer Edition, 2002. **13**(1): p. 95-108.
233. He, S., et al., *Synthesis of biodegradable poly(propylene fumarate) networks with poly(propylene fumarate)-diacrylate macromers as crosslinking agents*

and characterization of their degradation products. Polymer, 2001. **42**(3): p. 1251-1260.
234. Fisher, J.P., et al., *Photoinitiated cross-linking of the biodegradable polyester poly(propylene fumarate). Part I. Determination of network structure.* Biomacromolecules, 2003. **4**(5): p. 1327-34.
235. Fisher, J.P., et al., *Photoinitiated cross-linking of the biodegradable polyester poly(propylene fumarate). Part II. In vitro degradation.* Biomacromolecules, 2003. **4**(5): p. 1335-42.
236. Lee, K.W., et al., *Physical properties and cellular responses to crosslinkable poly(propylene fumarate)/hydroxyapatite nanocomposites.* Biomaterials, 2008. **29**(19): p. 2839-48.
237. Peter, S.J., et al., *Marrow stromal osteoblast function on a poly(propylene fumarate)/beta-tricalcium phosphate biodegradable orthopaedic composite.* Biomaterials, 2000. **21**(12): p. 1207-13.
238. Shi, X.F., et al., *Injectable nanocomposites of single-walled carbon nanotubes and biodegradable polymers for bone tissue engineering.* Biomacromolecules, 2006. **7**(7): p. 2237-2242.
239. Lee, J.W., et al., *3D scaffold fabrication with PPF/DEF using micro-stereolithography.* Microelectronic Engineering, 2007. **84**(5-8): p. 1702-1705.
240. Lee, K.W., et al., *Poly(propylene fumarate) bone tissue engineering scaffold fabrication using stereolithography: Effects of resin formulations and laser parameters.* Biomacromolecules, 2007. **8**(4): p. 1077-1084.
241. Kempen, D.H., et al., *Retention of in vitro and in vivo BMP-2 bioactivities in sustained delivery vehicles for bone tissue engineering.* Biomaterials, 2008. **29**(22): p. 3245-52.
242. Peter, S.J., et al., *Effects of transforming growth factor beta1 released from biodegradable polymer microparticles on marrow stromal osteoblasts cultured on poly(propylene fumarate) substrates.* J Biomed Mater Res, 2000. **50**(3): p. 452-62.
243. Ishaug, S.L., et al., *Bone formation by three-dimensional stromal osteoblast culture in biodegradable polymer scaffolds.* J Biomed Mater Res, 1997. **36**(1): p. 17-28.
244. Vehof, J.W., et al., *Influence of rhBMP-2 on rat bone marrow stromal cells cultured on titanium fiber mesh.* Tissue Eng, 2001. **7**(4): p. 373-83.
245. Goldstein, A.S., *Effect of seeding osteoprogenitor cells as dense clusters on cell growth and differentiation.* Tissue Eng, 2001. **7**(6): p. 817-27.
246. Bitar, M., et al., *Effect of cell density on osteoblastic differentiation and matrix degradation of biomimetic dense collagen scaffolds.* Biomacromolecules, 2008. **9**(1): p. 129-35.
247. Kruyt, M., et al., *Analysis of the Dynamics of Bone Formation, Effect of Cell Seeding Density, and Potential of Allogeneic Cells in Cell-Based Bone Tissue Engineering in Goats.* Tissue Eng Part A, 2008.
248. Zhou, Y.F., et al., *Does seeding density affect in vitro mineral nodules formation in novel composite scaffolds?* J Biomed Mater Res A, 2006. **78**(1): p. 183-93.

249. Lieb, E., et al., *Effects of transforming growth factor beta1 on bonelike tissue formation in three-dimensional cell culture. II: Osteoblastic differentiation.* Tissue Eng, 2004. **10**(9-10): p. 1414-25.
250. van den Dolder, J., et al., *Observations on the effect of BMP-2 on rat bone marrow cells cultured on titanium substrates of different roughness.* Biomaterials, 2003. **24**(11): p. 1853-60.
251. van der Zande, M., et al., *The effect of combined application of TGFbeta-1, BMP-2, and COLLOSS E on the development of bone marrow derived osteoblast-like cells in vitro.* J Biomed Mater Res A, 2008. **86**(3): p. 788-95.
252. Toh, Y.C., et al., *Application of a polyelectrolyte complex coacervation method to improve seeding efficiency of bone marrow stromal cells in a 3D culture system.* Biomaterials, 2005. **26**(19): p. 4149-60.
253. Banoub, R.W., M. Fernstrom, and R.J. Ruch, *Lack of growth inhibition or enhancement of gap junctional intercellular communication and connexin43 expression by beta-carotene in murine lung epithelial cells in vitro.* Cancer Lett, 1996. **108**(1): p. 35-40.
254. van den Dolder, J., P.H. Spauwen, and J.A. Jansen, *Evaluation of various seeding techniques for culturing osteogenic cells on titanium fiber mesh.* Tissue Eng, 2003. **9**(2): p. 315-25.
255. Mygind, T., et al., *Mesenchymal stem cell ingrowth and differentiation on coralline hydroxyapatite scaffolds.* Biomaterials, 2007. **28**(6): p. 1036-47.
256. Owen, T.A., et al., *Progressive development of the rat osteoblast phenotype in vitro: reciprocal relationships in expression of genes associated with osteoblast proliferation and differentiation during formation of the bone extracellular matrix.* J Cell Physiol, 1990. **143**(3): p. 420-30.
257. Lian, J.B. and G.S. Stein, *Concepts of osteoblast growth and differentiation: basis for modulation of bone cell development and tissue formation.* Crit Rev Oral Biol Med, 1992. **3**(3): p. 269-305.
258. Rawadi, G., et al., *BMP-2 controls alkaline phosphatase expression and osteoblast mineralization by a Wnt autocrine loop.* J Bone Miner Res, 2003. **18**(10): p. 1842-53.
259. Pham, Q.P., et al., *The influence of an in vitro generated bone-like extracellular matrix on osteoblastic gene expression of marrow stromal cells.* Biomaterials, 2008. **29**(18): p. 2729-39.
260. Mackay, A.M., et al., *Chondrogenic differentiation of cultured human mesenchymal stem cells from marrow.* Tissue Eng, 1998. **4**(4): p. 415-28.
261. Lee, K.S., S.H. Hong, and S.C. Bae, *Both the Smad and p38 MAPK pathways play a crucial role in Runx2 expression following induction by transforming growth factor-beta and bone morphogenetic protein.* Oncogene, 2002. **21**(47): p. 7156-63.
262. Canalis, E., T.L. McCarthy, and M. Centrella, *Effects of platelet-derived growth factor on bone formation in vitro.* J Cell Physiol, 1989. **140**(3): p. 530-7.
263. Kim, S., et al., *In vivo bone formation from human embryonic stem cell-derived osteogenic cells in poly(d,l-lactic-co-glycolic acid)/hydroxyapatite composite scaffolds.* Biomaterials, 2008. **29**(8): p. 1043-53.

264. Lee, J.H., et al., *Control of Osteogenic Differentiation and Mineralization of Human Mesenchymal Stem Cells on Composite Nanofibers Containing Poly[lactic-co-(glycolic acid)] and Hydroxyapatite.* Macromol Biosci, 2009.
265. Ngiam, M., et al., *The fabrication of nano-hydroxyapatite on PLGA and PLGA/collagen nanofibrous composite scaffolds and their effects in osteoblastic behavior for bone tissue engineering.* Bone, 2009. **45**(1): p. 4-16.
266. Niu, X., et al., *Porous nano-HA/collagen/PLLA scaffold containing chitosan microspheres for controlled delivery of synthetic peptide derived from BMP-2.* J Control Release, 2009. **134**(2): p. 111-7.
267. Lewandrowski, K.U., et al., *Enhanced bioactivity of a poly(propylene fumarate) bone graft substitute by augmentation with nano-hydroxyapatite.* Biomed Mater Eng, 2003. **13**(2): p. 115-24.
268. Heo, S.J., et al., *In vitro and animal study of novel nano-hydroxyapatite/poly(epsilon-caprolactone) composite scaffolds fabricated by layer manufacturing process.* Tissue Eng Part A, 2009. **15**(5): p. 977-89.
269. Gupta, D., et al., *Nanostructured biocomposite substrates by electrospinning and electrospraying for the mineralization of osteoblasts.* Biomaterials, 2009. **30**(11): p. 2085-94.
270. Patel, M., et al., *Cyclic acetal hydroxyapatite composites and endogenous osteogenic gene expression of rat marrow stromal cells.* J Tissue Eng Regen Med.
271. Patel, M., et al., *Characterization of cyclic acetal hydroxyapatite nanocomposites for craniofacial tissue engineering.* J Biomed Mater Res A.
272. Shi, Z., et al., *Size effect of hydroxyapatite nanoparticles on proliferation and apoptosis of osteoblast-like cells.* Acta Biomater, 2009. **5**(1): p. 338-45.
273. Kim, K., et al., *Effect of Initial Cell Seeding Density on Early Osteogenic Signal Expression of Rat Bone Marrow Stromal Cells Cultured on Cross-Linked Poly(propylene fumarate) Disks.* Biomacromolecules, 2009.
274. Mistry, A.S., et al., *Fabrication and in vitro degradation of porous fumarate-based polymer/alumoxane nanocomposite scaffolds for bone tissue engineering.* J Biomed Mater Res A, 2009. **89**(1): p. 68-79.
275. Mistry, A.S., A.G. Mikos, and J.A. Jansen, *Degradation and biocompatibility of a poly(propylene fumarate)-based/alumoxane nanocomposite for bone tissue engineering.* J Biomed Mater Res A, 2007. **83**(4): p. 940-53.
276. Mistry, A.S., et al., *In vivo bone biocompatibility and degradation of porous fumarate-based polymer/alumoxane nanocomposites for bone tissue engineering.* J Biomed Mater Res A, 2009.
277. Cai, Z.Y., et al., *Poly(propylene fumarate)/(calcium sulphate/beta-tricalcium phosphate) composites: preparation, characterization and in vitro degradation.* Acta Biomater, 2009. **5**(2): p. 628-35.
278. Grayson, W.L., et al., *Effects of initial seeding density and fluid perfusion rate on formation of tissue-engineered bone.* Tissue Eng Part A, 2008. **14**(11): p. 1809-20.
279. Lode, A., A. Bernhardt, and M. Gelinsky, *Cultivation of human bone marrow stromal cells on three-dimensional scaffolds of mineralized collagen:*

influence of seeding density on colonization, proliferation and osteogenic differentiation. J Tissue Eng Regen Med, 2008. **2**(7): p. 400-7.
280. van Gaalen, S.M., et al., *Relating cell proliferation to in vivo bone formation in porous Ca/P scaffolds.* J Biomed Mater Res A, 2009.
281. He, J., D.C. Genetos, and J.K. Leach, *Osteogenesis and trophic factor secretion are influenced by the composition of hydroxyapatite/ poly(lactide-co-glycolide) composite scaffolds.* Tissue Eng Part A, 2009.
282. Fickert, S., J. Fiedler, and R.E. Brenner, *Identification, quantification and isolation of mesenchymal progenitor cells from osteoarthritic synovium by fluorescence automated cell sorting.* Osteoarthritis Cartilage, 2003. **11**(11): p. 790-800.
283. Kotobuki, N., et al., *Viability and osteogenic potential of cryopreserved human bone marrow-derived mesenchymal cells.* Tissue Eng, 2005. **11**(5-6): p. 663-73.
284. Gronthos, S., et al., *Integrin-mediated interactions between human bone marrow stromal precursor cells and the extracellular matrix.* Bone, 2001. **28**(2): p. 174-81.
285. Gajjeraman, S., et al., *Biological assemblies provide novel templates for the synthesis of hierarchical structures and facilitate cell adhesion.* Adv Funct Mater, 2008. **18**(24): p. 3972-3980.
286. Chastain, S.R., et al., *Adhesion of mesenchymal stem cells to polymer scaffolds occurs via distinct ECM ligands and controls their osteogenic differentiation.* J Biomed Mater Res A, 2006. **78**(1): p. 73-85.
287. Rouahi, M., et al., *Quantitative kinetic analysis of gene expression during human osteoblastic adhesion on orthopaedic materials.* Biomaterials, 2006. **27**(14): p. 2829-44.
288. Gibson, L.J., *The mechanical behaviour of cancellous bone.* J Biomech, 1985. **18**(5): p. 317-28.
289. Liao, J., et al., *Development of nanohydroxyapatite/polycarbonate composite for bone repair.* J Biomater Appl, 2009. **24**(1): p. 31-45.
290. Guarino, V., et al., *The role of hydroxyapatite as solid signal on performance of PCL porous scaffolds for bone tissue regeneration.* J Biomed Mater Res B Appl Biomater, 2008. **86B**(2): p. 548-57.
291. Phimphilai, M., et al., *BMP signaling is required for RUNX2-dependent induction of the osteoblast phenotype.* J Bone Miner Res, 2006. **21**(4): p. 637-46.
292. Choi, K.Y., et al., *Runx2 regulates FGF2-induced Bmp2 expression during cranial bone development.* Dev Dyn, 2005. **233**(1): p. 115-21.
293. Beenken, A. and M. Mohammadi, *The FGF family: biology, pathophysiology and therapy.* Nat Rev Drug Discov, 2009. **8**(3): p. 235-53.
294. Liu, Y., et al., *In vitro effects of nanophase hydroxyapatite particles on proliferation and osteogenic differentiation of bone marrow-derived mesenchymal stem cells.* J Biomed Mater Res A, 2009. **90**(4): p. 1083-91.
295. Kim, K., et al., *Stereolithographic Bone Scaffold Design Parameters: Osteogenic Differentiation and Signal Expression.* Tissue Eng Part B Rev. **(In Press)**.

296. Takai, E., et al., *Substrate modulation of osteoblast adhesion strength, focal adhesion kinase activation, and responsiveness to mechanical stimuli.* Mol Cell Biomech, 2006. **3**(1): p. 1-12.
297. Peyton, S.R. and A.J. Putnam, *Extracellular matrix rigidity governs smooth muscle cell motility in a biphasic fashion.* J Cell Physiol, 2005. **204**(1): p. 198-209.
298. Docheva, D., et al., *Researching into the cellular shape, volume and elasticity of mesenchymal stem cells, osteoblasts and osteosarcoma cells by atomic force microscopy.* J Cell Mol Med, 2008. **12**(2): p. 537-52.
299. Hanjaya-Putra, D., et al., *Vascular endothelial growth factor and substrate mechanics regulate in vitro tubulogenesis of endothelial progenitor cells.* J Cell Mol Med, 2009.
300. Hsiong, S.X., et al., *Differentiation stage alters matrix control of stem cells.* J Biomed Mater Res A, 2008. **85**(1): p. 145-56.
301. Kong, H.J., et al., *FRET measurements of cell-traction forces and nano-scale clustering of adhesion ligands varied by substrate stiffness.* Proc Natl Acad Sci U S A, 2005. **102**(12): p. 4300-5.
302. Reilly, G.C. and A.J. Engler, *Intrinsic extracellular matrix properties regulate stem cell differentiation.* J Biomech, 2010. **43**(1): p. 55-62.
303. Zhang, Y., et al., *The effects of pore architecture in silk fibroin scaffolds on the growth and differentiation of mesenchymal stem cells expressing BMP7.* Acta Biomater.
304. Lee, K.W., et al., *Enhanced cell ingrowth and proliferation through three-dimensional nanocomposite scaffolds with controlled pore structures.* Biomacromolecules. **11**(3): p. 682-9.
305. Li, S., et al., *Macroporous biphasic calcium phosphate scaffold with high permeability/porosity ratio.* Tissue Eng, 2003. **9**(3): p. 535-48.
306. Xu, C.C. and R.W. Chan, *Pore architecture of a bovine acellular vocal fold scaffold.* Tissue Eng Part A, 2008. **14**(11): p. 1893-903.
307. Athanasiou, K.A., et al., *Fundamentals of biomechanics in tissue engineering of bone.* Tissue Eng, 2000. **6**(4): p. 361-81.
308. Rezwan, K., et al., *Biodegradable and bioactive porous polymer/inorganic composite scaffolds for bone tissue engineering.* Biomaterials, 2006. **27**(18): p. 3413-31.
309. Saito, E., et al., *Experimental and computational characterization of designed and fabricated 50:50 PLGA porous scaffolds for human trabecular bone applications.* J Mater Sci Mater Med, 2010.
310. Kemppainen, J.M. and S.J. Hollister, *Differential effects of designed scaffold permeability on chondrogenesis by chondrocytes and bone marrow stromal cells.* Biomaterials, 2010. **31**(2): p. 279-87.
311. Lee, K.S., et al., *Runx2 is a common target of transforming growth factor beta1 and bone morphogenetic protein 2, and cooperation between Runx2 and Smad5 induces osteoblast-specific gene expression in the pluripotent mesenchymal precursor cell line C2C12.* Mol Cell Biol, 2000. **20**(23): p. 8783-92.

312. Selvamurugan, N., et al., *Transforming growth factor-beta 1 regulation of collagenase-3 expression in osteoblastic cells by cross-talk between the Smad and MAPK signaling pathways and their components, Smad2 and Runx2.* J Biol Chem, 2004. **279**(18): p. 19327-34.
313. Xiao, G., et al., *Fibroblast growth factor 2 induction of the osteocalcin gene requires MAPK activity and phosphorylation of the osteoblast transcription factor, Cbfa1/Runx2.* J Biol Chem, 2002. **277**(39): p. 36181-7.
314. Baffour, R., et al., *Enhanced angiogenesis and growth of collaterals by in vivo administration of recombinant basic fibroblast growth factor in a rabbit model of acute lower limb ischemia: dose-response effect of basic fibroblast growth factor.* J Vasc Surg, 1992. **16**(2): p. 181-91.
315. Bikfalvi, A., et al., *Biological roles of fibroblast growth factor-2.* Endocr Rev, 1997. **18**(1): p. 26-45.
316. Woei Ng, K., et al., *Osteogenic differentiation of murine embryonic stem cells is mediated by fibroblast growth factor receptors.* Stem Cells Dev, 2007. **16**(2): p. 305-18.
317. Mandriota, S.J. and M.S. Pepper, *Vascular endothelial growth factor-induced in vitro angiogenesis and plasminogen activator expression are dependent on endogenous basic fibroblast growth factor.* J Cell Sci, 1997. **110 (Pt 18)**: p. 2293-302.
318. Deckers, M.M., et al., *Expression of vascular endothelial growth factors and their receptors during osteoblast differentiation.* Endocrinology, 2000. **141**(5): p. 1667-74.
319. Street, J., et al., *Vascular endothelial growth factor stimulates bone repair by promoting angiogenesis and bone turnover.* Proc Natl Acad Sci U S A, 2002. **99**(15): p. 9656-61.
320. Saadeh, P.B., et al., *Mechanisms of fibroblast growth factor-2 modulation of vascular endothelial growth factor expression by osteoblastic cells.* Endocrinology, 2000. **141**(6): p. 2075-83.
321. Natsume, H., et al., *Rho-kinase limits FGF-2-stimulated VEGF release in osteoblasts.* Bone, 2010. **46**(4): p. 1068-74.
322. Takai, S., et al., *Negative regulation by p70 S6 kinase of FGF-2-stimulated VEGF release through stress-activated protein kinase/c-Jun N-terminal kinase in osteoblasts.* J Bone Miner Res, 2007. **22**(3): p. 337-46.
323. Takai, S., et al., *Activation of phosphatidylinositol 3-kinase/Akt limits FGF-2-induced VEGF release in osteoblasts.* Mol Cell Endocrinol, 2007. **267**(1-2): p. 46-54.
324. Tokuda, H., et al., *Involvement of SAPK/JNK in basic fibroblast growth factor-induced vascular endothelial growth factor release in osteoblasts.* J Endocrinol, 2003. **177**(1): p. 101-7.
325. Murphy, C.M., M.G. Haugh, and F.J. O'Brien, *The effect of mean pore size on cell attachment, proliferation and migration in collagen-glycosaminoglycan scaffolds for bone tissue engineering.* Biomaterials, 2010. **31**(3): p. 461-6.
326. Roosa, S.M., et al., *The pore size of polycaprolactone scaffolds has limited influence on bone regeneration in an in vivo model.* J Biomed Mater Res A, 2009. **92**(1): p. 359-68.

327. Byers, B.A. and A.J. Garcia, *Exogenous Runx2 expression enhances in vitro osteoblastic differentiation and mineralization in primary bone marrow stromal cells.* Tissue Eng, 2004. **10**(11-12): p. 1623-32.
328. Zhang, Y., et al., *The effects of Runx2 immobilization on poly (epsilon-caprolactone) on osteoblast differentiation of bone marrow stromal cells in vitro.* Biomaterials, 2010. **31**(12): p. 3231-6.